Towards ultracold Caesium isomers

Tanapoom Poomaradee

A dissertation submitted in partial fulfillment
of the requirements for the degree of
Doctor of Philosophy
of
University College London.

Department of Physics and Astronomy
University College London

September 23, 2021

I, Tanapoom Poomaradee, confirm that the work presented in this thesis is my own. Where information has been derived from other sources, I confirm that this has been indicated in the work.

Abstract

This PhD thesis reports on works towards laser cooling and trapping caesium isotopes and nuclear isomers. The main outcome of the research was the installation of an experimental facility for obtaining $\sim$100 μK samples of ^{135m}Cs, and in the test of the facility with $^{133}Cs^{+}$ ionic beams neutralised and trapped in Magneto-Optical Traps (MOTs). The work can be divided into three related experiments, instrumental for obtaining ultra-cold isomers of caesium atoms.

The first part was conducted in the laser cooling laboratory at University College London. The task consisted of designing and setting up a laser and imaging systems for a dual-chamber MOT of ^{133}Cs atoms. The laser systems comprise of two main lasers, cooling and repumping lasers, each equipped with frequency stabilisation and amplification stages.

The second part of the work took place in the Accelerator Laboratory of the University of Jyväskylä (Finland). Here, the systems created at UCL were transferred and installed within the existing Ion Guide Isotope Separation On-Line (IGISOL) facility. The reassembled system was tested again with the ^{133}Cs MOT and optimised for stability and robustness in a new, uncontrolled, and noisy environment.

In the third part of the experiment, the system in Finland was upgraded for neutralisation and laser cooling of an incoming +1 ions beam produced by IGISOL. This required the installation of a new experimental chamber, equipped with a thin Y foil for ion implantation and neutralisation, and coated with a low-desorption energy coating to increase the trapping efficiency. In parallel, the ions' delivery system and connection to the IGISOL electrostatic transport line were also created.

In this phase, the implantation of $^{135m}Cs^{+}$ beams was tested. In order to monitor the production and transport of the desired ions, the gamma decay of ^{135m}Cs implanted in a Ge detector was observed. The life-time of ^{135m}Cs atoms was measured to confirm the implanted species. Moreover, trapping of ^{135}Cs was attempted.

The long term goal of the research started with this thesis is to employ the facility to realise Bose-Einstein condensate of ^{135m}Cs. The realisation would have numbers of applications, most notably paving the path for investigations on multi-body physics in ultra-cold nuclear matter, and the demonstration of the generation of coherent gamma photons.

Impact Statement

The main impact of this thesis is the development and characterisation of ion-implanted cold atom system. The ion-implanted cold atom system is a modification of a cold neutral atom experiment. It can generate cold radioactive atomic samples employing ion implantation and laser cooling and trapping techniques. The radioactive source is created by implanted radioactive ions provided by an ion beam accelerator facility. Then, the atoms are cooled and trapped by means of laser cooling and trapping techniques. The combined method of radioactive ion implantation and laser cooling and trapping is a promising approach for the exploration of the nature of cold radioactive isotopes and isomers. The laser system for the cold atom experiment was first assembled and tested at University College London (UCL) in 2015 and moved to University of Jyväskylä (JYU) Accelerator Laboratory, Finland in 2016. At JYU, the cold atom experiment was built and coupled with the K-130 cyclotron ion beam accelerator located in the Ion Guide Isotope Separation On-Line (IGISOL) facility. The coupled system has been entirely operational since 2017. Achievements to date of the system are magneto-optical trapping of ion-implanted ^{133}Cs, successful implantation of ^{135,135m}Cs atoms and preliminary evidence of ^{135}Cs trapping.

The long term aim to realise coherent gamma-ray sources will have an impact also beyond academia. The demonstration of a method to produce coherent gamma rays would enhance current technologies to a new level of precision. This will lead to a new generation of high-accuracy gamma knifes for stereotactic radiation therapy and to new approaches to gamma-imaging for nuclear security. In addition, the laser cooling and trapping technique used in this thesis can improve the precision

of radioactive trace detection used in nuclear forensics to the ultra-sensitive level. Moreover, the coupled system designed and built in this thesis could also be suitable, with appropriate modifications, for investigation of other cold isotopes not just for caesium.

Within academia, this thesis is a preliminary result of a larger ultra-cold radioactive caesium project, which required multidisciplinary knowledge, ranging from atomic and optical physics to nuclear physics. Therefore, it has been established under the international collaboration between UCL and JYU. The project has been supported by the Engineering and Physical Sciences Research Council (EPSRC), the Atomic Weapons Establishment (AWE) and the European Commission under Horizon 2020. Establishment of the project generates new challenge research topics which benefit researchers and science students in the UK and Europe. Moreover, the result presented in this thesis was published in the international peer-reviewed journal Nuclear Instruments and Methods in Physics Research Section A (NIMA). There have been four PhDs, and three of UCL's undergraduate students involved in this project since 2014. The research project is still active and attracts undergraduate, PhD students and researchers.

Acknowledgements

During the five years of my PhD, there are many excellent persons who gave me helps and advises that contributed to my PhD work and personal life. Therefore, I would like to express my gratitude to them.

Firstly, I sincerely thank my generous supervisor, Prof. Ferruccio Renzoni. His advice boosts my productivity and also the freedom to do research. Moreover, I thank him for introducing me to the combined field of atomic physics and nuclear physics, which provided me with new experiences of doing international research. It is my pleasure to be one of his students.

I would like to thanks Dr Luca Marmugi for mentoring me to be a disciplined researcher (although, I have not achieved such level of discipline) and teach me everything about laser cooling. He is the most disciplined, diligent and one of the perfect physicists who are expert in both theory and experiment I have ever met. I am sure that I am not his exceptional student, but I am very proud to have spent five years working with him.

I want to thank Dr Alexandros Giatzoglou, my colleague, for contributing to this research project, especially in the Finland part. He is a skilful physicist and resilient experimentalist. If he wants to do things, it will happen.

In the early stage of my PhD, Dr Michela Venturelli and Dr Raffaele Nolli allowed me to join them in the Rb BEC project. They are very kind and had a lot of patience with me. They also took care not only in the Lab but in terms of my personal life as well. Especially Dr Michela, my life coach, I admire her as my big sister, and I thank her a lot for everything.

I want to thank Prof. Iain Moore and Dr Sami Rinta-Antila, University of

Jyvaskyla, Finland, for excellent support when I worked in Finland. Without them, the project would have not succeeded.

In the UCL laser cooling group, there were great people who shared office with me. I thank Dr Cameron Deans for his help in the experiment. He is the most consistent and smart person I have ever met. I thank Sindi Sula, Krishna Jadeja, and Yuval Cohen: working with you was a great pleasure. I thank Ben Maddox, my colleague, for his hard work.

Apart from the academic aspect, I would like to thank persons who took care of me during the five years in the UK. I thank Dr Apimook Watcharangkool for helping me settling down in the UK and for his excellent cooking skills. I thank Dr Nattawadee Panyain for her superb organisation skill, which made my life much more comfortable. I thank Dr Johnny Nguyen for friendship, suggestions, and encouragement.

I thank the Development and Promotion of Science and Technology Talents Project (DPST), my funder, for this great opportunity and all financial support. Moreover, I would like to thank the office of educational affairs in the United Kingdom (OEA UK) for taking care not just me but all Thai students in the UK.

I thank my lovely daughter, Athens, and my wife, Benchawan Tuntipong, for being a great motivation in my life. Finally, I thank my parents, Mr Preechar and Mrs Nucharin Phummaradee, for excellent supports and forgiveness, which helped me overcome all hard times in my life. They have been working very hard to raise me being a proper person. I dedicate this thesis to them.

Contents

List of Figures

List of Tables

Chapter 1

Introduction

1.1 Nuclear Structure

An atom consists of three types of subatomic particles, protons (+1 e-charge each), neutrons (neutral) and electrons (-1 e-charge each), where e is the magnitude of the electron charge. In neutral atoms, the number of protons (Z) and electrons are equal. On the other hand, the neutron is a neutral charge, and the neutron number (N) do not affect the electron number but the stability of the nucleus. Either a proton or a neutron is called a nucleon. The nucleons occupy the central region of an atom to be a nucleus. For an element, an atom has a certain number of protons and electrons. However, its neutron number could vary. Atoms with the same proton number but a different number of neutrons are called isotopes.

The electrons orbit around the nucleus and bind with the proton by electrostatic force. The quantum mechanical model explains probabilistic behaviours of electrons, where the key to the model is to solve the Schrödinger equation. Due to the Pauli exclusion principle, the orbiting electrons possess unique energies described by a set of quantum numbers n, L, m, and S, where n is the principal quantum number, L is angular momentum quantum number, m is the magnetic quantum number, and S is electron spin angular momentum. The electrons energies are quantised to discrete energy levels or electron shells indicated by n. In each shell, electrons can orbit in numbers of angular momentum represented by L. The m described projection of the angular moment to the quantisation axis, and S refers to spins of an

electron. These quantum numbers establish the fine structure of the electron energy levels. However, the fine structure energy level can be split further to hyperfine level by considering the coupling of electron total angular momentum and nucleus spin (represented by a quantum number, I).

In the nucleus, nucleons bind together via the strong nuclear force [1], which generates nuclear potential energy. Similar to the electron, nucleons also have shell structures explained by the shell model [1][2][3]. Nucleons with given energies are arranged into discrete energy shells, which are occupied by specific numbers of nucleons. The inner shell hold nucleons which have lower energy than those in the outer shell. Once a shell is filled up, the remaining nucleon will go to another shell with higher energy. The closed-shell nuclei of an isotope that have either proton number, Z and neutron number, N equal to one of the magic numbers (2, 8, 20, 28, 50, 82 and 126) have higher binding energy compared to other nearby isotopes, and the shape of the magic nucleus are spherical in the ground state. The non-magic number nuclei are deformed in shape to minimise their nuclear potential energy to reach the ground state [1].

In analogous to electrons, nuclei also have excited states which mostly decay rapidly. A nucleus's excited state can be occurred by promoting outer shell nucleons to higher energy levels [1][3]. Once the outer shell nucleon is promoted, the nuclear charge distribution of the inner shell is redistributed, resulting in alternating the nuclear potential energy to a new local minimum. Most of the excited states of nuclei have ultra-short lifetimes. However, in some nuclei, there are some long measurable lifetimes excited states called metastable states. The metastable state occurred due to a large change of spin, spin projection or shape of the nucleus, which led to the forbidden decay. Some of the isotopes with metastable states are isomers, which are products of nuclear reactions such as the decay of radioactive nuclei. Moreover, the isomer can be produced experimentally using the ion implantation technique discussed in this thesis.

1.2 Nuclear isomers

Nuclear isomers are isotopes which have metastable excited nuclei [2][3]. The term nuclear isomer was proposed by Fredrick Soddy [4] in 1917 and the first experimental observation of a nuclear isomer, ^{234m}Pa, was done by Otto Hahn [5] in 1921.

In order to discriminate nuclear isomers from other excited nuclear states, their half-life is considered. Typically, the half-life of excited nuclei is around picoseconds [6], while the metastable excited nuclei of isomers live significantly longer. Although there is no qualified half-life for identifying an isomer, it typically ranges between nanoseconds and years. Remarkably, some nuclear isomers, mostly in super-heavy nuclei, survive much longer than their ground states [7]. An example is ^{270}Ds with isomer state half-life of $\sim$6 ms and $\sim$100 μs ground state half-life. As a metastable excited nuclear state, an isomer can have higher-order excitations, which are labelled by the superscript letter "m","n","p" or "q" marking first to the fourth excited state, respectively [7].

There are many radioactive decay modes of nuclear isomers depending on excitation energy and nuclear structure [2]. α, β or γ are observed, as well as internal conversion (or isomeric transition, IT). Some isomers can also decay by nucleon emission or spontaneous fission.

1.2.1 Types of nuclear isomers

The nuclear isomers can be formed by different mechanisms as shown in figure 1.1, namely via a change of shape, spin or spin orientation [2]. The occurrence of isomers depends on the structure of the nuclear shell. Based on their forming mechanism, one can classify them into three types, namely shape isomers, spin traps and K-traps.

1.2.1.1 Spin traps

For the nucleus in the ground state, the nucleons are paired following Fermi-Dirac statistics. On the contrary, in the excited nucleus, one nucleon is promoted to a higher energy state, which causes the nucleon pair to break up. It may also produce a rearrangement of the remaining pairs. These nucleons are generally treated as quasi-

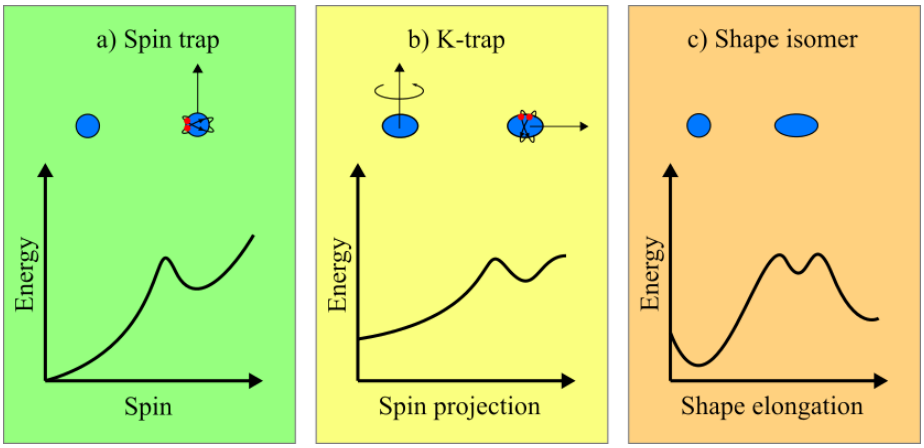

Figure 1.1: Type of Isomers: The left (right) blue objects are nucleus in ground state (excited state) of a) spin trap, b) K-trap and c) shape isomer. The change of nuclear spin, nuclear spin orientation and shape of nucleus generate local minima in nuclear potential energy (located in the horizontal position of the objects).

particles which contribute excitation energy of the nucleus and affect the remaining properties of the nucleus, such as angular momentum.

The spin trap, which represents the majority of isomers [2], arises from quasi-particles promoting the nucleus in a new angular momentum state. It forms a local energy minimum (Figure 1.1a) on the nuclear potential energy. In this case, the total nuclear angular momentum depends on the number of quasi-particles and the vector sum of their angular momenta. The probability of decaying back to the ground state of spin traps is low, due to unfavourable spin selection rules. As a result, the isomeric state is energetically convenient with respect to transitioning back to the ground state, which would require overcoming an energy barrier. The large energy difference and the unfavourable selection rules between the nuclear spin of the ground state and the excited state lead to emission of γ photons with multipolarity to match the nuclear spin change. The larger change of λ (the angular momentum carried by the radiation in units of $\hbar$) for the radiation lead to the smaller probability for the isomer to decay, which means the longer life-time. An alternative decay mode of spin traps involves internal conversion [2].

1.2.1.2 K-traps

K-trap is a form of spin trap. Apart from the magnitude of nuclear spin, the existence of K-traps also relies on the spin orientation relative to the symmetry axis of the nucleus. It emerges in regions of the N-Z space that are far from nuclei magic numbers of neutrons and protons, where the shape of the nucleus is typically prolate. The long axis of the prolate nucleus is defined as an axis of symmetry, and a quantum number, K represents the projection of the total nuclear spin on the axis of symmetry.

For K-traps to decay, the change of K could not exceed λ in order to meet nuclear-transition selection rules. However, due to the symmetry-breaking process, transitions that violate the selection rule (K-forbidden) are possible. Because of the highly unlikely transition, metastable isomers are created with a longer half-life.

1.2.1.3 Shape isomers

A shape (or fission) isomer is formed by elongation of the nucleus. The change of the nucleus's geometry (oblate or prolate) can contribute a secondary minimum on nuclear excited-states, as shown in figure 1.1c. Shape isomers can either decay back to the first energy minimum via an isomeric transition (IT) or split into two lighter nuclei via spontaneous fission. The latter case is the primary decay process for heavy nuclei [8][9].

Most of shape isomers emerge in heavy nuclei (A=80 region, A = 100 region and in a region around ^{208}Pb), and most of them decay by the spontaneous fission. However isomers can also occur in light nuclei, for example, ^{66}Ni (γ-decay, $t_{1/2} = 134 \pm 9$ ps) [9].

1.2.2 Caesium isomers

This thesis focus on cooling and trapping of caesium isotopes and isomers, which relate to the application goal explained in section 1.3. Therefore, it is worth to review the target element.

Caesium is an alkaline element, thus has one valence electron. Its atomic number, Z = 55 and electron configuration is $1s^2 2s^2 2p^6 3s^2 3p^6 3d^{10} 4s^2 4p^6 4d^{10} 5s^2 5p^6 6s^1$.

This simple electronic structure (hydrogen-like atom) of caesium produces optical absorption lines at 852 nm D2-line and 894 nm D1-line. Due to the availability of laser sources in this spectral regions, these lines have been widely exploited in atomic physics, from optical spectroscopy to laser cooling and trapping.

There are 40 discovered caesium isotopes, and there is only single stable isotope which is ^{133}Cs ($J^{\pi} = \frac{7}{2}^{+}$). Most of the caesium isotopes have beta decay mode, and there are 18 isotopes which have nuclear excited-state (isomers). Half of those isomers have IT or gamma decay mode. A list of isomers' lifetime, decay energy and nuclear spin is provided in table 1.1.

Caesium isomer	excitation energy (keV)	life-time	spin and parity, J^{π}
^{121m}Cs	68.5±0.3	122±3 s	$\frac{9}{2}^{(+)}$
^{123m}Cs	156.27±0.05	1.64±0.12 s	$\frac{11}{2}^{(-)}$
^{124m}Cs	462.55±0.17	6.3±0.2 s	$7^{(+)}$
^{130m}Cs	163.25±0.11	3.46±0.06 m	$5^{(-)}$
^{134m}Cs	138.7441±0.0026	2.912±0.002 h	$8^{(-)}$
^{135m}Cs	1632.9±1.5	53±2 m	$\frac{19}{2}^{(-)}$
^{136m}Cs	158±5	1.9±0.2 s	$8^{(-)}$
^{138m}Cs	79.9±0.3	2.91±0.08 m	$6^{(-)}$
^{144m}Cs	300±200	< 1 s	(> 3)

Table 1.1: List of γ decay caesium isomers (data is derived from [7]). The bracket indicates the state parity.

Caesium is suitable for laser cooling and trapping because of its large atomic mass (which leads to low recoil temperature) and large hyperfine energy splitting. However, its two-body inelastic collision cross-section contributed by direct magnetic dipole interaction is very high.

The inelastic losses are sensitive to internal states of the trapped atoms, which need to be carefully chosen. In order to suppress all of the two-body inelastic collisions at very low temperature, caesium atoms need to be trapped in the absolute ground state of $6^2S_{1/2}$ $F = 3, m_F = 3$. However, the absolute ground state is a high-field (magnetic) seeker because of the negative value of Landé g_F-factor. Therefore,

evaporative cooling in a magnetic trap is not allowed. Trapping and cooling of ultra-cold caesium can be operated in an optical trap such as optical dipole trap or optical lattice. The trapping force of the trap is determined by the gradient of energy shift from the AC Stark effect, also called 'light shift'. This is described in appendix C.

Caesium has a low melting temperature of 28.44^{o}C. Therefore, it is easy to be vaporised and released as a vapour into a vacuum chamber for atomic physics experiments.

1.2.3 Energy shifts in atomic spectra of isotopes and isomers

1.2.3.1 Isotopic and isomeric shift

Change in the nuclear properties of an isotope generates an energy shift in the atomic transition line i. The energy shift is contributed by two effects called 'mass shift' and 'field shift' [10]. In an isotope, the energy shift is called 'isotopic shift'. The isotopic shift of an isotope with mass number A' compared to the reference isotope with mass number A, $\delta\nu_i^{A',A}$ is expressed by [11]

$$\delta\nu_i^{A',A} = (K_{NMS} + K_{SMS})\left(\frac{1}{A} - \frac{1}{A'}\right) + F\,\delta\langle r^2\rangle^{A',A}, \tag{1.1}$$

The first right-hand side term of equation 1.1 is the mass shift which is determined by the difference in neutron number of two isotopes (mass number A and A') of an element, and it is the sum of the normal mass shift and specific mass shift. The normal mass shift is a correction in the reduced mass of the electron [12][13]. The normal mass shift constant is $K_{NMS} = \frac{\nu_i}{1836.1}$, where ν_i is transition frequency [12][10]. The specific mass shift is due to the correlation of electrons motion and recoil energy of the nucleus [13]. Calculation of the specific mass shift constant is more complicated and can be found in [11].

The second term is the field shift which is induced by the nuclear charge deformation [14][15][16]. The nucleus that lost/gained a neutron undergo deformation in nuclear charge structure. The charge deformation alters the mean square radius, $\delta\langle r^2\rangle^{A',A}$ of the nuclear charge distribution resulting in the field shift [10][17]. F is field shift constant which is an electronic factor related to the electron charge

density at the nucleus [18][19][20][21].

In an isomer (excited state of an isotope), the energy shift is called 'isomeric shift' [10][22]. The isomeric shift is determined only by the field shift because the mass of ground state and excited stated nuclei are equal. However, unlike in the isotopic shift, the cause of the shift is originated from a promoted nucleon which affects the nuclear charge distribution.

A shift in the optical transition frequency is produced as a result of the change in the nuclear properties determined by the change in the number of nucleons (in isotopes), and in the mean square radius of the nuclear charge distribution (in isotopes and isomers). The magnitude of the isotopic and energy shift (i.e., the sum of isotopic and isomeric shift) of ^{135}Cs with respect to ^{133}Cs are given in table 1.2 [23]. The contributions of these shifts to the optical spectrum are also displayed in figure 1.2.

^{133}Cs to ^{A}Cs	$\delta\nu_i^{133,A}$ (MHz)
133	0
135	-36.4
135m	-17.6

Table 1.2: Isotopic and isomeric shift of Caesium (the shift are relative to ^{133}Cs D2 line transition frequency).

1.2.3.2 Hyperfine energy shift

The hyperfine splitting of the energy levels of caesium isotopes and isomers is determined by the total nuclear angular momentum, I, the magnetic dipole constant, A_{hfs} and the electric quadrupole constant, B_{hfs}.The energy shifts are given [24] by

$$\Delta_{F,m_F} = \frac{1}{2}A_{hfs} + B_{hfs}\frac{\frac{3}{2}K(K+1) - 2I(I+1)J(J+1)}{4I(2I-1)J(2J-1)}, \tag{1.2}$$

where

$$K = F(F+1) - I(I+1) - J(J+1), \tag{1.3}$$

$|L-S| \leq J \leq L+S$ is total electron angular momentum, where L and S are the orbital angular momentum and the spin angular momentum, respectively. $|J-I| \leq F \leq J+I$ is total atomic angular momentum.

Although, equation 1.2 and 1.3 are general, we will restrict the discussion to ^{133}Cs, ^{135}Cs and ^{135m}Cs because these are the targets of this experiment. The spectra inclusive of the hyperfine splitting of ^{133}Cs, ^{135}Cs and ^{135m}Cs are shown in figure 1.2 and table 1.3. The shifts were determined via equation 1.2 and values of A_{hfs} and B_{hfs} are obtained from [23].

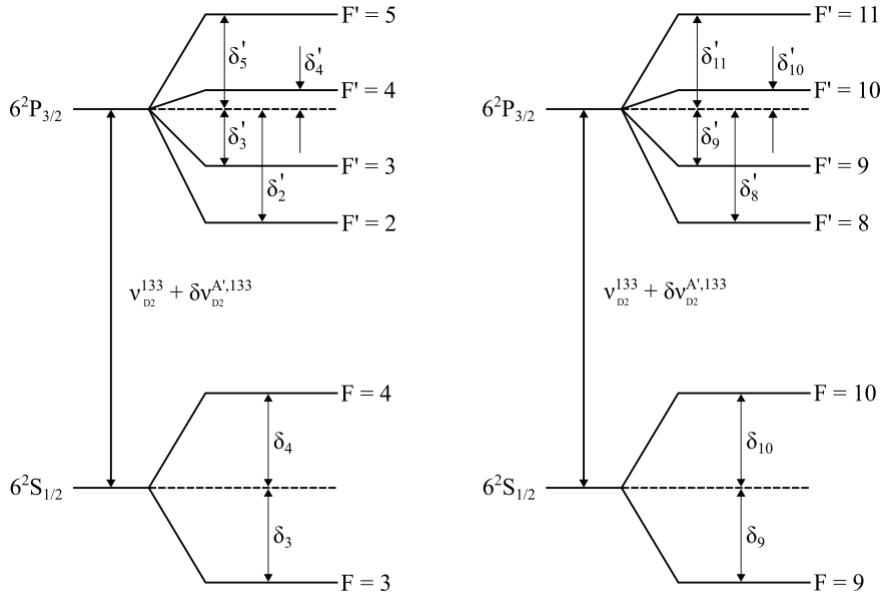

a) ^{133}Cs & ^{135}Cs b) ^{135m}Cs

Figure 1.2: Caesium isotopes hyperfine structure. ν_{D2}^{133} is the D2 line transition frequency of ^{133}Cs. $\nu_{D2}^{A',133}$ is the isotopic shift of caesium isotope, $^{A'}$Cs comparing to ^{133}Cs.

1.3 Applications of isomers

Isotopes and isomers of caesium can be exploited in many applications. In this section, two promising applications related to laser cooling and trapping are reviewed and discussed. The first one is nuclear forensic which utilise cold ^{135}Cs and ^{137}Cs in a magneto-optical trap (MOT) in order to enhance the isotopes detection sensitivity. The second one is collective γ-ray emission. This is a proposed application involv-

Fine Structure	Hyperfine Frequency Shift (MHz)				
		^{133}Cs	^{135}Cs		^{135m}Cs
$6^2P_{3/2}$	δ'_5	263	282	δ'_{11}	253
	δ'_4	13	12	δ'_{10}	93
	δ'_3	-188	-201	δ'_9	-135
	δ'_2	-339	-359	δ'_8	-202
$6^2S_{1/2}$	δ_4	4022	4254	δ_{10}	3390
	δ_3	-5171	-5470	δ_9	-3746

Table 1.3: Hyperfine shift of ^{133}Cs, ^{135}Cs and ^{135m}Cs. Fine structure levels are described by spectroscopic notation $n^{2S+1}l_J$ where n is the principle quantum number and l is a letter, "S" and "P" which represent the orbital angular momentum, $L = 0$ and $L = 1$, respectively. The minus sign indicate that hyperfine frequency shift down from fine structure level.

ing Bose-Einstein condensate of ^{135m}Cs to generate coherence γ-ray emission.

1.3.1 Cold radioactive atoms in nuclear forensics

^{137}Cs ($t_{1/2} = 30$ y) and ^{135}Cs ($t_{1/2} = 2.3 \times 10^6$ y) are abundant anthropogenic isotopes ($\sim$1ppb relative to amount of stable ^{133}Cs) which are fallout of nuclear activity such as the operation of nuclear power plants and nuclear weapons test [25][26]. Due to the high accessibility, ^{137}Cs is used as a radioactive tracer in many fields of studies. For example, in environmental transport studies, tracing of ^{137}Cs in the ocean is a conventional method to estimated length scales and velocities of the ocean flow [27][28]. Additionally, it is also used as a tracer of soil erosion because caesium atoms are highly reactive and attach to soil firmly [29]. In nuclear forensics, tracing the amount of ^{137}Cs is widely used. However, the age of nuclear sample estimated by the method can be inaccurate because of the non-uniform spatial distribution of fallout. Measuring ^{137}Cs/^{135}Cs ratio can improve accuracy of the nuclear forensic chronometric estimation compared to using of simple ^{137}Cs detection [25].

Unlike ^{137}Cs, tracing of ^{135}Cs faces many difficulties due long half-life of ^{135}Cs and very modest γ-ray emission. In order to obtain measurable γ-ray emission from ^{135}Cs by radioactive counting method, impractically large amounts of the

sample need to be collected. Additionally, a conventional mass spectrometer can rarely reveal the presence of ^{135}Cs because of interference from ^{133}Cs mass tail and isobaric interference of ^{135}Ba.

In order to overcome those problems, a magneto-optical trap is exploited for the ^{135}Cs and ^{137}Cs sampling. It is a promising method for detection of the caesium isotopes and other radioactive elements at ultra-sensitive level [25].

1.3.2 Bose-Einstein condensate approach for coherent gamma ray source

Gamma rays are electromagnetic radiation which has a wavelength less than 100 pm and radiation energy larger than X-ray. These properties result in a very large penetration power. The possibility to realise a gamma-ray laser (graser), and thus produce coherent gamma ray radiation, has been object of research for over three decades [30]. In order to realise the coherent gamma-ray source, coherence of the radiation need to be achieved. However, there are two obstacles to overcome in order to realise coherent gamma-ray sources: the narrow emission linewidth and the need of a large amount of radiation source. In atomic physics, a possible solution of the problems is the generation of coherent gamma photon via the collective decay of isomeric Bose-Einstein condensate.

Bose-Einstein condensate (BEC) is a state of matter in which particles occupy the lowest quantum state and can be described by a single wavefunction. This, therefore, lead to expression of macroscopic scaled quantum behaviour and coherence of particle in the BEC. Particles allowed to form a BEC are called 'bosons', and follow the Bose-Einstein statistics. The phase transition associated with the formation of a BEC can be interpreted in terms of the de Broglie wavelength, λ_{dB}

$$\lambda_{dB} = \sqrt{\frac{2\pi\hbar^2}{mk_BT}}, \tag{1.4}$$

where m is an atomic mass of the bosonic atom. k_B is the Boltzmann constant. T is the atomic cloud temperature. A suitable low temperature (T 10^2 nK) determines a large de Broglie wavelength which causes the overlap of the atomic wavefunction.

The onset of BEC corresponds to a phase-space density $\rho\lambda_{dB}^3$

$$\rho\lambda_{dB}^3 \geq 2.61, \tag{1.5}$$

where ρ is the atom number density.

In an isomeric BEC, because of coherence of the BEC, the decay of an isomeric nucleus can trigger collective emission of photons and the subsequent collapse of the BEC. The coherence of the emission burst strongly relies on the coherence of the BEC. Moreover, ultra-low temperature of the BEC can eliminate the Doppler broadening, leading to narrow emission linewidth.

A caesium isomer, ^{135m}Cs is a candidate for the abovementioned application, because it decays via emission of γ-photons. Moreover, sufficient long life-time of ^{135m}Cs ($T_{\frac{1}{2}} = 53$ minutes) allows for the BEC to be created, and it is not too long to observe gamma emission from the isomeric BEC. This was proposed by L. Marmugi, Ph. Walker and F. Renzoni in 2018 [31]. Additionally, a sufficient number of caesium isomers can be produced by ion implantation [32]. Measurements in [33] shown that, the ^{135m}Cs atoms production rate at the IGISOL facility is $\sim 9 \times 10^4$ atom/s which is adequate for a sensitive fluorescent imaging system.

The collective emission process of gamma photon from pure ^{135m}Cs BEC was identified, and the calculation results in [31] demonstrated that the number of emission photon exponentially depends on the initial density of isomer in BEC, within a range which is achievable in the laboratory. The identified mechanism provides a good chance of coherent gamma photons generation.

Laser cooling and trapping was identified as a tool to generate isomeric BEC. The proposed protocol relies on the extraction of implanted isomers from a neutraliser using resistive heating. Then, the isomer atoms are cooled and trapped by a magneto-optical trap (MOT). Finally, a sub-Doppler cooling technique will be applied to cool the isomer down to BEC temperature. In case of stable caesium, a BEC can be obtained by evaporative cooling in a tightly focussed dipole trap [34]. The technique induces massive atomic loss, which will be prohibitive for a low initial trapped number of ^{135m}Cs. Nevertheless, there is a suitable cooling technique

which can cool the atom down to the BEC state with a small atomic loss of 30%. It is degenerate Raman sideband cooling (dRSC), which was demonstrated with Rubidium-87 [35].

1.4 Laser cooling and trapping

1.4.1 Doppler cooling

Doppler cooling is the most common laser cooling technique used in cold atoms experiments. The cooling mechanism involves a velocity related atomic transition energy shift called "Doppler shift", ω_D given by

$$\omega_D = -k\dot{v} \ , \tag{1.6}$$

where k is the angular wave-number of a laser beam, and v is the atomic velocity.

The reduction of atomic kinetic energy generated by the cooling relies on photon absorption and spontaneous emission process of atoms. During the process, an atom absorbs a photon and experiences a momentum change in the radiation direction. In a spontaneous emission process, the atom also experiences momentum change; however, the net momentum change over several spontaneous emission processes is averaged to zero. The photon scattering rate is given by

$$R_{sc} = \frac{\Gamma}{2}\left(\frac{I/I_{sat}}{1+I/I_{sat}+(2\delta_{\pm}/\Gamma)^2}\right) \ , \tag{1.7}$$

where Γ is natural linewidth of atoms. I is laser intensity and I_{sat} is saturation intensity. The detuning term, $\delta_{\pm}$ indicates the laser frequency shift which is given by

$$\delta_{\pm} = \delta \pm \omega_D \ , \tag{1.8}$$

where δ is the laser frequency detuning.

According to equation 1.7, the scattering rate would peak in case of $\delta = -\omega_D$. In order to efficiently reduce the atomic velocity, a moving atom has to absorb photons propagating in the opposite direction. Thus, the laser frequency has to be

red detuned (negatively detuned from the atom's transition frequency). In this way, a damping force for the moving atoms is generated.

The extension of Doppler cooling in 3-Dimension is called 'optical molasses'. The optical molasses can cool the atom down to the Doppler limit [10] defined by the Doppler temperature T_D given by,

$$T_D = \frac{\hbar\Gamma}{2k_B} , \tag{1.9}$$

where k_B is the Boltzmann constant.

1.4.2 Magneto-optical trap

The magneto-optical trap (MOT) plays an essential role as a core technique for preparation and detection of cold caesium isotopes. Then, the cold atom sample can be cooled down below Doppler temperature using optical molasses and optical dipole trap [36][37].

The magneto-optical trap (MOT) is a combination of optical molasses [38] and a quadrupole magnetic field. To see how a MOT works, first, consider a two-level atom which has a ground state with the quantum number $F = 0$ and an excited state with quantum number $F' = 1$. The excited state has thus 3 degenerate magnetic sub-levels that correspond to $m_F = 0, \pm 1$.

The atoms are located in the quadrupole magnetic field gradient, which is produced by anti-Helmholtz coils. In the weak magnetic field gradient, the atoms experience a position-dependent Zeeman shift given by,

$$\Delta E_{|F,m_F\rangle} = \mu_B g_F m_F B_z , \tag{1.10}$$

where μ_B is the Bohr magnetron, g_F is hyperfine Landé g-factor, and B_z the magnetic field strength along the z-direction, which is linear around the centre of the trap $B_z = z\frac{\mathrm{d}B}{\mathrm{d}z}$. The energy splitting given by equation 1.10 is shown in figure 1.3. The atoms absorb σ_+, σ_- polarized light and then randomly emit photons which results in a friction force, and a restoring force towards the trap centre. Hence, the atoms in the trap region, i.e. the region where the polarised lights intersect, are

cooled and trapped.

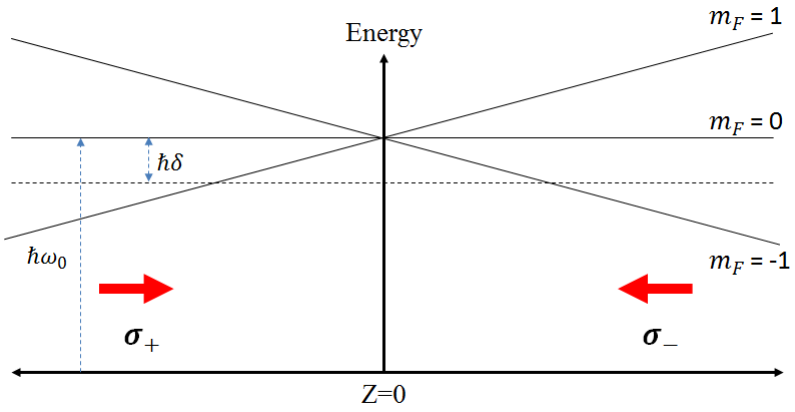

Figure 1.3: 1D scheme of the working principle of a magneto-optical trap.

The atomic motion in one dimension due to the radiative forces can be described by [39]

$$\frac{\mathrm{d}^2x}{\mathrm{d}t^2} = \frac{\vec{F}_+ + \vec{F}_-}{m} , \tag{1.11}$$

where x is the atom position and m the atomic mass. $\vec{F}_\pm$ is given by

$$\vec{F}_\pm = \pm\frac{\hbar\vec{k}\Gamma}{2}\left(\frac{I/I_{sat}}{1+I/I_{sat}+(2\delta_\pm/\Gamma)^2}\right) , \tag{1.12}$$

and the detuning term,

$$\delta_\pm = \delta \mp \vec{k}\cdot\vec{v} \pm \left(\frac{\mu_B(g_eM_e - g_gM_g)}{\hbar}\right)\left(z\frac{\mathrm{d}B}{\mathrm{d}z}\right) , \tag{1.13}$$

In the first term, δ is the detuning of MOT cooling beams. The second term describes the Doppler shift where $\vec{k}$ is the angular wave-vector and $\vec{v}$ is the atom's velocity. The third term is the Zeeman shift, where $\frac{dB}{dz}$ is the quadrupole magnetic field gradient. M_g and M_e is the magnetic quantum number for the considered ground state and excited state, respectively. g_g and g_e are the Landé g-factors and μ_B is the Bohr magneton.

The MOT population and background atom density are generally described by

the rate equations [40][41],

$$\frac{\mathrm{d}N_t}{\mathrm{d}t} = R - \gamma N_t - \beta \int n(\mathbf{r},\mathbf{t})^2 \mathrm{d}^3\mathbf{r} \ , \tag{1.14}$$

where R is the MOT loading rate, which is the number of atoms per unit time that a MOT can capture and discussed in section 4.5.1.1. β is two body loss coefficient [42], which affects the trapped atom number only in high trap density. In this work, the effect of β was taken into account. γ is the background collision loss coefficient [41] given by

$$\begin{aligned} \gamma &= \sum_i \sigma_{Cs,i} \bar{v}_i \\ &= n_{Cs} \sigma_{Cs,Cs} \bar{v}_{Cs} + n_b \sigma_{CS,b} \bar{v}_b \ , \end{aligned} \tag{1.15}$$

where n_{Cs} and n_b are caesium and non-caesium background density, respectively. $\sigma_{Cs,Cs} = 2 \times 10^{-13}$ cm^2 and $\sigma_{Cs,b}$ are caesium and non-caesium background collision cross-section respectively. For a vapour cell MOT, the background atom population is dominated by caesium atoms. Therefore, collision by non-caesium background atoms was neglected.

In this work, for a MOT population, $N_t > 10^4$ atoms, the MOT is in constant density regime [43][44]. In this regime, the MOT volume grows as the trapped atoms number increases in order to maintain a constant density. Therefore, the time-dependent MOT atom number is expressed by

$$\frac{\mathrm{d}N_t}{\mathrm{d}t} = R - \frac{N_t}{\tau} \ , \tag{1.16}$$

where $\frac{1}{\tau}$ is total effective loss coefficient [41], which relates to the average cloud density (n_0),

$$\frac{1}{\tau} = \gamma + \beta n_0. \tag{1.17}$$

By solving equation 1.16, the time-dependent MOT atom number is obtained:

$$N(t) = N_{sat} \left(1 - \exp(-t/\tau)\right) \tag{1.18}$$

where $N_{sat} = R\tau$ is the saturated atoms number in the MOT.

Chapter 2

Design and preparation of the laser system

A significant part of the first year of my PhD was devoted to the design, stabilisation and characterization of the cooling and repump lasers which were external cavity diode lasers in Littrow configuration, assembled in the UCL laboratory. The cooling laser power was amplified by a tapered amplifier to achieve sufficient power for the double magneto optical trap (MOT). The repump laser power was also amplified by using a master-slave configuration. Then, the laser system performance was evaluated with a MOT experiment. The optical setup for the ^{133}Cs also included the imaging system. A design for both absorption and fluorescence imaging was built and tested at UCL, the results confirmed that the lasers are powerful and stable enough to generate the double MOT, and for the subsequent stages of the experiment. The MOT cloud was real-time monitored by the fluorescence imaging.

2.1 External cavity diode laser and beam alignment

In this phase of the work, an external cavity diode laser (ECDL) in Littrow configuration [45][46][47][48] is used as the main laser source. A sketch of the laser cavities used in this work is shown in figure 2.1. The laser diode output beam is collimated by a lens and diffracted by a diffraction grating. When the first order of diffraction is reflected back inside the laser diode, optical feedback is provided to the laser from the external cavity. This introduces a further spectral selection to

the stimulated emission inside the semiconductor laser diode's chip. The optical feedback results into two main features: on the one hand, the emission of the laser diode becomes single mode (longitudinally); on the other hand, the wavelength, λ, of the laser cavity can be tuned by changing the incident angle, θ_i of laser beam to the grating surface normal. The diffraction condition is given by

$$m\lambda = 2d \sin\theta_i \tag{2.1}$$

where d is distance between the grooves of the diffraction grating and m is the diffraction order. The zero-order of diffracted light from the grating was used as an output beam.

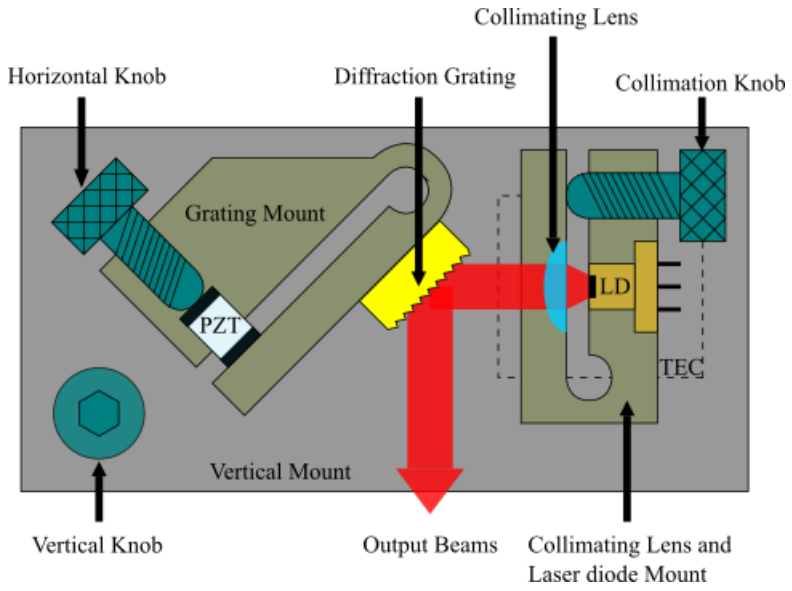

Figure 2.1: ECDL in Littrow configuration. The laser diode (LD) is mounted in an aluminium case, and the diode temperature is controlled by a thermoelectric cooling plate placed underneath the mount. A collimating lens collimates the diode laser beam. The beam collimation is achieved by the collimation nob controlled. A diffraction grating diffracts the laser beam (red), the zero diffracted order is an output beam, and the first order is diffracted back to the laser diode as feedback. The vertical knob is adjusted to optimise the laser feedback. The frequency of the output beam is roughly and finely controlled by the horizontal knob and piezoelectric actuator (PZT) driving voltage, respectively. The figure is not drawn to scale. A picture of ECDL in Littrow configuration used in this experiment is shown in figure D.1, appendix D.

The feedback from the first order diffracted light is a crucial part of the ECDL

alignment in term of laser wavelength tuning ability[47][49]. If the feedback is not optimised, the output wavelength of the diode laser will depend on the gain peak in the diode active medium and will not be finely tunable. In addition, instabilities will be produced, ultimately resulting in longitudinal multi-mode operation. As briefly anticipated, the spectral selectivity provided by the external cavity and the selected optical feedback allow for single mode operation of the laser. This is important in order to achieve fine control of the excitation of the atoms. The output power as a result of 1^{st} order feedback of the cooling laser is shown in figure 2.2: as it is clear from inspection of the graph, the optical feedback allows one to lower the laser threshold. This provides a practical method to test and improve the alignment of the external cavity: the optical feedback is optimum when - for given temperature and tuning - the threshold current reaches a minimum value.

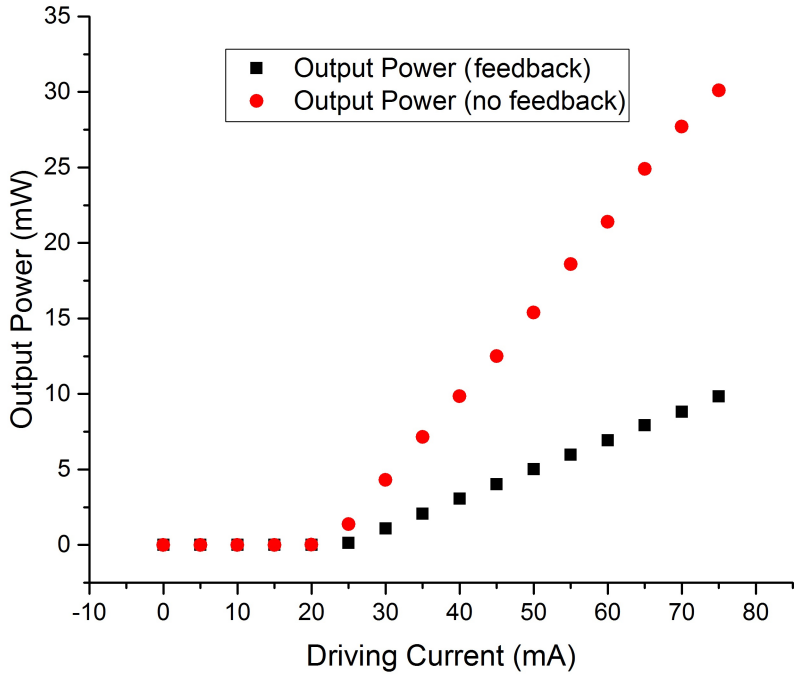

Figure 2.2: Cooling ECDL output power characteristic with/without optical feedback. The laser threshold current of 1^{st} order feedback and non-feedback laser are 22.0 mA and 25.5 mA, respectively.

Two ECDLs are required for the operation of the MOT used in the present

work. The first one is the so-called cooling laser which is used to slow atoms down in the magneto-optical trap. The second one is a repump laser which is used to pump off-cycle atoms back to the cooling cycle of the cooling laser. The lasers system scheme is shown in figure 2.3.

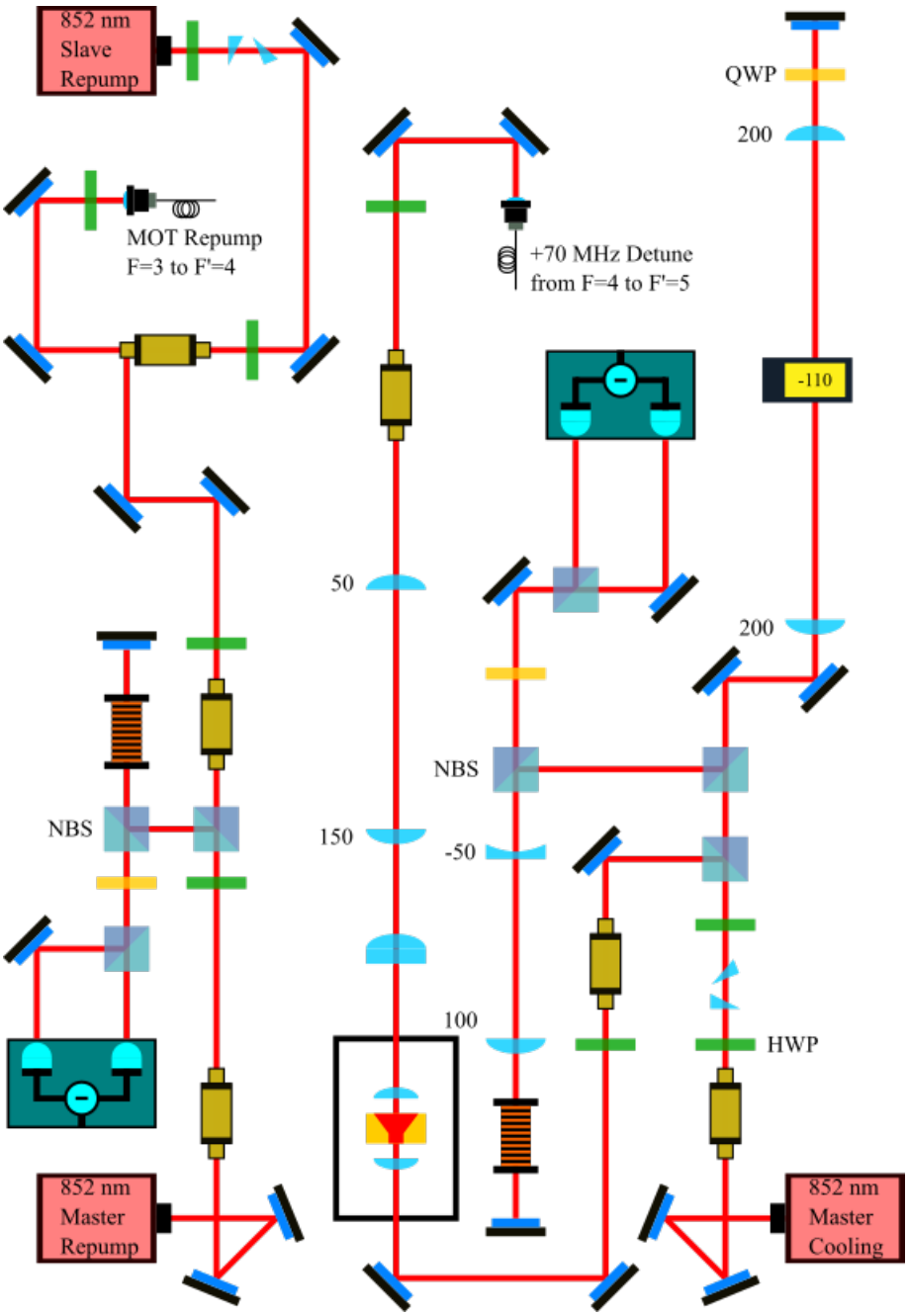

Figure 2.3: Scheme of the lasers system on the laser table. HWP is a half-wave plate, QWP is a quarter-wave plate, NBS is a normal beam splitter, PBS is a polarizing beam splitter and OIS is an optical isolator.A picture of the lasers system used in this experiment is shown in figure D.2, appendix D.

All lasers are protected from back-reflected laser light by optical isolators (OIS). The maximization of OIS transmitted optical power was done via two mirrors placed before the OIS. For the cooling laser, the beam profile is shaped from elliptic to circular by anamorphic prisms. Then, for both cooling and repump laser, the beam is split into two by a polarizing beam splitter (PBS). The power ratio of the beams emerging the PBS is controlled by rotating a half wave plate (HWP) in front of the PBS. The reflected vertical polarized beam is used as the input beam for a tapered amplifier and a slave laser in case of cooling and repump laser respectively for laser power amplification. The amplified laser outputs were injected into single mode polarization-maintaining optical fibers [50]. The transmitted horizontal polarized beam is sent to laser frequency control systems, based on a dichroic atomic vapor laser lock (DAVLL) spectroscopy.

2.1.1 Cooling laser

2.1.1.1 Cooling laser frequency control

The cooling laser is red detuned with respect to the transition frequency between the ground state $6^2S_{1/2}\ F = 4$ and the excited state $6^2P_{3/2}\ F' = 5$, where F and F' indicate hyperfine energy levels of the ground and the excited state respectively. Excited atoms within this transition are most likely to decay back to the $F = 4$ ground state, where they are re-excited to $F' = 5$. This allows the creation of a closed loop optical transition, which ensures continuous and efficient cooling of the atoms.

For caesium, the $F = 4 \rightarrow F' = 5$ transition peak is relatively small, which leads to a small capture range in DAVLL spectroscopy. Therefore the cooling laser is locked at the $6^2S_{1/2}\ F = 4$ to $6^2P_{3/2}\ F' = 4,5$ crossover frequency, which provides a larger capture range. Then, the laser frequency is shifted to the $F = 4$ to $F' = 5$ transition by using a 110 MHz double pass AOM and a 80 MHz single pass AOM, as described in detail in the following.

Firstly, the cooling laser is shifted by $-2f_{AOM1} = -2 \times 97\ MHz$, thanks to a double pass configuration AOM (Crystal technology, model: 3110-140), where f_{AOM1} is the acoustic frequency applied to the AOM crystal. Then, the output beam

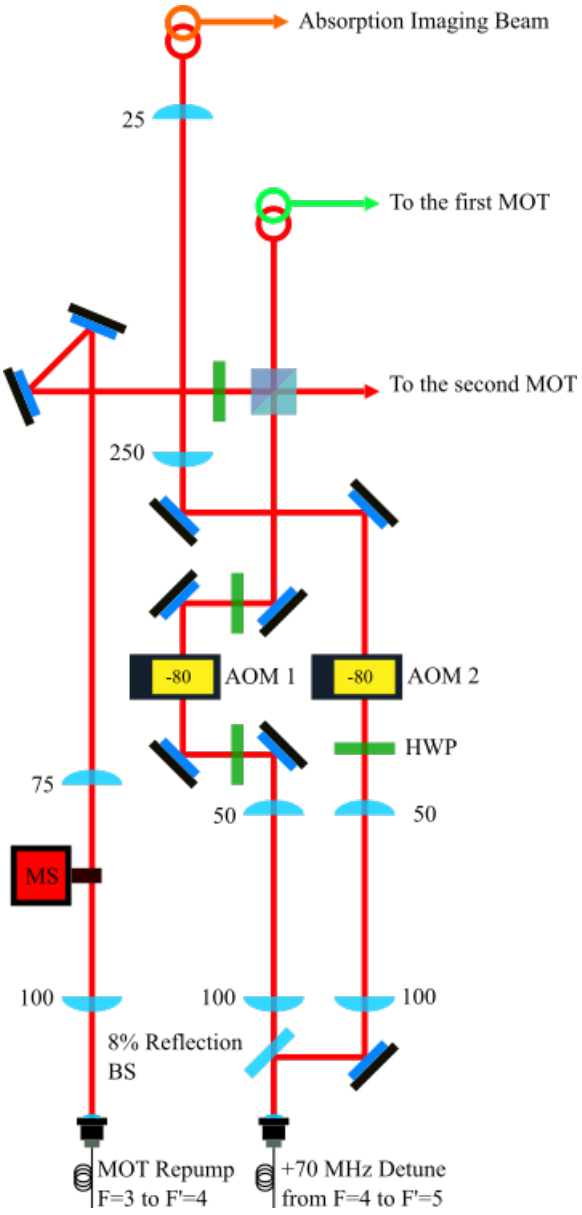

Figure 2.4: Scheme of the lasers system on the MOTs table. HWP is a half-wave plate, PBS is a polarizing beam splitter and MS is a mechanical shutter.

from the double pass AOM goes to the DAVLL spectroscopy section. Once the laser is locked, the frequency of the tapered amplifier's input beam is at $2f_{AOM1}$ detuned in the blue of the the crossover frequency. The output frequency of the MOPA is at the same frequency as the seed beam. The MOPA output beam is injected into a P3-780PM-FC-5 polarization-maintaining optical fiber, which transfers the light to the MOT table. The double-pass arrangement of the AOM allows fine tuning of the laser without displacement of the laser beam, unlike the case of single-pass

AOMs. However, the frequency shift provided by the 110 MHz AOM pushes the light above the desired frequency. Therefore, the laser frequency is shifted again (figure 2.4) by a single pass AOM (Crystal technology, model: 3080-122) modulated at $f_{AOM2} = 80\ MHz$. This shifts the laser's frequency down to the desired value, by using the -1^{st} order, i.e. achieving a -80 MHz further shift. This, in combination with the double-pass AOM, allows also fast switching and intensity control of the beam, without consequences on its frequency. Thanks to this arrangement, the cooling laser frequency is red detuned from the crossover frequency. The wanted detuning of the cooling laser can be achieved by a 110 MHz AOM and the modulation frequency can be calculated by,

$$f_{AOM1} = \frac{f_{AOM2} + \Delta f_{4,5\rightarrow 5} + \delta}{2} \tag{2.2}$$

where δ is the detuning of the laser, in this work $\delta = -2.2\Gamma$, Γ is the natural line width of the caesium $6^2P_{3/2}$ excited state, and $\Delta f_{4,5\rightarrow 5}$ is the frequency difference between $F' = 4,5$ crossover and $F' = 5$ transition. Therefore, the required driving frequency of the 110 MHz AOM is,

$$f_{AOM1} = \frac{80 + (251.091620/2) + (-2.2 \times 5.23413)}{2} \simeq 97 MHz\ .$$

2.1.1.2 Cooling laser master oscillator power amplifier (MOPA)

The trap laser intensity is a parameter that defines MOT performance. A higher intensity generate higher trapping force. According to equation 1.12, the trapping force saturates for $I >> I_{sat}$, where I_{sat} is the saturation intensity. Therefore, the trap laser intensity has to be larger than I_{sat}. Moreover, in order to reach the maximum number of trapped atoms in a MOT, the diameter of the cooling beams must be enlarged by telescopes, an operation which reduces the laser intensity. In this work, for 1.8 cm beam diameter, the minimum requirement of total trap beam power is above 78 mW which is more than the output of the ECDL used in this experiment (30 mW). Additionally, there are huge losses along the beam path between the ECDL and the MOT chamber. Therefore the power of the ECDL needs to be amplified.

A Master Oscillator Power Amplifier (MOPA) [51] offers a convenient solution. It is essentially a semiconductor device called tapered amplifier (TA) that amplifies the input (seed) beam within the gain region of a tapered chip. The output intensity is gained from electrical current injection (up to 3A typically) and is independent of frequency changes in the seed beam. The TA chip used in this work is the model m2k-TA-0850-2000 from m2k-laser GmbH, which amplifies light at 852 nm up to 2 W and comes in a DHP-F package as shown in 2.5 a.

The MOPA control system includes a current controller and a temperature controller. A simplified diagram of all parts combined together is shown in figure 2.5 b. The TA chip is placed in a copper case for heat dissipation. The case is placed on top of a thermo-electric cooler (TEC) plate which is connected to a temperature controller. The TEC cools the TA case down by transferring heat to a copper heat sink. The dynamic of the TA temperature depends on the injection current and the driving current of the TEC.

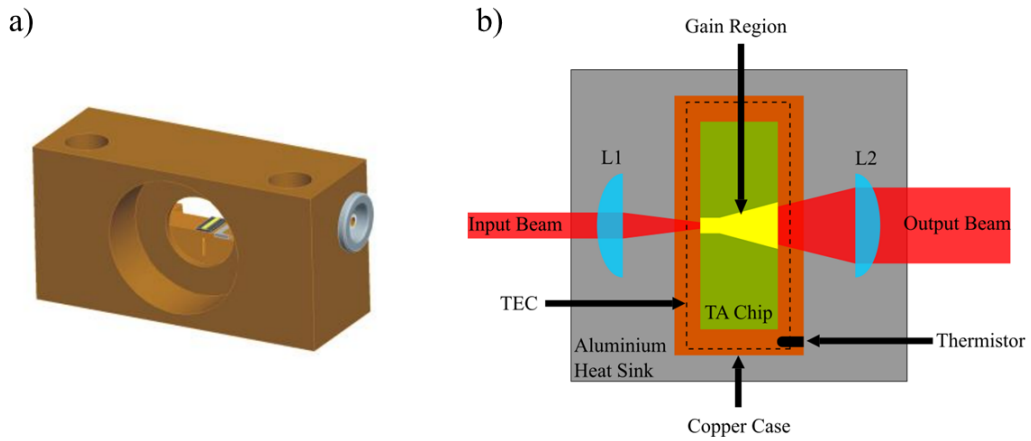

Figure 2.5: a) 3D sketch of a tapered amplifier chip in DHP-F package. b) Simplified sketch of the tapered amplifier for the MOPA configuration. A picture of the tapered amplifier used in this experiment is shown in figure D.3, appendix D.

When setting up the MOPA, there are two crucial alignments: the injection of the seed beam into the tapered chip and the optimization of the amplifier output beam profile.

Injection of MOPA seed beam The seed beam is steered by two mirrors and focused by a front collimating high numerical aperture (NA) lens. For a collimated

seed beam, the focal point of the lens has to be on the $125 \times 1.2\ \mu m^2$ TA chip input facet. In order to focus the beam on such a small area, the spontaneous emission light emitted from the TA input facet can be used as references for the alignment. The seed beam and the spontaneous emission beam must be overlapped. Moreover, spatial mode matching of the input beam and the spontaneous emission beam are required in order to obtain best injection condition. This forces the seed beam focal point and the TA input facet to be perfectly matched. Finally, the fine alignment of the seed beam input angle is done by the two mirrors until a relevant increase of output power of the MOPA is observed. The output power of MOPA depends on the beam polarization orientation, therefore a half wave plate is placed before the MOPA. Finally, an optical isolator is used to protect the seed laser from the TA spontaneous emission beam.

Optimization of the MOPA output beam profile The output beam of the MOPA is divergent, with different amounts of divergence from the parallel ($10^\circ - 12^\circ$) and perpendicular (50°) axis. As shown in figure 2.3, the beam is firstly collimated along the perpendicular axis by a plano convex large numerical aperture (NA) lens. Then a cylindrical plano-convex lens is used to collimate the output beam along the parallel axis. After that, the output beam size is reduced by a telescope to match the input aperture of a high power optical isolator (OIS). The optical isolator is used to protect the TA chip from back reflection light which come from the front surface of a fiber-port in which the beam is injected.

The output power of the MOPA is a good indicator of the correct alignment of the seed beam. To this purpose, the output power of the MOPA was investigated. The MOPA output power is shown in figure 2.6 as a function of the driving current for a given 16 mW seed power. The relation of spontaneous emission light of MOPA and MOPA driving current was also observed by measuring 0 mW seed MOPA output power. As the result show in inset of figure 2.6, the spontaneous emission power is very low compared with total output power and neglectable. The injection beam power dependence of MOPA output power was also observed and shown in 2.7.

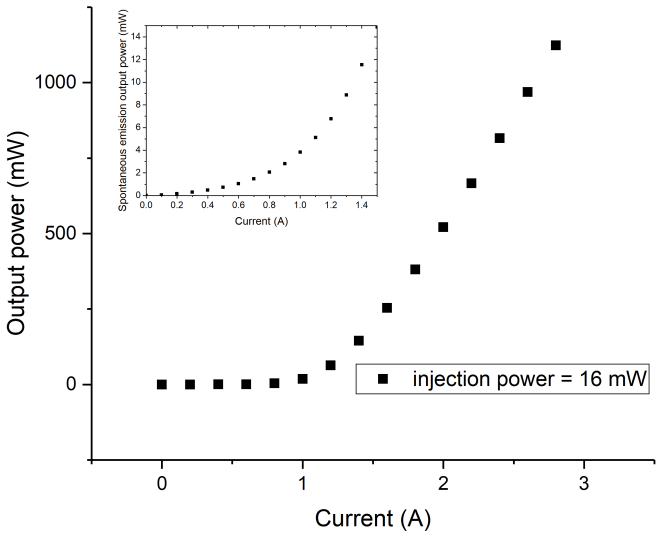

Figure 2.6: Driving current dependence of MOPA output power

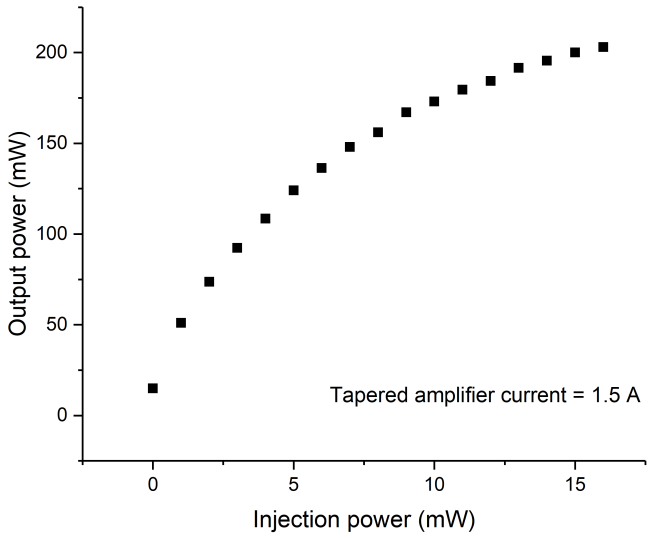

Figure 2.7: Injection beam power dependence of MOPA output power

2.1.2 Repump laser

In hyperfine optical pumping, which is produced by the red detuned cooling laser, there is a possibility that atoms are excited to the $F' = 4$ level and decay to the $F = 3$ ground state. A repump laser is used to transfer off-cycle atoms from the $6^2S_{1/2}$ $F = 3$ ground state to the $6^2P_{3/2}$ $F' = 4$ excited state. The off-cycle atoms

therefore have the possibility to decay back to $F = 4$ and take part to the cooling cycle again.

The detuning of the repump laser is zero and the capture range of the $F = 3 \rightarrow F' = 4$ transition from DAVLL spectroscopy is large enough for locking. Therefore, frequency tuning by AOM is not necessary. As shown in figure 2.3, the repump laser is split by a polarizing beam splitter (PBS). The vertical linear polarization beam is reflected into the DAVLL. The horizontal one is transmitted and will be used to inject a slave laser.

2.1.2.1 Master-Slave configuration of repump laser

The master-slave lasers configuration is a solution to increase the repump laser power available and maintain the stability of the laser frequency for the MOT. The configuration consists of two lasers. The first laser is called 'the master' laser, which has a stable output frequency and a narrow bandwidth but low optical power. The second laser is called "the slave laser" which has high optical power but less stable output frequency and broad bandwidth. In order to combine the advantages of those two laser, the slave laser is optically injected by the master laser. The stimulated emission in the slave laser active region generated by the master laser results in a reduction of the slave bandwidth and in an increase of the slave output power [52][53].

In our experiment setup, the slave laser is a SDL-5412-H1 852 nm single mode laser diode and the master is the ECDL repump laser previously described. The repump beam is split by a PBS, with the vertical linear polarization reflected into a DAVLL spectroscopy section and the transmitted beam used to inject the slave laser.

Injection of the slave laser The beam from the ECDL passes through an optical isolator which is used for protecting the diode from spurious light coming from the slave laser. Then, the repump beam is steered by two mirrors to the side port of the slave's optical isolator. The injection beam and slave output beam are overlapped, fine optimization of the injection point is done by the two mirrors until an increase of slave output power is observed after the optical isolator. The injection should be

done at low slave driving current, within the range 30-50 mA. The injection power of the slave is controlled by a half wave plate placed before the two mirrors.

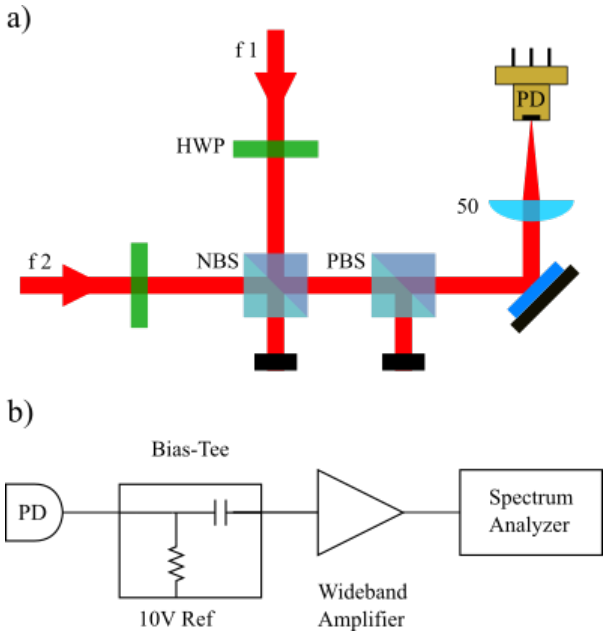

Figure 2.8: Heterodyne setup: a) Laser beams with frequencies f1 and f2 are overlapped by entering the normal beam splitter (NBS) and polarised by the polarising beam splitter (PBS). The overlapped beams are focused by a 50 mm plano-convex lens lead to an ultra-fast photo-detector (PD). The power of each beam is equalised by the half-wave plates (HWP). b) The PD signal is 10V bias using a bias-Tee and amplified by a wideband amplifier. Then, the amplified signal is measured by a spectrum analyser.

However, similar to the ECDLs, there are optimal values of current and temperature for the injection locking. In order to roughly identify the slave laser output frequency, the slave laser was beat with cooling laser in heterodyne setup as shown in figure 2.8a. The cooling, f1 and slave output f2 beam were spacial overlapped by a NBS, the power of each beam was balanced by HWPs and a PBS and the beams was focused by a 50 mm lens and the beat signal was detected by ultra-fast photo-detector (Hamamatsu, GaAs MSM Photo-detector G4176-03). In figure 2.8b, the beat signal between slave laser and cooling laser frequency from PD was $+10$ V bias by a bias tee (ZX85-12G-S) and 12 dB amplified by wideband amplifier (minicircuit, ZX60-14012L+), then the amplified signal was analysed by a spectrum analyser. The measurement was done at 125 mA of slave driving current, and result displayed in figure 2.9. The dominant beat signal is around 9 GHz which corre-

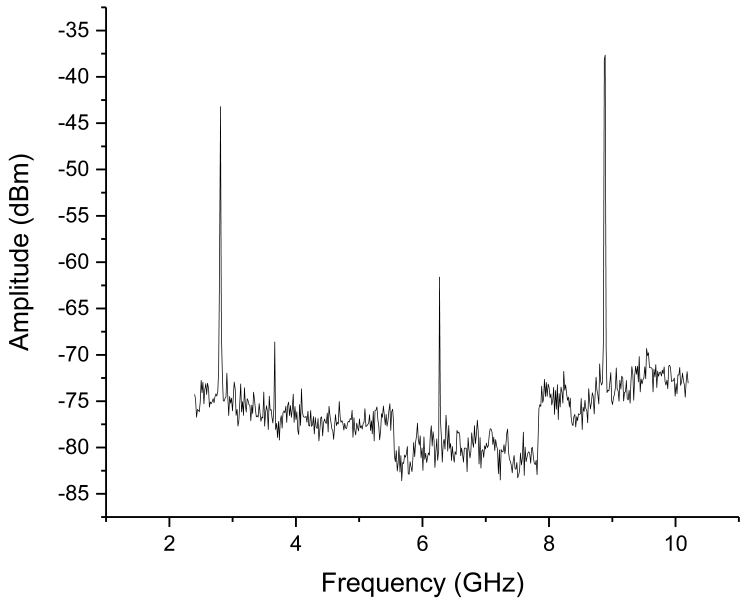

Figure 2.9: Slave output relative frequency modes: There are four measured modes of the beat signal of the slave repump laser and cooling laser (0.9 GHz, 3.75 GHz, 6.3 GHz and 9 GHz). The dominant mode of 9 GHz corresponds to frequency difference between cooling and repump frequencies using in this experiment.

sponds to the frequency difference between $6^2S_{1/2}F = 3$ and $6^2S_{1/2}F = 4$ and the 194 MHz frequency shift from double-pass AOM of cooling laser. Then, the saturated absorption spectroscopy of the slave laser was used to find the exact working point of slave laser by fine tuning of current and temperature of slave laser until a clear saturated absorption spectroscopy profile was observed.

2.2 Laser frequency stabilization

In cold atom experiments, Doppler free saturated absorption spectroscopy [54][46][47] is the basic technique for monitoring and stabilizing the laser frequency. Consider a vapour of three level atoms in one dimension. A laser probe beam propagates through a gas vapour reference cell onto a photo detector as shown in figure 2.10 a). As the laser frequency is scanned, the absorption of photons at the transition frequencies will cause a drop of the laser intensity at the photo detector. The absorption profile, recorded as the output signal of the photo detector,

is broadened because of the velocity distribution of the atoms in the reference cell, as shown in figure 2.10 b), as a consequence of the Doppler effect. As a result, the hyperfine transitions cannot be observed. These transitions can be revealed by adding an additional higher intensity counter-propagating "pump" laser beam, as shown in figure 2.10 c). Non-zero velocity atoms interact mostly with either the probe beam or with the pump beam, depending on their velocity and pump-probe relative intensity. However, atoms with a zero velocity component along the propagation direction of the lasers can interact with both beams regardless of the Doppler effect and most of the atoms at rest are excited by the pump beam because of its high intensity. The low probability of the probe beam to excite the atoms at rest leads to an increase of the probe transmission superimposed on the broad structure in the absorption profile, as shown in figure 2.10 d). This spectroscopy is called "Doppler-free saturated absorption spectroscopy", as it allows to overcome the Doppler broadening and observe resonances with natural linewidth.

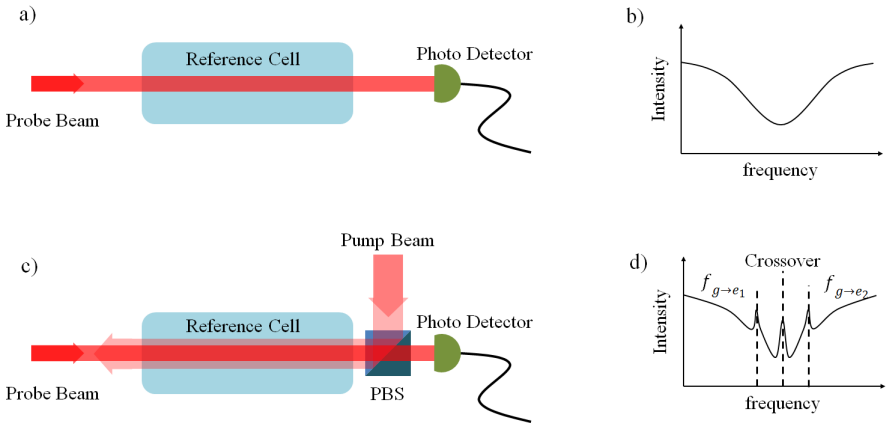

Figure 2.10: Absorption spectroscopy set-ups with and without pump beam and corresponding probe absorption profiles. a) Atoms in the reference cell are absorbed only by a probe beam. b) Broad absorption profile observed by the photo-detector in a). c) Atoms in the reference cell are absorbed by the probe and pump beams. d) Doppler-free saturated absorption profile observed by the photo-detector in c).

The Doppler-free saturated absorption profile is used to lock the laser frequency at the wanted value. The locking can be done simply by using a servo-lock. The "error signal", i.e. the difference of the set-point signal and the locking

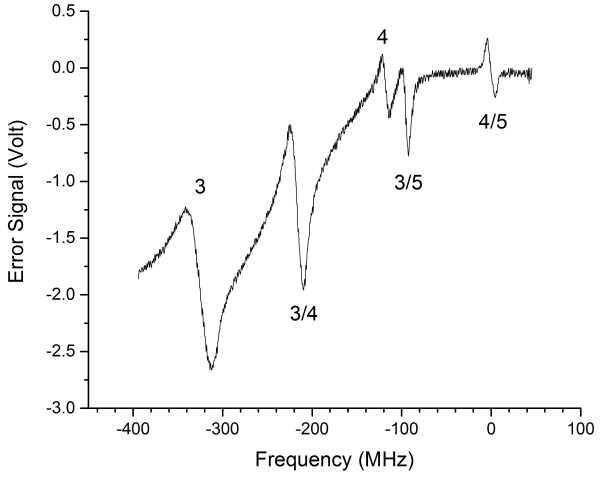

Figure 2.11: Cooling laser DAVLL Doppler-free saturated absorption spectroscopy signal of the ^{133}Cs D2 line $6^2S_{1/2}F = 46^2P_{3/2}$ transition. The numbers in the figure indicate the excited state hyperfine level, F' of the observed transitions, and the crossovers.

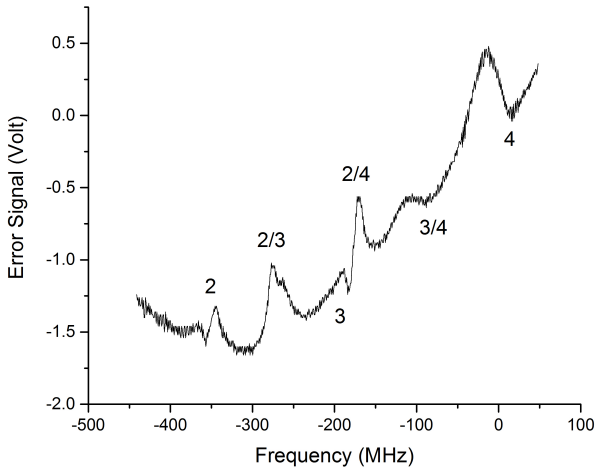

Figure 2.12: Repump laser DAVLL Doppler-free saturated absorption spectroscopy signal of the ^{133}Cs D2 line $6^2S_{1/2}$ $F = 3$ ground state to $6^2P_{3/2}$ excited state. The numbers in the figure indicate the excited state hyperfine level, F' of the observed transitions, and the crossovers.

point signal in the absorption profile, is used as a input of the servo-lock [55][47]. The error signal is amplified and then a negative feedback is used to maintain the magnitude of the error signal to zero.

However, for normal Doppler-free saturated absorption profile, the probe trans-

mission intensity cannot be directly used as error signal as it does not provide a slope at the locking point, i.e. at the peak of the profile.

Therefore, in this work, the diode lasers frequency is stabilised by the sub-Doppler dichroic atomic vapour laser lock (DAVLL) technique, which provides a linear error signal at the transition peak [56][57]. The DAVLL employs a weak homogeneous magnetic field to lift the degeneracy of the Zeeman magnetic sublevels of the atoms, thus producing unbalanced absorption between the σ_+ and σ_- polarization components of the linearly polarized probe beam [57]. In other words, the Doppler-free saturated absorption profiles of the σ_+ and σ_- components are shifted in opposite directions on the frequency axis. After transmission through the atomic vapour, the σ_+ and σ_- polarization components are transformed into vertical and horizontal linear polarizations by a quarter wave plate, and then separated by a PBS. The intensities of the split beams are measured by two photo detectors. The two signals are amplified and subtracted from each other. This produces a signal with a linear slope at the transition frequency, suitable for laser locking as shown in figure 2.11 and 2.12 for cooling and repump laser, respectively.

In the set-up of my experiment, the beam going toward the caesium vapour reference cell is considered as a pump beam. Then, after passing through the cell, the beam is retro reflected back to the cell. The retro reflected beam is considered as a probe beam because it has lower optical power due to losses from the cell surfaces and a mirror.

2.3 Experimental setup for MOT

2.3.1 The vacuum system

In this part of the work, a double chamber setup (shown in figure 2.13) for laser cooling and trapping of ^{133}Cs was used. Vacuum system for this experiment consists of two parts, upper and lower.

The upper part comprised a chamber, a CF40 metal valve, a Varian StarCell 20 l/s ion pump and caesium metal dispensers. All the component are connected by a six ways cross. The chamber is a six ports metal cube with optical windows. It

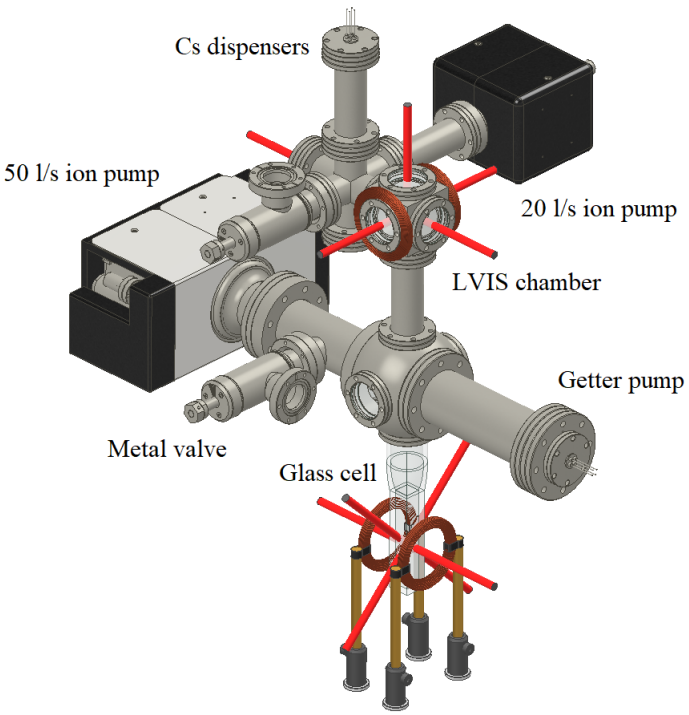

Figure 2.13: Vacuum system for double ^{133}Cs MOT are consisted of two following parts: 1) LVIS chamber where the first MOT is loaded from background Cs supplied by the Cs dispensers. The high vacuum (HV) pressure in the upper chamber is maintain by a 20 l/s ion pump. 2) Glass cell where the second MOT is loaded from pre-cool atoms transferred from the LVIS chamber. The ultra-high vacuum (UHV) pressured in the glass cell is generated by a 50 l/s ion pump and a getter pump. A picture of the vacuum system is shown in figure D.4, appendix D.

is used for vapour cell MOT (VCMOT) loading. The dispensers provide caesium atom vapour for the VCMOT. The metal valve was use as pre-evacuation valve and the pressure of $\leq 10^{-7}$ mbar in the VCMOT chamber was maintained by the 20 l/s ion pump.

The second chamber is constituted by a glass cell, a non-evaporative getter (NEG) pump and an ion pump. The Pyrex glass cell with square cross-section (2×2 cm^2), is connected to the vacuum system by a steel CF40 flange. The getter pump and the 55 l/s ion pump were operated to maintain the ultra-high vacuum (UHV) pressure in the glass cell. All the components in the lower part of the system were attached to a spherical square connector.

The two parts of the system were attached to a blank CF40 flange with $\phi = 1.5$ mm hole which works as vacuum impedance. Differential vacuum and two ion pumps ensure about 3 orders of magnitude decrease of the residual pressure in the glass cell reaching a pressure lower than 10^{-10} mbar.

2.3.2 MOT's optical alignment

In the first vacuum chamber, a MOT from a thermal vapour produced by metal dispensers is realised. Trapped atoms from the first MOT were optically transferred to the second chamber. In this glass cell, the pre-cooled atoms were trapped again by a MOT.

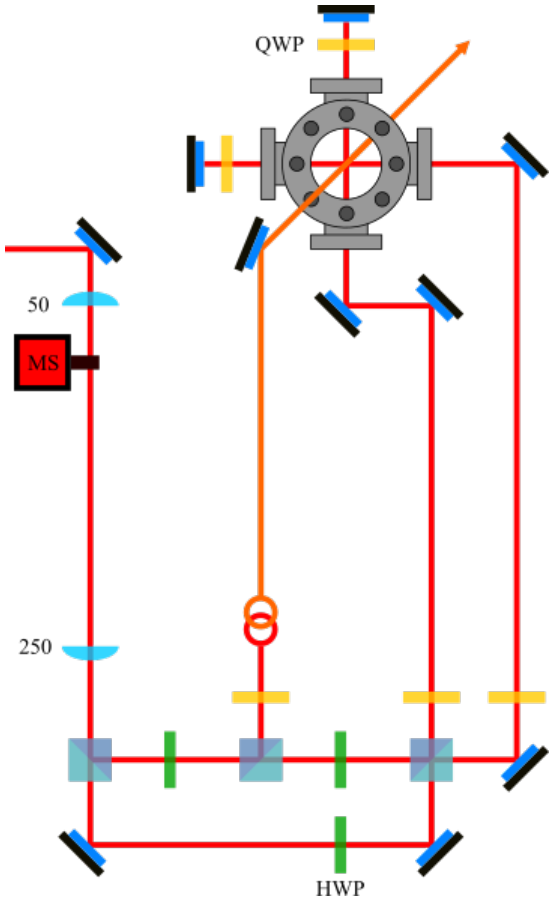

Figure 2.14: Optical alignment of the first chamber (LVIS chamber). HWP is a half-wave plate, QWP is a quarter-wave plate, PBS is a polarizing beam splitter and MS is a mechanical shutter.

The first MOT is arranged in the so-called Low Velocity Intense Source (LVIS) configuration [58]. This allows the creation of a collimated beam of pre-cooled

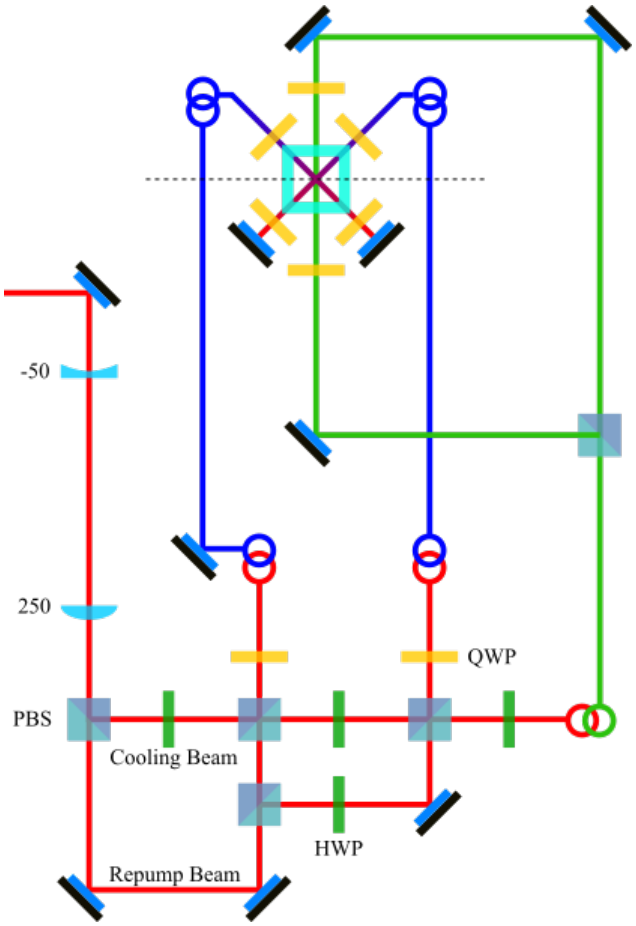

Figure 2.15: Optical alignment of the second chamber (science MOT chamber). HWP is a half-wave plate, QWP is a quarter-wave plate, and PBS is a polarizing beam splitter.

atoms, which serves as a source for the MOT in the second chamber. In this configuration, one of the mirrors of the first MOT is substituted by a 1" mirror with a central hole of 1.5 mm, glued inside the vacuum chamber. Because of the hole, a dark column is created within the first MOT volume, where atoms experience unbalanced radiation pressure. As a consequence, atoms are pushed from the centre of the first MOT towards the second chamber.

In the first MOT setup, overlapped cooling and repump beams diameter are enlarged by a telescope which consists of a $\phi = 1$", $f = 50$ mm plano convex lens and a $\phi = 1$" $f = 250$ mm plano convex lens, to 1.0 cm and 1.5 cm diameters, respectively. A mechanical shutter (MS) was placed at the focal point of the telescope. At this position, the MS is a controlled switch of the first MOT beams. After the tele-

scope, the overlapped beams are split by a PBS into cooling beam (PBS's reflected component) and repump beam (PBS's transmitted component). The cooling beam was split into three beams and the repump beam was split into two beams which later overlap with the two cooling beams in the horizontal plane. The power of the beams was controlled by three HWPs placed in front of the PBS as shown in figure 2.14

In the second chamber, atoms coming from the LVIS are again captured by lasers and trapped in a second MOT based on a standard six-beam configuration, as sketched in figure 2.15. The second MOT beam alignment is similar to the first MOT's. Moreover, for the second MOT, the repump beams are applied in all three directions.

2.3.3 MOT's imaging setup

In this experiment, an optical system was designed for fluorescence and absorption imaging. Fluorescence imaging is a method based on collecting spontaneous emission from an atomic sample. This imaging technique is useful for detection of low density cold atomic cloud [59][60]. Moreover, fluorescence imaging is a non-destructive measurement. Therefore, the fluorescence imaging method was used for MOT real time monitoring. Absorption imaging is destructive in nature. The imaging was used to measure MOT's properties, trap atom number and temperature. The optical system arrangement is shown in figure 2.16.

The number of atoms trapped in the MOT, and their temperature, are measured by absorption imaging. The absorption imaging is implemented by means of a resonant probe laser beam: the radiation interacts with the trapped atoms, which absorb photons, thus casting a shadow in the beam transmitted through the atom cloud. The transmitted beam is magnified by an objective lens and detected by a CCD camera (2.16). The variation of the probe beam due to the transmission through the atom cloud can be related to the cloud atomic density. In practice, a position-dependent decrease of the transmitted light is produced, which allows for the reconstruction of the density distribution of the atomic cloud.

In our set-up, the probe beam for absorption imaging is derived from the MOT

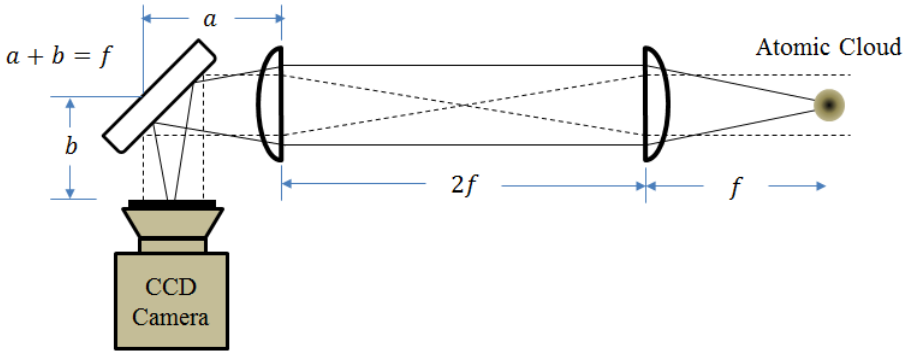

Figure 2.16: MOT Imaging system is consisted of three following parts: a) 1:1 ratio telescope which collect spontaneous emission photons from MOT cloud or probe photons from an absorption imaging beam. b) a $\phi = 1$" dielectric mirror is used to reflect the imaging beam from the telescope to the camera's CCD array. c) CCD array of CCD camera which is placed at focal point of the telescope's eyepiece lens. A picture of the MOT imaging system used in this experiment is shown in figure D.5, appendix D.

cooling beam by using a 8% reflection beam splitter (figure 2.4). In order to have the probe beam on resonance with the $F = 4 \rightarrow F' = 5$ transition, an 80 MHz AOM is added in order to shift the frequency into resonance, and to be able to quickly switch on and off the probe beam. The beam diameter is increased to 2 cm by a telescope.

The imaging system consists of a pair of $f = 100$ mm 2" plano-convex lens, a dielectric mirror and a CCD camera (PCO Pixel Fly). The imaging system was designed to allow for both absorption (dashed line) and fluorescence (solid line) imaging by using a single camera. The lens pair forms a 1:1 objective lens. A collimated probe beam is transmitted through the atomic cloud into the objective lens, and is focused at the middle point between the two lenses. An $\phi_{max} = 1$" iris was place at the focal point of the telescope. In fluorescence imaging, the iris is wide open, while the iris hole diameter, ϕ will be set to $\phi < 1.0$ mm for absorption imaging in order to reduce the amount of stray light that goes to CCD array. Moreover, the imaging beam path from the science glass chamber to the CCD camera was also covered by $\phi = 1$" black cylindrical tube to prevent background light and dust. After the objective lens, a mirror was placed in front of the CCD camera for the positioning of the MOT cloud image on the CCD array, the probe beam is reflected

by the mirror into the CCD camera, placed 100 mm from the objective lens.

2.4 Results and conclusion

An image of MOT in the glass cell, shown in figure 2.17, was captured by fluorescence imaging. The MOT cloud radii in two orthogonal directions, $\sigma_x = 0.427 \pm 0.007$ mm and $\sigma_y = 0.448 \pm 0.013$ mm respectively, are obtained by Gaussian fit of counts on CCD array. In this way, we define the radius as the standard deviation of the Gaussian distribution fitting the the sum of pixel values along a given axis. The laser system working point in term of frequency, power and beam size of laser for a MOT are reported in table 2.1.

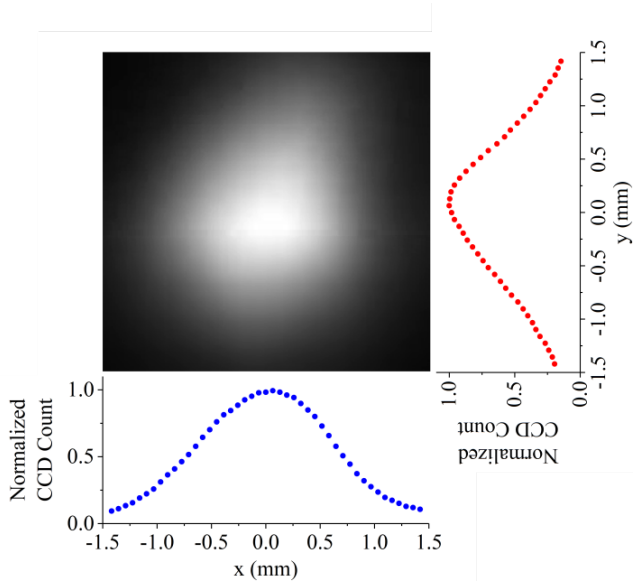

Figure 2.17: Fluorescence image of a ^{133}Cs MOT. The two insets show the distribution of the sum over columns (rows) of the pixel counts. A picture of the MOT observed by an infrared camera placed near the science cell is shown in figure D.6, appendix D.

Laser	transiton ($F_g \rightarrow F_e$)	detuning (Γ)	Power (mW)	Diameter (cm)
Cooling	$4 \rightarrow 5$	-2.2	11.0	1.0
Repumping	$3 \rightarrow 4$	0.0	2.4	1.5
Imaging	$4 \rightarrow 5$	0.0	0.5	2.0

Table 2.1: Laser parameters for the operation of the MOT and the imaging system.

Chapter 3

Cold atom system for cooling and trapping of Caesium isotopes and isomers

The experiment was transferred and installed in the Accelerator Laboratory of the University of Jyväskylä (Finland). In the laboratory, there is the ion guide isotope separation on-line (IGISOL) facility which will provide the source of isotopically selected ^{135m}Cs necessary for the long-term goal of the project.

A vapour cell MOT experiment was setup to test the laser system in new and challenging environment. The experiment mainly comprised vacuum system, the upgraded laser system and MOT time sequence control system. The MOT was characterised by absorption imaging.

3.1 Vacuum system

The single chamber vacuum system used in this experiment is illustrated in figure 3.1. The arrangement is that of a conventional 3D MOT with three pairs of cooling and repumper beams, and anti-Helmholtz coils [61].

The vacuum chamber is a $5 \times 8 \times 15$ cm^3 Pyrex cell which was connected to a CF40 tee via a CF40 metal to glass connector. The ultimate vacuum pressure of 10^{-10} mbar was achieved by a Varian Starcell 20 l/s ion pump which was attached to the CF40 tee via a CF40 straight nipple. An ampoule of pure ^{133}Cs was also

installed as a source of alkali vapour (reservoir). The liquid reservoir was contained inside a dedicated CF16 straight tube, delimited by a CF16 valve. The valve was used as ^{133}Cs vapour density controller.

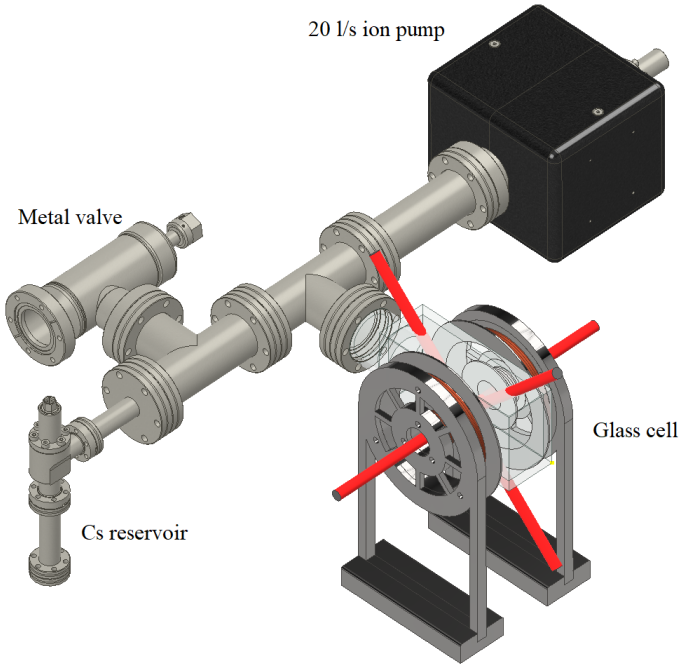

Figure 3.1: Vacuum system and anti-Helmholtz coils setup for the vapour cell MOT of ^{133}Cs. The MOT in the glass cell is loaded from background Cs supplied by liquid Cs contained in a reservoir. A 20 l/s ion pump maintains the high vacuum (HV) pressure. The anti-Helmholtz coils are placed around the glass cell. Red columns are MOT beams that are orthogonally aligned to each other. A picture of the vacuum system for single ^{133}Cs MOT and optical setup are shown in figure D.8, appendix D.

3.2 Upgrade of the laser system

The laser system for this experiment was an upgrade of the transferred system, described in chapter 2. Therefore, only the main differences and improvements are reported here.

The two home built Littrow configuration ECDLs were replaced by commercial cat eye configuration ECDLs [62][63][64][65] with 60 mW output power at 852 nm (RadiantDyes NarrowDiode). The alignment of the cat eye configuration ECDLs is shown in 3.2. Among the advantages of this configuration over conven-

tional ECDLs, we mention the independence of the laser wavelength selection from the optical feedback, leading to a lower sensitivity of the wavelength and the feedback to misalignments. Instead of using a diffraction grating, the laser frequency of the cat's eye ECDL is controlled by an intra-cavity narrow band-pass interference filter. Tuning is achieved by varying the angle of the filter with respect to the incident beam (6 degree for 852 nm). The transmitted beam goes to a Keplerian telescope where the beam is partially reflected back to the laser diode as a feedback by an output coupler (partially reflective mirror), which is placed at the focal point of the telescope. The transmitted beam is collimated by an output lens of the telescope as an output beam. Fine tuning for the laser frequency is obtained by changing the cavity length. This is controlled by applying a voltage to a ring piezo-electric transducer attached to the output coupler.

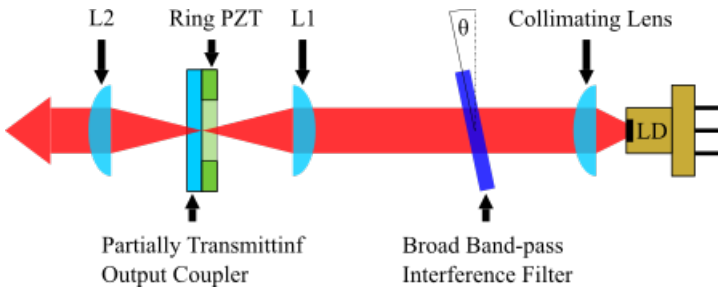

Figure 3.2: Cat eye configuration ECDL. The laser diode (LD) is mounted in an aluminium case, and the diode temperature is controlled by a thermoelectric cooling plate placed underneath the mount. A collimating lens collimates the diode laser beam. The beam collimation is achieved by the collimation nob controlled. A diffraction grating diffracts the laser beam (red), the zero diffracted order is an output beam, and the first order is diffracted back to the laser diode as feedback. The vertical knob is adjusted to optimise the laser feedback. The frequency of the output beam is roughly and finely controlled by the horizontal knob and PZT driving voltage, respectively. The figure is not drawn to scale.

The emission wavelength of the laser, $\lambda(\theta)$ is given by [63],

$$\lambda(\theta) = \lambda_0 \sqrt{1 - \frac{\sin^2\theta}{n_{eff}^2}}\,, \tag{3.1}$$

where θ is the angle of incidence of the beam on the interference filter. λ_0 is the output wavelength for nominal incidence. n_{eff} is effective refractive index of the filter. Thus, the wavelength sensitivity due to the angle misalignment of the filter is

given by

$$\frac{\mathrm{d}\lambda(\theta)}{\mathrm{d}\theta} = \left(\frac{\lambda_0}{n_{eff}^2}\right)^2 \frac{\sin(2\theta)}{2\lambda(\theta)} \,. \tag{3.2}$$

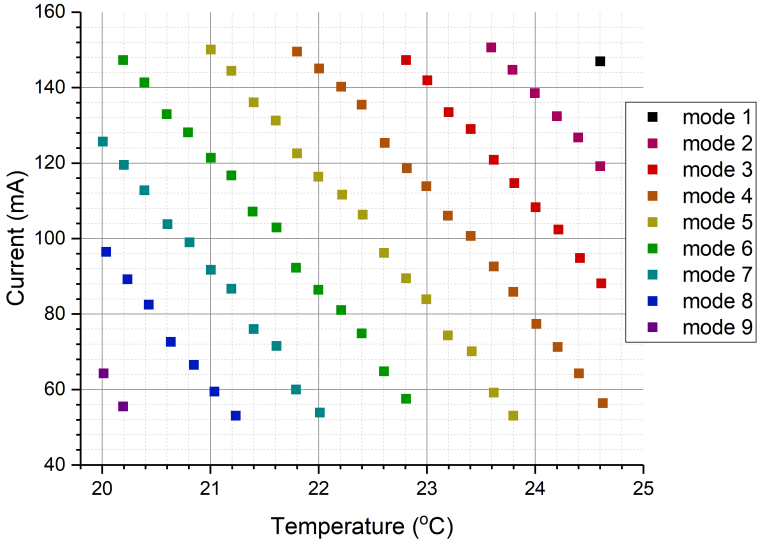

Figure 3.3: ECDL cooling laser working points

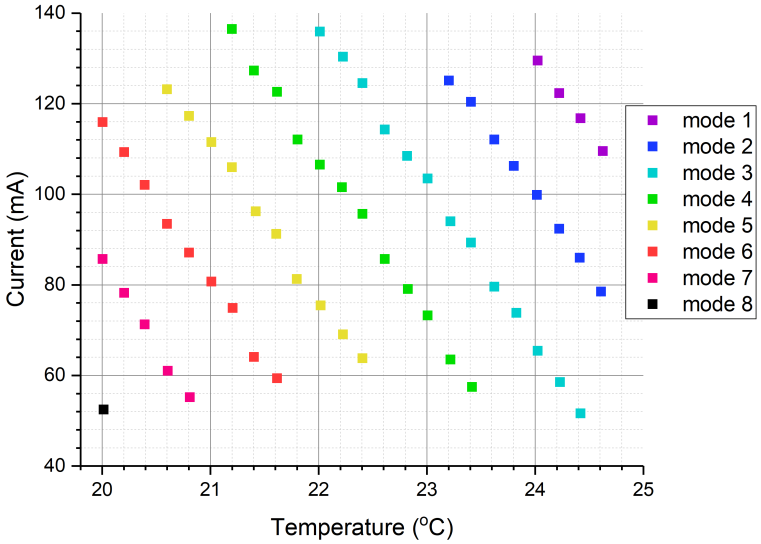

Figure 3.4: ECDL repumping laser working points

After installation, the lasers were driven by 0-150 mA DC current. The laser temperature was initially set at 22 ^{o}C. Then, the current and temperature were scanned until the DAVLL spectroscopy was observed ($F = 4$ to F' for MOT cooling and $F = 3$ to F' for MOT repumping). The scanning was operated on current-temperature grid in a range of 50-150 mA and 20-24 ^{o}C, 0.2 ^{o}C step. The working current and temperature of the cooling and repumping ECDLs were identified and shown in figure 3.3 and 3.4, respectively.

In the figures, there are modes of working points located on the T-I space. A working point in a mode can be moved continuously by changing current and temperature. Additionally, by considering a certain diode temperature or driving current, mode hopping occurs because the active region's refractive index of the diode is affected by the change of driving current and temperature of the laser diode [66][67].

3.3 MOT measurements

The MOT properties were determined by absorption imaging. To this purpose, the imaging sequence needs to be processed with millisecond-level accuracy. Therefore, a National Instruments NI6009 DAQ module was installed and controlled by Labview 2015.

3.3.1 Absorption imaging

Absorption imaging is a method that measures collimated beam's profile of near resonant light that passes through an atomic cloud. The beam is partially absorbed by the cloud so that the atoms "cast a shadow" pattern on a camera's CCD array.

To measure the spatial distribution of the MOT atomic density, the contribution from atomic absorption has to be isolated. This can be done by taking a sequence of 3 different images as shown in figure 3.5.

To determine the atomic distribution, the probe beam intensity is extracted from each image. Suppose that (x,y) are the spatial coordinates on the image plane, the intensity of the beam extracted from MOT, light and dark images are denoted by $I(x,y)$, $I_0(x,y)$ and $I_{BG}(x,y)$, respectively.

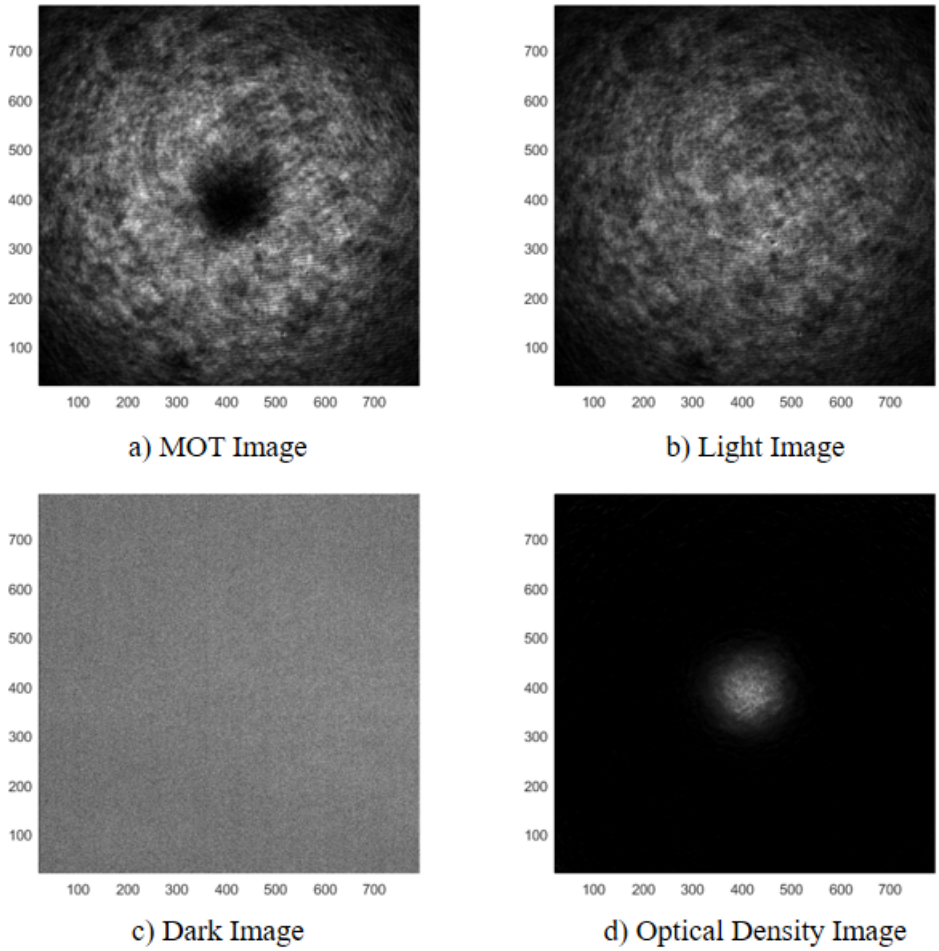

Figure 3.5: Images required for MOT absorption imaging described according to imaging sequence. a) MOT image: a shadow cast on the probe beam after transmission through the atomic cloud. b) light image: the intensity profile of the probe beam in the absence of the atomic cloud. c) dark image: an image of the background intensity profile as measured in the absence of probe beam and atomic cloud. d) optical density image of MOT: the spatial distribution of the ensemble obtained by equation 3.4 and 3.7.

The first image - commonly referred to as the ”MOT image” - represents the intensity profile $I(x,y)$ of the probe beam after interaction with the atomic cloud. The second image is the intensity profile of the probe beam in the absence of the atomic cloud, $I_0(x,y)$ and the third is the background intensity profile $I_{BG}(x,y)$, as measured in the absence of probe beam and atomic cloud.

For simplicity, we can consider a single pixel of the CCD camera, with coordinates (x,y). The transmitted intensity I can be related to the incoming intensity I_0

via Beer's law [68][69],

$$I(x,y) = I_0(x,y)e^{-O.D.} \tag{3.3}$$

where $O.D.$ is the optical density of the cloud, which is related to the atom column density, $n(x,y)$ via

$$O.D. = n(x,y)\sigma \ . \tag{3.4}$$

Here σ is the absorption cross section [24], given by

$$\sigma = \frac{\sigma_0}{1+4(\frac{\omega-\omega_0}{\Gamma})^2+\frac{I_0}{I_{sat}}} \tag{3.5}$$

where ω_0 is the resonance frequency and ω is the probe frequency, Γ the natural decay rate of the excited state, I_{sat} the saturation intensity which depends on the probe beam polarization and σ_0 the on-resonance absorption cross section given by

$$\sigma_0 = \frac{\hbar\omega_0\Gamma}{2I_{sat}}. \tag{3.6}$$

In order to eliminate the unwanted contribution from stray light from the background, I_{BG} has to be subtracted from both $I(x,y)$ and $I_0(x,y)$. Then, the expression for the column density, as from equations 3.3 and 3.4, becomes

$$n(x,y) = \frac{1}{\sigma}\ln\left(\frac{I_0 - I_{BG}}{I_\omega - I_{BG}}\right) \ . \tag{3.7}$$

3.3.1.1 MOT temperature measurement

The MOT temperature is determined via the technique of time of flight [70][71]. This consists in letting the atom cloud freely expand and then taking images of the cloud at several different expansion times. To discuss the details, we can consider a 1D case, and indicate by x the distance from cloud centre. At a given time t, the distribution of the column density, $n(x,0)$ obeys the Boltzmann distribution

$$f(x) = \frac{1}{\sqrt{2\pi}\sigma(t)}\exp\left(-\frac{x^2}{2\sigma^2(t)}\right) \tag{3.8}$$

where σ is the standard deviation or cloud radius. By introducing m, the atomic mass and T, the temperature, the time evolution of the cloud radius [70][71][72] is given by

$$\sigma(t) = \sqrt{\frac{k_B T}{m} t^2 + {\sigma_0}^2}\,, \tag{3.9}$$

with σ_0 the initial cloud size. Thus, by measuring the cloud size σ at different times t, it is possible to derive the atomic cloud temperature from equation 3.9 as,

$$T = \frac{m}{k_B T}\left(\frac{{\sigma_1}^2 - {\sigma_1}^2}{{t_2}^2 - {t_1}^2}\right)\,, \tag{3.10}$$

where t_1, σ_1 and t_2, σ_2 are MOT expansion times and cloud sizes at these times.

3.3.1.2 MOT atoms number and density measurement

The estimated number of trapped atoms, N can be obtained by

$$N = \int_{-\infty}^{\infty}\int_{-\infty}^{\infty} n(x,y)dxdy \simeq A_{pixel} \sum_{all\ pixels} n_{pixel} \tag{3.11}$$

where A_{pixel} is the area of a single pixel of the CCD camera and n_{pixel} is the column density of each pixel.

For a high-density MOT and on resonance probe frequency, the column density can be saturated because all the probe photons were absorbed by excessive number of atoms in a column. The saturation causes the measured atom number to be lower than the actual atom number. In order to achieve accurate MOT atom number, the frequency of the probe laser needs to be detuned from resonance. The detuning decreases the absorption cross-section, thus a reasonable amount of probe photons can travel through the cloud and are detected by the CCD array.

In this work, the probe detuning was increased until the saturation of the optical density was not observed any more. For a given detuning, the atom number is calculated as discussed in section 3.3.1 using equation 3.11. However, one can also empirically calculate the column density by a rescaling function, $f(\omega)$ given by

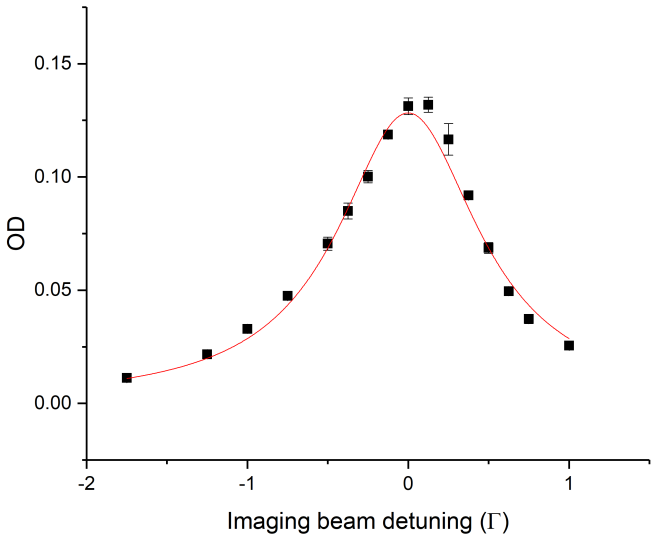

Figure 3.6: Optical density as a function of imaging beam detuning. The fit of the data (red curve) with the rescaling function (equation 3.12) provides $a = 0.15 \pm 0.01$ and $b = 0.15 \pm 0.08$. Reduced chi-square of the fit, $\chi^2_{red} = 6.376$.

$$f(\omega) = \frac{a}{1 + 4\left(\frac{\omega - \omega_0}{\Gamma}\right) + b}, \tag{3.12}$$

where $a = 0.15 \pm 0.01$ and $b = 0.15 \pm 0.08$. The function was obtained by the relation between the optical density and the probe detuning as shown in figure 3.6. Therefore, the scaled column density is given by

$$n(x,y) = \frac{OD}{\sigma_0 f(\omega)}. \tag{3.13}$$

3.3.2 NI Labview measurement control for MOT

In this work, the MOT variables values and time sequence were controlled by a NI-6009 data acquisition module (DAQ) which was programmed in Labview. The graphical user interface (GUI) used to control the MOT is shown in figure 3.7. The following MOT parameters can be set or customised on the GUI control panel column: 1) MOT loading time, 2) magnetic field gradient, 3) MOT expansion time or time of flight (TOF), 4) cooling beam detuning and 5) probe beam detuning. After imaging, the MOT optical density (OD) image is shown on the panel.

In a single measurement run, there are two primary values which are extracted from an OD image: the MOT cloud width and the atom number. The MOT cloud width and position of the cloud centre were extracted by fitting the image with a 2D Gaussian function. The atom number can be obtained as explained in section 3.3.1.2. Other quantities, such as the cloud volume and temperature can be obtained by multi-measurement runs. Therefore, the program was designed to run multiple measurements.

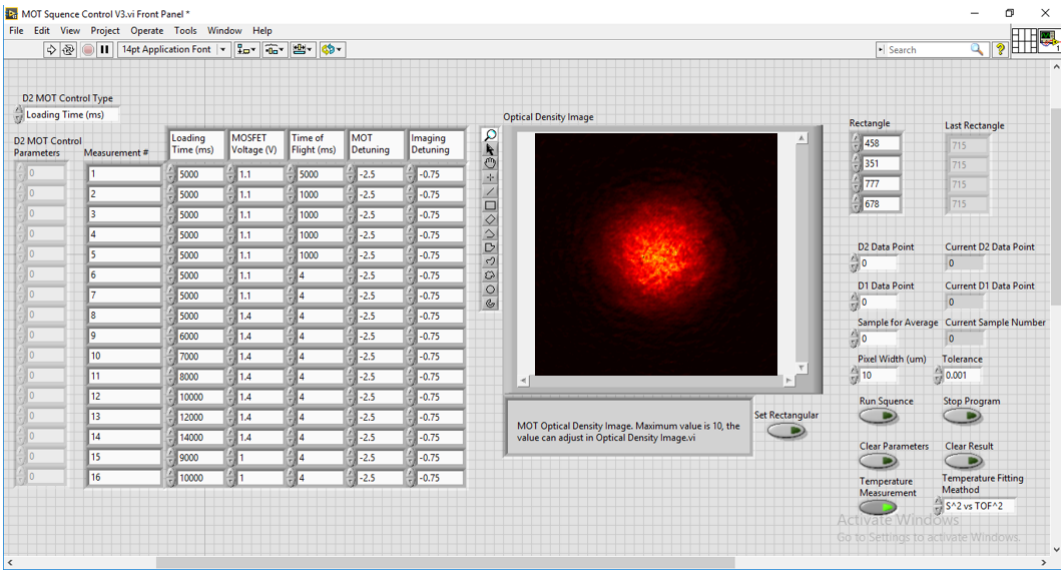

Figure 3.7: Labview console for experimental control and data acquisition.

DAQ Ch.	Device	Parameters	Time Sequences
DO_2	MS	Cooling Intensity	
AO_1	Double-Pass AOM	Cooling Detuning	
DO_2	MS	Repump Intensity	
AO_0	MOSFET	Magnetic Field	
DO_0	AOM2	Imaging Intesity	
DO_4	PCO Pixelfly	Camera Trigger	
		Time(ms)	Loading TOF dt MOT Rest dt Light Dark Rest

Figure 3.8: Timing sequence for MOT and imaging.

The time sequence of a MOT measurement is presented in figure 3.8. During the first phase, the MOT is loading with the MOT beams mechanical shutter open and the anti-Helmholtz coils current on. The cooling frequency was red detuned by the double pass AOM. The MOT was loaded for a given time then the MOT beams and the coils current were switched off simultaneously at the beginning of time of flight phase. In this phase, the MOT cloud was allowed to expand. In preparation of the TOF phase, the double pass AOM frequency is decreased to the value required for the imaging probe. In the imaging phase, the probe beam illuminated the expanding MOT cloud. Then, the camera shutter was triggered to expose the CCD array to the transmitted probe beam for a given exposure time (10-100 μs), and the MOT image was obtained. After that, the probe beam was switched off and a waiting time was introduced in the sequence to ensure that the MOT cloud vanished before taking the light image which is simply an image of the probe beam profile.

Ideally, there is no delay between switching on the probe and triggering the camera. However, we introduce a 1 ms delay time td of the camera trigger to compensate for the finite response time of the imaging AOM. Finally, the background or dark image was taken. After the imaging phase, the double pass AOM frequency was returned to the value required for the MOT in preparation for next sequence.

3.4 Characterization of the ^{133}Cs MOT

In this section, the MOT is characterised and optimised in terms of temperature, loading, R and loss rate, $\frac{1}{\tau}$ which were characterised as a function of quadrupole magnetic field gradient and MOT cooling beams detuning. The purpose is to obtain the optimum conditions for the experiments with radioactive atoms.

The characterisation was conducted via absorption imaging. The controlled operating MOT parameters are the following: the MOT beams diameter is 2 cm, the cooling and repumping beam power is 10 and 2 mW/beam respectively. The MOT atom number was measured for different loading times. Then, the loading curves were fitted with equation 1.18 to find R, $\frac{1}{\tau}$ and the MOT atom number at equilibrium (N_{sat}).

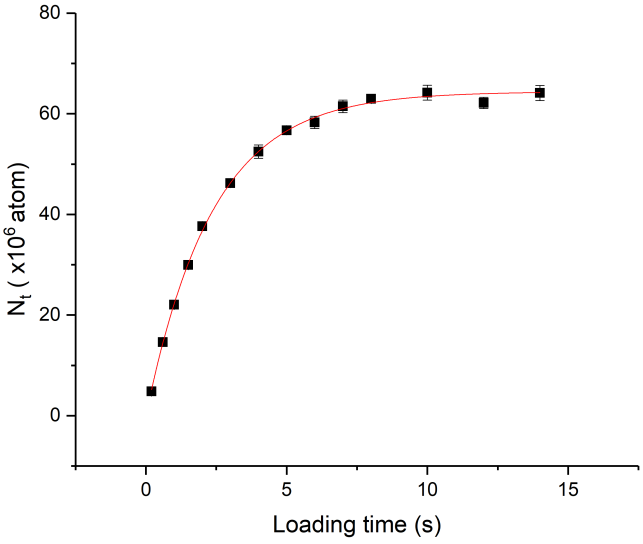

Figure 3.9: A MOT loading curve with parameters: $\delta = -2.5\Gamma$, $\frac{dB}{dz} = 14$ G/cm. The fit of the data with equation 1.18 gives the following results: 1) loading rate, 27.2 ± 0.6 million atom/second. 2) total effective loss coefficient, $\frac{1}{\tau} = 0.42 \pm 0.01$ s^{-1}. Reduced chi-square of the fit, $\chi^2_{red} = 0.941$.

Figure 3.9 shows a typical MOT loading curve. The atom number increases drastically in the early loading period (0 to 2 s) because of imbalance of MOT loading and loss rate. Then, the population saturates because the loss rate increases as well. Finally, the trap number reaches the saturation level of 64.4 ± 0.5 million atoms, which corresponds to the balance between MOT loading and loss rate.

3.4.1 MOT loading rate

Figure 3.10 illustrates the influence of the cooling laser detuning on the MOT loading rate which is increased by increasing the amplitude of the negative detuning until the rate reaches a maximum point and then start to decline. The observed trend of the MOT loading rate can be understood considering the MOT trapping force (equation 1.12 and 1.13) and the MOT capture velocity, v_c given that $R \propto {v_c}^4$. For a fixed magnetic field gradient, an increase of the MOT capture velocity requires an increment of the MOT detuning corresponding to the larger Doppler shift. However, if the detuning is too far from the resonance frequency, only atoms at the edge of the trapping region are slowed down, which is not enough to slow the atoms

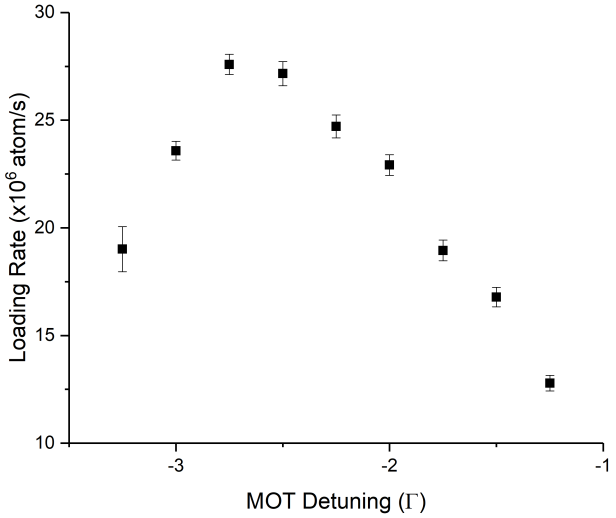

Figure 3.10: MOT loading rate as a function of the detuning of the MOT cooling beams.

down to rest. Therefore, there is an optimum detuning that leads to maximum capture velocity and loading rate. In this case, the maximum loading rate of 27.5 ± 0.5 million atom/second was achieved at $\delta = -2.65\Gamma$.

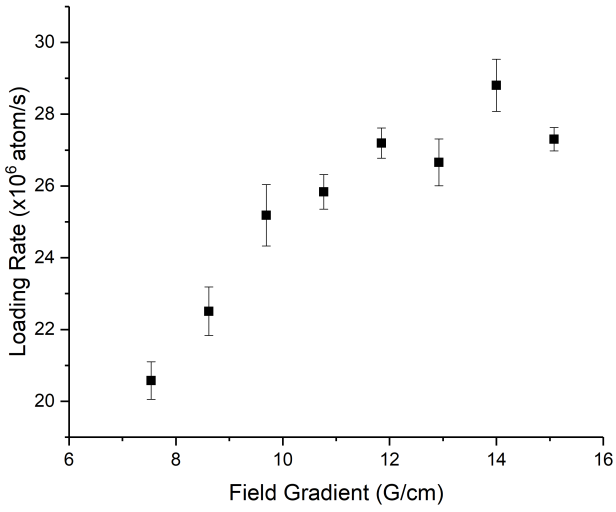

Figure 3.11: MOT loading rates as a function of magnetic field gradient.

The MOT magnetic field gradient provides a similar effect on the loading rate. By increasing the magnetic field gradient, the trapping force is strengthened because the Zeeman shift is larger and matches the Doppler shift of fast atoms resulting in

high capture velocity. Figure 3.11 shows the effect of magnetic field gradient on the MOT loading rate, the loading increases for increasing field gradient and reaches a maximum level of 28.8 ± 0.7 million atom/sec at 14 G/cm. However, the loading rate decreases after the maximum because as the detuning was kept constant, an increase of the magnetic field gradient leads to a decrease in the trap region area. This means that an atom has less time to decelerate in the trap.

3.4.2 MOT total loss coefficients

Losses of atoms in the MOT are caused by two mechanisms, namely background and intra-trap collision. In order to identify the working point that provides the minimum loss, the dependence of the total loss coefficient on the detuning and magnetic field gradient was observed.

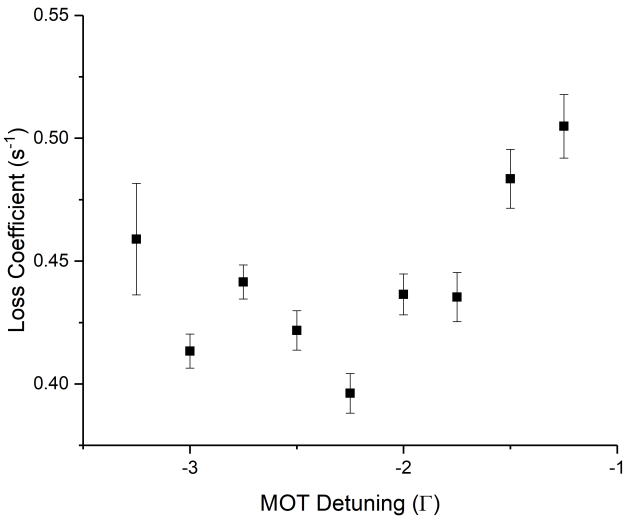

Figure 3.12: Effective trap loss coefficient as a function of the detuning of the MOT cooling beams.

In figure 3.12, the total loss coefficient is plotted as a function of the detuning of the MOT cooling beams. The measured loss rate was 0.51 ± 0.01 s^{-1} at -1.25Γ detuning. The loss rate then decreases for increasing detuning until it reaches the minimum of 0.39 ± 0.01 s^{-1} at -2.25Γ detuning.

Figure 3.13 shows the linear relation between magnetic field gradient and the total loss coefficient. An increase in magnetic field gradient increases the trap con-

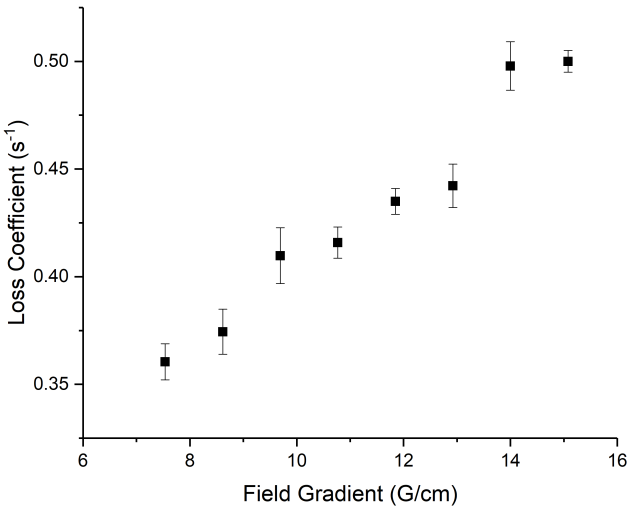

Figure 3.13: Effective trap loss coefficients as a function of the magnetic field gradient.

finement resulting in an increase of MOT peak density as well as in the total loss coefficient. This result agrees with the theoretical model in [43] which considers a two body collision loss rate proportional to the trap magnetic field gradient.

The MOT from ion implantation will operate with an ultra-low trapped atom number, in the range of few thousand atoms. In this regime, intra-trap collisions are negligible and the loading rate is the key factor. Therefore, the values of MOT detuning and magnetic field gradient leading to the best loading rate are selected.

3.4.3 MOT temperature

The temperature of the MOT is an important parameter which has to be minimised before progress to subsequent cooling stages. The lower bound of the MOT temperature corresponds to a sub-Doppler temperature [37], given by

$$k_B T = \frac{\hbar \Gamma I}{2 k_B I_0 |\Delta|} \left(C_1 + C_2 \frac{1}{1+4\Delta^2} \right), \tag{3.14}$$

where Δ is laser detuning in unit of natural linewidth, Γ. C_1 and C_2 are fit parameters. The sub-Doppler temperature of a MOT is the result of polarisation gradient cooling [37][39].

The effect of cooling beam detuning on the MOT temperature is shown in fig-

ure 3.14. The MOT temperature in the x and y directions increase for decreasing detuning amplitude. This can be explained by a decrease in the efficiency of polarisation gradient cooling because slow atoms near trap centre strongly interact with the low-detuned laser field. This leads to an increase in the atomic velocity.

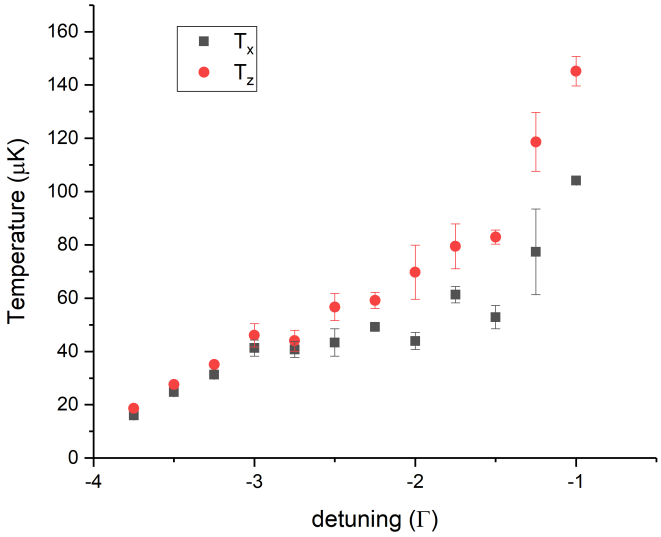

Figure 3.14: MOT temperature as a function of MOT cooling beam detuning.

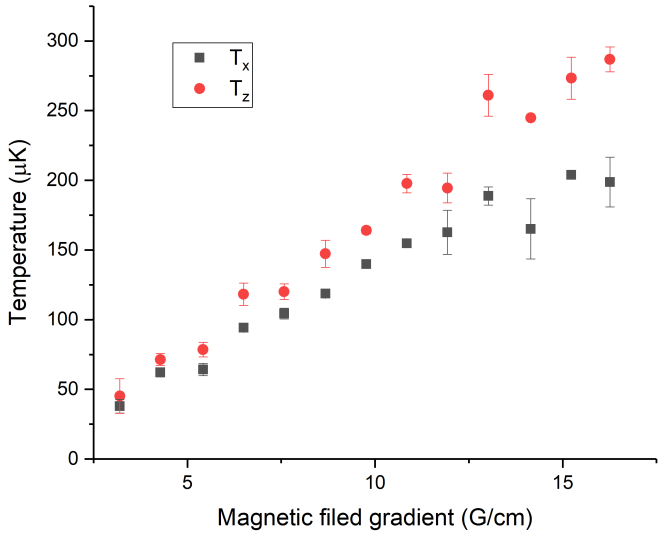

Figure 3.15: MOT temperature as a function of magnetic field gradient.

Increasing the magnetic field gradient heats up the trapped atoms as shown in figure 3.15. The MOT density is increased due to increase of magnetic field gradient. Consequently, multiple scattering is induced resulting in the increase of cloud temperature. Moreover, polarisation gradient cooling is less effective and Doppler cooling becomes dominant.

Chapter 4

MOT of ^{133}Cs atoms from ion implantation

The next phase of the experiment consisted in trapping ^{133}Cs atoms, provided by an ion beam generated from a surface ionisation source [73]. The focused ion beam enters the cold atom setup through the small hole of vacuum impedance and is implanted and neutralised in a 25 mm thick foil. The foil is chosen to be yttrium due to a favourable imbalance between ionisation energy and work function. Then, neutralised atoms were extracted by resistive heating. After that, MOT loading from the neutraliser was performed [33]. The implantation profile was numerically simulated, and a phenomenological model for the neutraliser was also developed. A model of 1D diffusion was used to extract the neutraliser activation energy.

In addition, preliminary implantation tests were also performed with radioactive beams, in this case for the production of ^{135m}Cs. $^{135m}Cs^{+}$ was generated by means of proton induced fission in a Uranium target. The ions were extracted and accelerated through a mass separator which directed the $^{135m}Cs^{+}$ beam to be implanted in a neutraliser. After implantation, gamma emission from the neutraliser was detected by a gamma detector. Then, by using the gamma spectrum, half-life of ^{135m}Cs was measured in order to verify implantation of the species. Moreover, preliminary tests for trapping of ^{135}Cs were also conducted.

4.1 Ion beams of Caesium isotopes and isomers

In IGISOL facility, the ion beam for the ion implantation was generated from two sources, the K-130 cyclotron beam accelerator (the 'online source') and a surface ionisation source (the 'offline source'). The IGISOL facility is shown in figure 4.1.

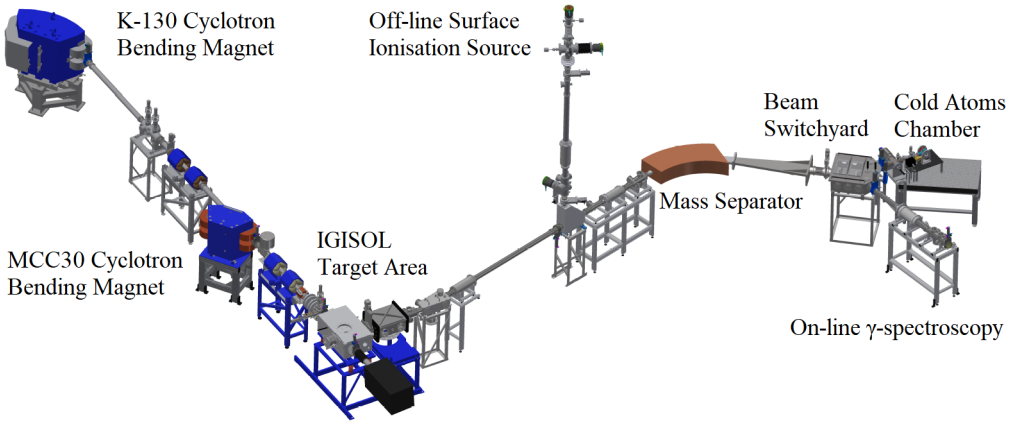

Figure 4.1: Sketch of the IGISOL facility. The facility produced ion beams for the experiment using two different sources. 1) The online source generated an ion beam of caesium by mean of the proton-induced fission reaction. The K-130 cyclotron accelerator generated a proton beam that bombards the natural uranium target at the IGISOL target area to induce a fission reaction. The reaction product, which was ions were accelerated to the mass separator. 2) The offline source is a surface ionisation source where caesium atoms on a cylindrical rod surface were ionised by resistive heating. Then, a skimmer electrode accelerated the ions to the mass separator. The ions beam of selected isotopes was magnetically directed to the beam switchyard. The ion beams direction could be electronically switched to the cold atoms experiment or online γ-spectroscopy area. The cold atom experiment is attached on the right side of the facility. The optical setup and alignment of the experiment is not included in this figure. This figure is derived from [33].

4.1.1 Online source

The online source was used to produce radioactive ion beams for our experiment. A 50 MeV proton beam was generated from the K-130 cyclotron beam accelerator and hit a natural uranium target located in the IGISOL target area in order to induce fission reaction. The fission products dispersed from the target into helium buffer gas for thermalisation [74]. Then, the products - mostly single charged ions - were 30 keV accelerated through a sextupole ion guide (SPIG) [75]. The ion beam was guided to a mass separator which has a 55 degree dipole magnetic field,

corresponding to $300 < \frac{M}{\Delta M} < 500$ of mass resolving power. The resolving power specifically allows $^{135m}Cs^{+}$ and other $\frac{A}{q} = 135$ fission products into the ultra-high vacuum science chamber of the cold atom experiments. The laser cooling and trapping apparatus was designed to trap only caesium isotopes and isomers, therefore non-caesium products will not be trapped.

4.1.2 Offline source

A surface ionisation source [73] is used as a source of stable $^{133}Cs^{+}$. In the source, alkali atoms - in this work caesium atoms - are pasted on a cylindrical rod and a skimmer electrode. The rod is resistively heated to 1000-1200 K to generate a caesium plasma. Then, the caesium ions are extracted by the electrode. The $^{133}Cs^{+}$ ions were accelerated by a 30 kV electrode to the mass separator and transferred to the experimental chamber by the same process applied to the online ion beam. The use of an offline source was more convenient than an online source because this allowed us to operate with large quantities ion beam. However, the offline source has limited ion species, it can only produces an ion beam of stable isotopes available in macroscopic quantities. The offline source was used to develop and optimise cold atom experiment prior to online runs.

4.2 Cold atom experiment setup

4.2.1 Vacuum system for the ion beam MOT

A single chamber MOT vacuum system was used for the experiment as shown in figure 4.2. In preparation for the MOT loading from ion implantation, all processes in this experiment were performed under ultra-high vacuum (10^{-9} mbar) in a borosilicate glass cell with the neutraliser (described in section 4.2.2) embedded at the end of the ion beam line. The inner surfaces of the glass cell were anti-relaxation organic coated, as detailed in section 4.2.3. The glass cell shape is spherical with six 40-20 scratch-dig optical windows. A window pair was aligned with the anti-Helmholtz coils main axis which is parallel to optical table level, in order to allow positioning the coils near the cell. The Y foil was installed 28 mm from the cell centre. The dimensions of the glass cell are shown in figure 4.3.

A vacuum impedance was installed to separate the ion beam part from the cold atom experiment part. Vacuum pressure in the ion beam part was maintained by a 350 l/s turbo-molecular pump (Leybold CE TURBOVAC 350i) at a pressure less than 10^{-8} mbar. The pressure of the cold atom experiment part was maintained at 10^{-9} mbar by an ion pump (Varian Valcon Plus 20 StarCell, 20 l/s speed).

The ion pump was protected by a gate valve which was placed to separate the ion pump and the rest of the experiment part. This isolated the ion pump from high pressure during the pre-evacuation and baking process. The gate valve and the glass cell were connected with a 4 ways CF40 cross. Moreover, the CF16 valve and nipple tube containing 1 g of pure ^{133}Cs which was used in chapter 3 as a ^{133}Cs reservoir was also connected to the cross. The reservoir provides ^{133}Cs useful for MOT alignment and optimisation.

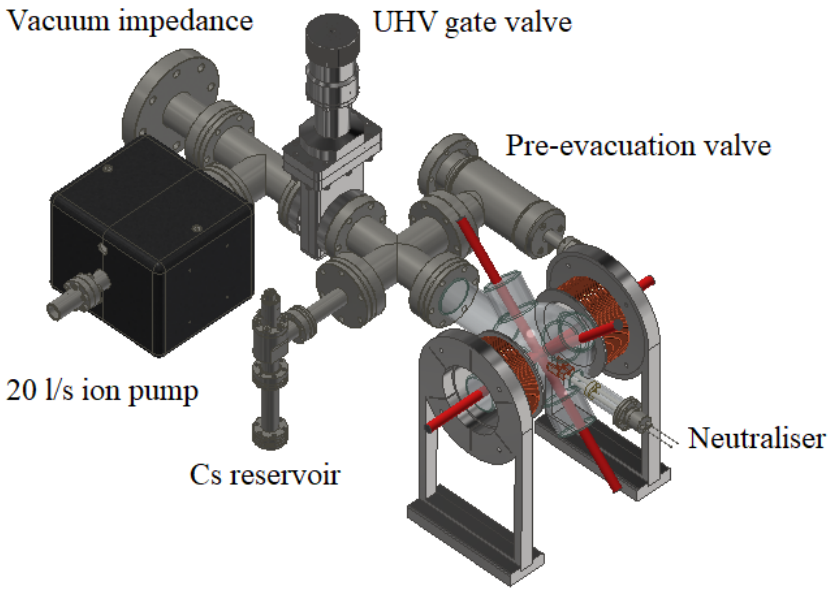

Figure 4.2: Vacuum system for the production of ^{133}Cs MOT from ion implantation. The MOT in the glass cell is loaded from background Cs supplied by two different sources, the liquid caesium reservoir and the neutraliser. A caesium ion beam entered the experiment through a 1.5 mm vacuum impedance hole and impinged in the neutraliser. A UHV gate valve separated the experiment and the ion beam facility. A 20 l/s ion pump maintained the ultra-high vacuum (UHV) pressure. A picture of the vacuum system for the ion implanted MOT and optical setup are shown in figure D.9, appendix D.

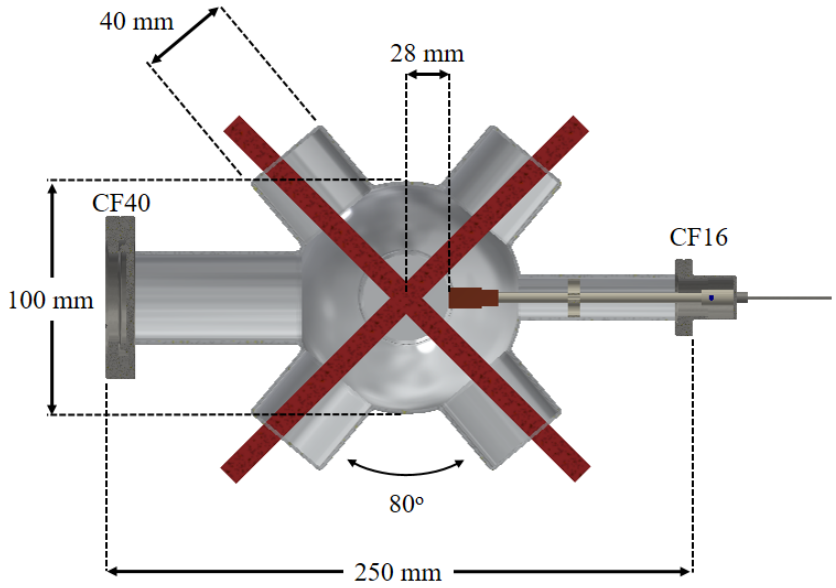

Figure 4.3: Cross-section of the catcher foil installed in the glass cell. A picture of the glass cell used in this experiment is shown in figure D.10, appendix D.

4.2.2 Ion implantation in a neutraliser

The neutraliser is an important part for this experiment. It is a thin metallic foil where ions provided by the ion beam are accumulated and neutralised. The release of neutralised atoms was achieved by resistive heating of the neutraliser.

The neutraliser is a 16×9 mm^2, 25 μm thick yttrium foil held by copper supports as shown in figure 4.4. The support was connected to a CF16 electrical feedthrough via two 1.5 mm copper wires. The wires were insulated by hollow Aluminium oxide (Al_2O_3) rods which secured current up to 20 A. The rods and the support separation were fixed by a ϕ = 16.5 mm, MACOR center ring in order to prevent excessive stress in the catcher foil.

The $^{133}Cs^+$ beam was electrostatically focused and impinged on the neutraliser as shown in figure 4.3. The high energy ions from the ion beam penetrated into the Y foil surface and were slowed down to the diffusive regime by inelastic collisions with the Y lattice, until they are stopped inside the foil. The ions were neutralised by the acquisition of a surrounding electron. The neutralisation was achieved because the caesium ionisation potential ($I_{Cs} = 3.89$ eV) is higher than yttrium work function

($W_Y = 3.1$ eV). Efficiency of the ion implantation is given by the Langmuir-Saha equation [76],

$$\frac{n_+}{n_a} = \frac{g_+}{g_a} \exp\left(\frac{W_Y - I_{Cs}}{k_B T}\right) , \tag{4.1}$$

where $\frac{g_+}{g_a} = \frac{1}{2}$ for alkali atoms, T is Y foil's temperature, n_+ and n_a are the concentration of ions and neutral atoms in the material, respectively. From equation 4.1, $\frac{n_+}{n_a} \leq 10^{-4}$ for a neutraliser temperature of $T = 298$ K.

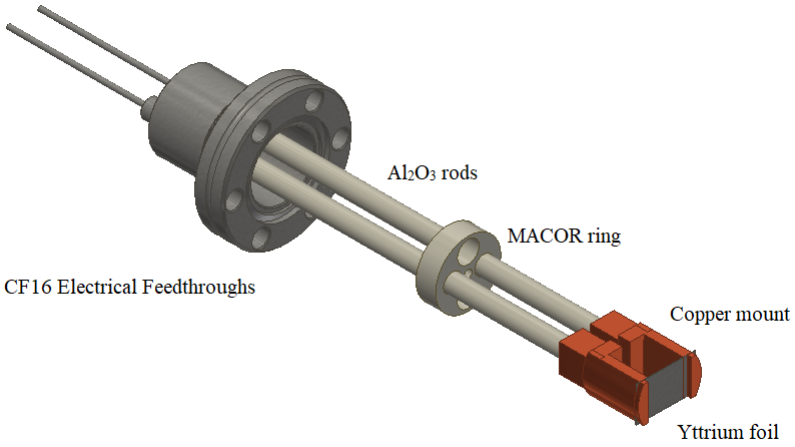

Figure 4.4: Design of the Yttrium neutraliser. A yttrium catcher foil (a rectangular grey sheet) was clamped between two copper mounts. Two copper wires insulated by hollow Aluminium oxide (Al_2O_3) rods connected the mounts and the CF16 electrical feedthrough. A machinable glass-ceramic MOCOR ring separated the rods to prevent excessive stress in the catcher foil. The design is derived from [33]. A picture of the neutraliser used in this experiment is shown in figure D.11, appendix D.

The initial concentration distribution of implanted atoms, $n_0(x)$ in the neutraliser contributes to the time-dependent behaviour of the atomic distribution which is discussed in section 4.3. $n_0(x)$ is characterised by a phenomenological function, which was first introduced by T. Warner, et al. [77] given by,

$$n_0(x) = \frac{2N_0}{\xi}\Gamma\left(\frac{n+1}{2}\right)^{-1}\left(\frac{x}{\xi}\right)^n \exp\left(-\frac{x^2}{\xi^2}\right) , \tag{4.2}$$

where N_0 is the implanted atom number and the length scale ξ is related to the mean

implantation depth, d, as given by

$$\xi = \Gamma\left(\frac{n+1}{2}\right)\Gamma\left(\frac{n+2}{2}\right)^{-1} d. \tag{4.3}$$

The width of the distribution is characterised by n. The dependence of the implantation distribution on n is shown in figure 4.5.

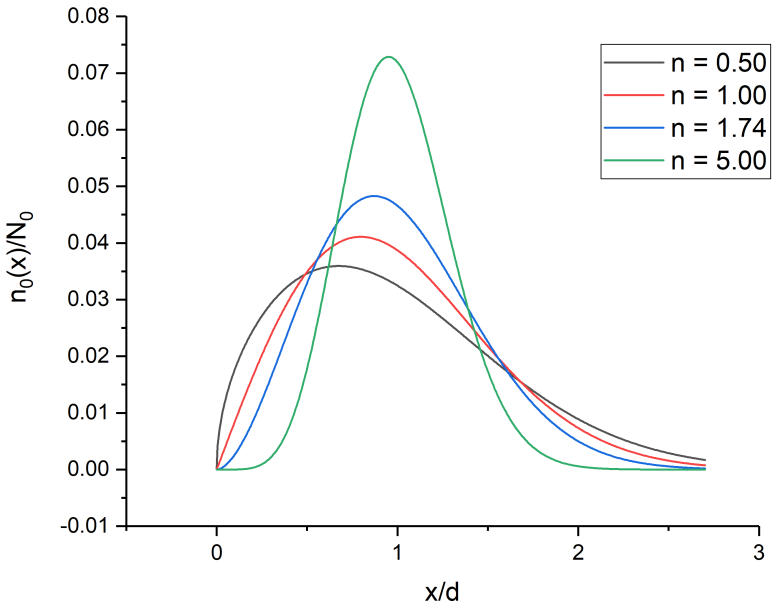

Figure 4.5: Initial distribution of implanted atoms with different characteristic number, n.

In this work, the initial implanted atomic concentration distribution is calculated with the help of the SRIM (Stopping and Range of Ions in Matter) code [78]. The distribution is fitted with equation 4.2 to find the corresponding value of n as shown in figure 4.6. The fit results indicate a mean implantation depth, $d = 18.5 \pm 0.1$ nm and $n = 1.74 \pm 0.06$.

The implanted ^{133}Cs atoms were extracted by resistive heating enhanced thermal diffusion. A DC electric current, I was applied through the electrical feedthrough. The foil temperature was measured by a pyrometer. In this experiment, the maximum applied current used is 6.5 A corresponding to a foil temperature of 1010 K. The maximum temperature is well below the Y foil melting point

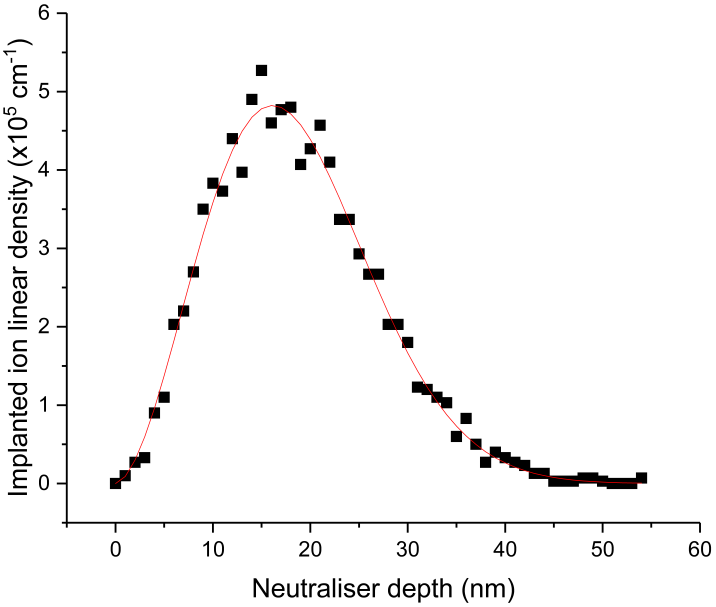

Figure 4.6: SRIM simulation of the initial distribution of 10^4 30 keV $^{133+}$Cs implanted into a 25 μm thick, Y - neutraliser simulated by SRIM. The simulation was done by Dr. Sami Rinta-Antila. The fit of the data (red curve) with the phenomenological function (equation 4.2) provides $d = 18.5 \pm 0.1$ nm and $n = 1.74 \pm 0.06$. Adjusted R-square of the fit, $R^2_{adj} = 0.988$.

temperature of 1800 K.

4.2.3 Adsorption on glass cell surface and anti-relaxation coating

MOT loading using the ion implantation technique yields a lower number of trapped atoms compared to a stable vapour produced by solid reservoirs or dispensers. This is because the release rate and the number of implanted atoms from the heated neutraliser is comparatively low. In the case of short lived species, the decay rate also represents a loss resulting in a low number of atoms trapped in the MOT. Additionally, due to the resistive heating process, the atomic release temperature is too high to allow for direct capture in the MOT.

The hot atoms can be thermalised by bouncing off the cell wall resulting in a decrease of their kinetic energy to a level suitable for their capture in the MOT. However, with a bare glass or steel surface, there is a high possibility that atoms in

the vapour phase are lost to the cell wall either permanently or temporarily because of chemisorption and physisorption, respectively [79][80]. These can reduce the number of trap atoms.

The "chemisorption" refers to the adsorption of the atoms to the surface by covalent bond or Coulomb forces. The chemisorbed atom will stick to the surface permanently because the interaction is strong. At the opposite regime, because atoms bond to the surface by weak van der Waals forces, atoms that adsorb to the surface by physisorption have the possibility to escape from the surface to the vapour phase. This process is characterised by the average time interval that atoms stick to the surface called "sticking time" [79][80],

$$\tau_s = \tau_0 \exp\left(-\frac{E_{ads}}{k_B T}\right), \tag{4.4}$$

where $\tau_0 \sim 10^{-12}$ s is the sticking time for pure elastic collision. E_{ads} is the adsorption energy of an atom to the surface and T is the surface temperature.

The time-dependent population of untrapped atoms in the glass cell, $N_{bg}(t)$ is described by [79][81],

$$N_{bg}(t) = (N_0 - N_{mot}(t)) \frac{\exp\left(-\frac{trA}{V}\right)}{1 + (\tau_s v_{th} A/4V)}, \tag{4.5}$$

where A and V is the surface area and volume of the glass cell. N_0 is total initial atoms in the glass cell. N_{mot} is MOT atoms number and r is effective pumping speed of the surface due to chemisorption.

To improve trapped atom number, the glass cell's inner wall was coated with polydimethylsiloxane (PDMS). PDMS chemical formula is $CH_3[Si(CH_3)_2O]_nSi(CH_3)_3$, where n is the number of repeating monomer units [80]. PDMS has important properties that suit for this work which are low cost, simple fabrication, optical transparency and non-flammable [82][83][84].

The PDMS coating reduces atoms permanent loss from chemisorption on glass cell surface and reduce the sticking time because the coated surface lowers the desorption energy, E_{ads} to $\sim$0.1 eV. The coating process applied for this experiment is

based on [85] and was performed by Dr. Luca Marmugi.

4.2.4 Fluorescence imaging

Fluorescence imaging is used as a non-destructive measurement and a proper tool for active monitoring MOT's atom number dynamic during the MOT loading.

The fluorescence imaging system was installed above a MOT Pyrex science chamber. The system is comprised of 1) a 16.8 mm diameter pinhole, it was placed 72 mm away from the MOT cloud in order to reduce background photon. 2) an 852 nm interference filter with 10 nm bandwidth and 3) a digital 14 bit CCD camera (PCO.Pixelfly USB) with objective lens (PENTAX C2514-5M).

4.2.4.1 MOT atom number measurement

The spontaneous photons from MOT cloud are partially capture by the imaging system and go to CCD array of a CCD camera where count signal is generated. The amplitude of the signal relates to the number of the incoming photon that hit the CCD array. Therefore, MOT atom number, N_{atom} proportionally relate to the count generated by CCD camera, N_c [86]. The relation is

$$N_{atom} = \frac{4\pi}{\eta T_c \Omega R_{sc} t_{exp}} N_c, \tag{4.6}$$

where T_c is the transmission coefficient of optical imaging alignment. Ω is solid angle captured by the pinhole aperture. R_{sc} is the scattering rate (equation 1.7 and 1.8). t_{exp} is an exposure time of the camera. η is the quantum efficiency of the CCD camera, it is ratio of CCD count to number of CCD array's input photon number.

4.2.4.2 Camera's quantum efficiency measurement

The quantum efficiency of the camera, η is an essential constant for fluorescence imaging. Although, there is a specific value of η which was mentioned in camera datasheet, on-site measurement of η is still necessary.

To measured η, CCD array of the PCO Pixelfly USB had been exposed to a calibration beam (a filtered 852 nm laser beam) for given exposure time, t_{exp}. Then, the CCD array generated count signal, N_c which related to t_{exp}. Therefore, the η

can be calculated and given by,

$$\eta = \frac{\hbar\omega}{I_c}\frac{\mathrm{d}N_c}{\mathrm{d}t_{exp}}, \tag{4.7}$$

where $I_c = 16.8\ \mu$W is the calibration beam power and $\omega = 2\pi \times 351.726$ THz is an angular frequency of the beam. $\frac{\mathrm{d}N_{count}}{\mathrm{d}t_{exp}} = 2.55 \times 10^8$ count/s is a linear fitted slope of N_c - t_{exp} plot. The measured quantum efficiency of the CCD camera, $\eta = 0.354$.

4.3 Implantation and extraction in the neutraliser: 1D diffusion model

Dynamics of implanted atoms in the neutraliser was mainly explained by thermal diffusion in material which is governed by Fick's laws [87],

$$F = -D\frac{\partial n}{\partial x}\,, \tag{4.8}$$

where F is atomic flux in material, n is implanted atom concentration in a neutraliser and D is the diffusion coefficient which explained by Arrhenius equation [88],

$$D = D_\infty \exp\left(-\frac{E_a}{k_B T}\right), \tag{4.9}$$

where D_∞ is diffusion coefficient for high neutraliser temperature, $T \gg 1000$ K, which difficult to quantify. D can be calculated using reference diffusion coefficient, D_{ref} at curtain temperature, T_{ref}. Therefore, equation 4.9 become

$$D = D_{ref} \exp\left[\frac{E_a}{k_B}\left(\frac{1}{T_{ref}} - \frac{1}{T}\right)\right]. \tag{4.10}$$

Under the condition that D is independent of time, position and atom concentration in material [87], the 1D diffusion equation can be derived by applying equation 4.8 to the continuity equation for mass given by,

$$\frac{\partial \phi}{\partial t} + \nabla \cdot F = 0\,. \tag{4.11}$$

The solution of equation 4.11 becomes the 1D diffusion equation,

$$\frac{\partial n}{\partial t} = D\frac{\partial^2 n}{\partial x^2} - \lambda n \,, \tag{4.12}$$

where λ is decay rate of the implanted species.

In a semi-infinite piece of material and $\lambda \sim 0$, the solution for equation 4.12 is obtained by method of Green's function of the diffusion equation [89] and initial distribution of implanted atoms in material, $n_0(x)$. The result is time-dependent distribution function [90]],

$$n(x,t) = \frac{1}{2\sqrt{\pi D t}} \int_0^\infty n_0(x') \left(\exp(-\frac{-(x-x')^2}{4Dt}) - \exp(-\frac{-(x+x')^2}{4Dt}) \right) \mathrm{d}x' \,. \tag{4.13}$$

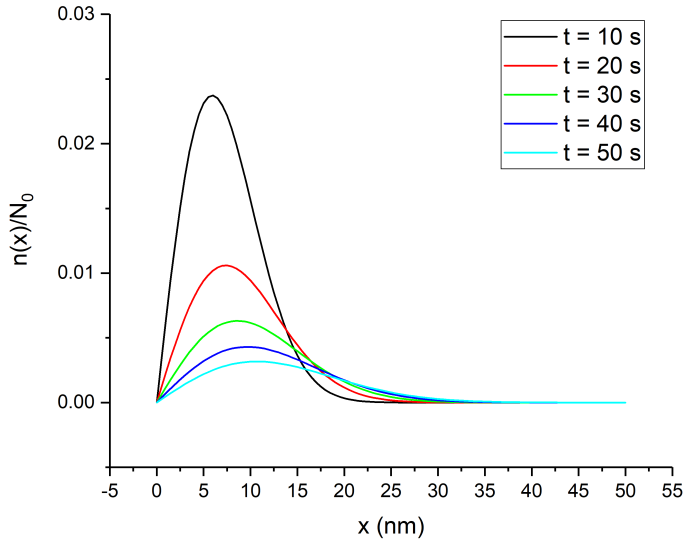

Figure 4.7: Time evolution of implanted atom distribution is simulated from following parameter: $D = 1.0$ nm^{2}s^{-1}, N_0 = 1, $d = 5$nm and n = 1.74.

Time evolution of normalised implantation distributions in equation 4.13, using the value $n_0(x)$ from equation 4.2 are shown in figure 4.7. The figure demonstrates the implanted atoms dissipation over the diffusion time under the condition that the atoms concentration at the neutraliser surface is zero.

The peak of the distribution, which was related to mean implantation depth, d,

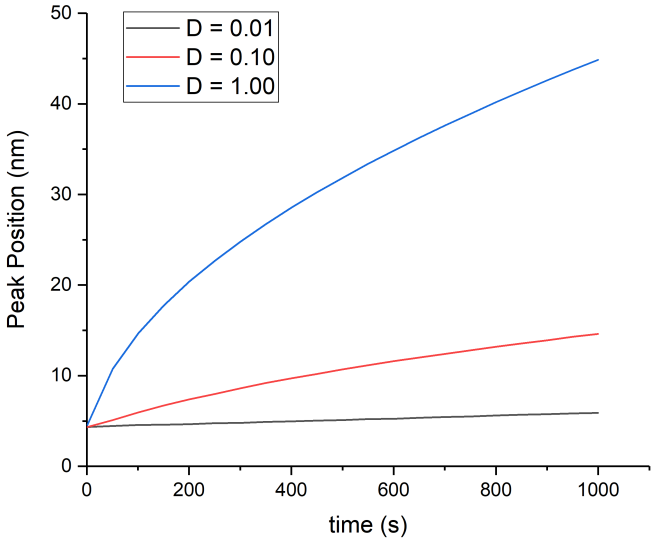

Figure 4.8: Distribution peak position as function of diffusion time. The diffusion coefficient value 1.0, 0.1 and 0.01 nm^2s^{-1} correspond to temperature of 1000, 830 and 710 K respectively.

is time-dependently shifted inside foil material. The peak shifting rate depends on the temperature dependent diffusion coefficient, D shown in figure 4.8. Although, the peak shift inside, the number of implanted atoms, $N = \int_0^\infty n(x)\mathrm{d}x'$, in the material is reduced over diffusion time. This indicate releasing of the implanted atoms from the nearest surface of the neutraliser.

4.4 Release rate of the neutraliser

The foil release rate caused by thermal diffusion can be determined based on the regime of ion implantation. This can be divided into two regimes called the pulse and continuous regimes [88]. These are defined by the neutraliser temperature during ion implantation and the timing of resistive heating.

4.4.1 Pulsed regime release rate

The pulse regime can be achieved by implanting ions into a low temperature neutraliser for curtain implantation time, t_{imp}. At low temperature, the diffusion coefficient is low, therefore, thermal diffusion can be neglected. In pulse regime, by taking the efficiency of the ion implantation in equation 4.1 into account, the im-

planted atom number is

$$N_0 = I_0 \times t_{imp} \ , \tag{4.14}$$

where I_0 is the ion beam current in unit of ions/s. Once the ion implantation is completed, neutraliser resistive heating is applied to a given temperature.

In pulse regime, the neutraliser release rate due to thermal diffusion, F_p is obtained by substituting equation 4.13 into 4.8. The atom release rate of the neutraliser is defined as the atomic flux at surface of the neutraliser ($x = 0$)

$$F_p(t) = \frac{1}{2\sqrt{\pi D t^3}} \int_0^\infty n_0(x') x' \exp\left(\frac{-x'^2}{4Dt}\right) \mathrm{d}x' \ . \tag{4.15}$$

From equation 4.15 and 4.2, the mathematical model of a neutraliser's release rate becomes

$$F_p(t) = \frac{N_0}{t_d\sqrt{\pi}} \Gamma\left(\frac{n+1}{2}\right)^{-1} \Gamma\left(\frac{n+2}{2}, 0\right) \left(\frac{t}{t_d}\right)^{\frac{n-1}{2}} \left(1+\frac{t}{t_d}\right)^{\frac{-(n+2)}{2}} \ , \tag{4.16}$$

where t_d is the characteristic diffusion time given by

$$t_d = \frac{d^2}{4D} \ . \tag{4.17}$$

In the case that the ion beam current was very low, it requires a long implantation time to accumulate sufficient implanted atoms before the resistive heating. This is not efficient with short life-time species because a large amount of the atom will decay during implantation. To conclude, The pulse regime operation is useful for implantation of long life-time species with low ion beam current. Moreover MOT loading using pulse regime operation provides a higher signal to noise ratio of trapped number.

4.4.2 Continuous regime release rate

Continuous regime occurs when ion implantation and neutraliser resistive heating are operated simultaneously. The implantation rate at a given time, t is related to ion beam current, I_0. A fraction of the implanted atoms immediately diffuse to the

neutraliser surface and are desorbed. The release rate for the continuous regime was calculated by the time integral of equation 4.15 where the implantation atom, N_0 was replaced by the implantation rate or the ion beam current. The release rate is given by

$$\begin{aligned} F_c(t) &= \int_0^t I_0 \frac{F_0(t-t')}{N_0} \mathrm{d}t' \\ &= \frac{I_0}{2\sqrt{\pi D}} \int_0^t \int_0^\infty t^{-3/2} x' n_0(x') \exp\left(\frac{-(x')^2}{4Dt}\right) \mathrm{d}x' \mathrm{d}t \\ &= \frac{2I_0}{\sqrt{\pi}} \left[\frac{\Gamma\left(\frac{n+2}{2}, 0\right)}{(n+1)\Gamma\left(\frac{n+1}{2}\right)} \right] \left[\frac{t}{t_d}^{\frac{n+1}{2}} {}_2F_1\left(\frac{n+1}{2}, \frac{n+2}{2}; \frac{n+3}{2}; \frac{-t}{t_d}\right) \right]. \end{aligned} \tag{4.18}$$

where ${}_2F_1(a,b;c;x)$ is the Gauss hypergeometric function. The MOT loading via continuous regime implantation is effective for short life-time species as implanted atoms are immediately extracted from the catcher foil after implantation.

4.5 Characteristics of MOT loading from ion implantation

Thermal diffusion in the neutraliser was indirectly observed by MOT loading. For a MOT from ion implantation, the MOT centre in the vertical axis was shifted downward to allows the ion beam to be implanted in the neutraliser which was located on the opposite site. The optimisation of MOT beam alignment has been done until the number of MOT atoms reaches a maximum. The maximized MOT number refers to the lowest MOT loss generated by collision with the ion beam.

The MOT loading was operated in the pulsed and continuous regimes to study in following aspects and contributions:

Bulk atom in the neutraliser : caesium impurity due to previous implantations was observed at various heating temperatures.

Effect of implantation time : The effect of implantation time on the MOT atom number was also measured in pulse regime operation.

Effect of implantation temperature : The MOT atom number loaded by continuous regime operation was conducted in order to indirectly observe thermal diffusion in the catcher foil. The observation has been done in replicated conditions for the isomer MOT. Moreover, the loading curves were fitted with a theoretical model to extract the activation energy, E_a of Y foil.

The time-dependent MOT atom number in both regimes was described by coupled rate equations. The MOT parameters in the equations are mathematically estimated. The operating condition of MOT is shown in table 4.1.

Parameter	Value	Unit
Cooling detuning (δ)	-2.65	Γ
Repumping detuning	0	Γ
Cooling beam intensity (I)	4.67	mW/cm^2
Repumping beam intensity	1.10	mW/cm^2
Magnetic field gradient ($\frac{dB}{dz}$)	14	G/cm
$^{133+}$Cs beam Current (I)	10^{-10}	A

Table 4.1: MOT operating parameters for loading atom from catcher foil.

4.5.1 Coupled rate equation and parameters estimation

The ^{133}Cs background density is related to neutraliser release rate enhanced by the thermal diffusion. The MOT atom number, N_t and ^{133}Cs number in the background, N_{bg} are explained by the coupled rate equations given [88][91]by

$$\begin{aligned} \frac{\mathrm{d}N_{mot}}{\mathrm{d}t} &= LN_{bg} - \gamma N_{mot} - \lambda N_{mot} \\ \frac{\mathrm{d}N_{bg}}{\mathrm{d}t} &= -(L+W)N_{bg} + \gamma N_{mot} + f - \lambda N_{bg} \ , \end{aligned} \tag{4.19}$$

where the atom input rate, f is equivalent to the neutraliser release rate, F explained in section 4.3 and the trapped atom decay rate, λ is neglected for ^{133}Cs.

4.5.1.1 Loading coefficient

MOT Loading rate, R is proportional to the background atom of trapped species, N_v. The relation is given by $R = LN_v$, where L is the loading coefficient which

represents the capture probability of the MOT. L can be explained by

$$L = \frac{3}{16\sqrt{\pi}} \frac{{v_c}^4}{{v_{th}}^3} \frac{\omega^2}{{r_{cell}}^3} \ , \tag{4.20}$$

where ω is the Gaussian width of the MOT beams. r_{cell} is the glass cell radius. v_c is the MOT capture velocity. The thermal velocity, $v_{th} = \sqrt{\frac{8k_BT}{\pi m}} = 217$m/s, for ^{133}Cs.

A parameter that play an importance role on the L is capture velocity, v_c. By assuming, an atom located at the edge of MOT region (a distance which equal to MOT beam's radius from a MOT centre.) and is moving toward MOT centre, v_c is defined as the lowest initial velocity that allows the atom to reach the opposite end of trap region and moving back to the trap centre [39][92]. The MOT's capture velocity strongly depends on MOT beam intensity [93], detuning [39] and diameter [94]. The v_c can be calculated by numerical solving of equation 1.11.

In his experiment, $L = 9 \times 10^{-4}$ s^{-1} is estimated from following parameter: capture velocity, $v_c = 18.5$ m/s, MOT beam's Gaussian width, $\omega = 1$ cm, glass cell radius, $r_{cell} = 5$ cm, thermal velocity, $v_{th} = 217$ m/s.

4.5.1.2 System loss coefficient

The system loss coefficient, W is generated by the vacuum system and chemisorption to glass cell surface. Note that the loss is dominantly affected by the vacuum system because the chemisorption is minimized by the relaxation coating. The W is given by

$$W = \left(\frac{r_{aperture}}{r_{cell}} \right)^3 \frac{\bar{v}_T}{2l} \ , \tag{4.21}$$

where $r_{aperture}$ is the radius of glass cell aperture connected to vacuum pumping side, the r_{cell} is the cell radius and l is the connection tube length from the cell centre to the cell aperture. The estimated number of the system loss coefficient for this experiment is $W_{Cs} \approx 47s^{-1}$.

4.5.1.3 Collision loss coefficient

For the MOT loading from the neutraliser, only the background collision is considered. The two-body collision can be neglected because of low trapped atom number

and density. In order to determine the background collision coefficient, the MOT loading need to be performed in the following conditions: 1) the background gas is considered as the ideal gas, and 2) amount of caesium atoms in the vacuum chamber is very low comparing to non-caesium atoms' in the glass cell, this result in domination of caesium and non-caesium collision. Under the conditions, the background collision coefficient, γ explained in equation 1.15 becomes

$$\gamma = \frac{P\sigma_b \bar{v}_b}{k_B T} \ , \tag{4.22}$$

where P is pressure in the glass cell. The Cs-non Cs collision cross-section, $\sigma_b = 2 \times 10^{-13}$ cm^2. The thermal velocity of the background atoms is, $\bar{v}_b = 470$ m/s for cell temperature of 298 K. For a pressure P in mbar, the background collision loss is $\gamma \approx P(0.23 \times 10^9)$ s^{-1}.

4.5.2 Loading from previous implantations

In case of long lived species, the remaining old implanted atoms in the neutraliser can be considered as bulk atoms. The bulk atoms are accumulated deep in the material because of mean implantation depth shifting, explained in section 4.2.2. The bulk atoms distribution profile is approximated as a Gaussian function multiply with a linear term of $\frac{x}{d}$ explained in [90]. By applying the distribution profile to equation 4.15, then the time-independent release rate contributed by the bulk atoms, F_B is given by [88],

$$F_B = \frac{N_{B0}}{2\tau_d (1 + t/\tau_d)^{\frac{3}{2}}} \ , \tag{4.23}$$

where N_{B0} is bulk atoms initial number, and τ_d is the characteristic diffusion time explained in equation 4.17. For the bulk atoms, $t << td$, the release rate is approximately time-independent. By substituted equation 4.17 and 4.9 into equation 4.23, the F_B is temperature dependent. To investigate the impurity effect on the MOT atom number, the MOT loading was conducted with various non implanted foil temperatures.

The loading curve from bulk atoms is shown in figure 4.9. The MOT loading curves then are numerically fitted with equation 4.19 to extract the release rate of

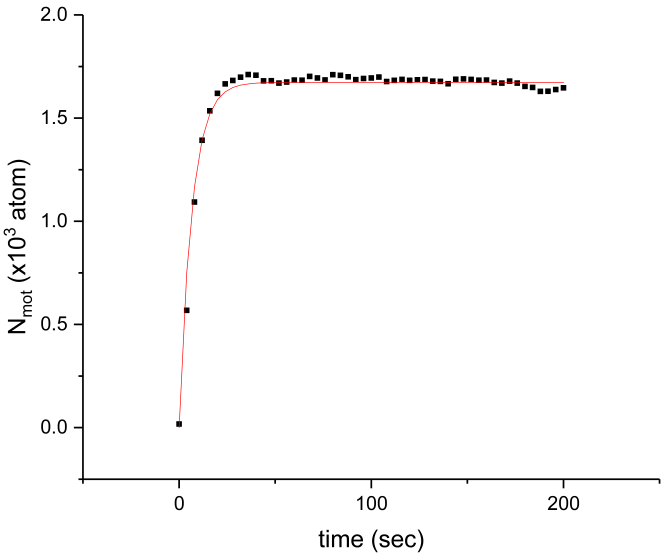

Figure 4.9: MOT atom population (black square) and fitting curve (red line) from equation 4.19 at operating temperature of 930 K. The fit result is a release rate, $F_B = 39.33 \pm 0.09$ million atom/second. Adjusted R-square of the fit, $R^2_{adj} = 0.982$.

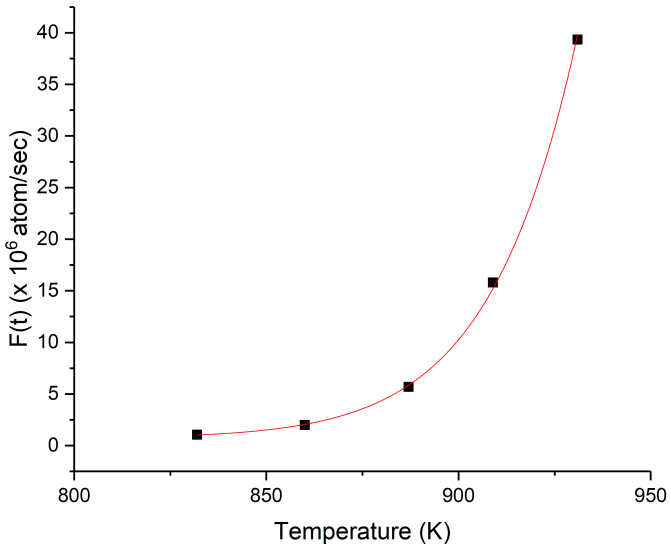

Figure 4.10: Neutraliser's release rate as a function of temperature. The fit of the data (red line) with temperature dependent form of equation 4.23. Reduced chi-square of the fit, $\chi^2_{red} = 138.31$.

the neutraliser. The fit results are shown in figure 4.10. As the results are demonstrate, the MOT number and release rate of the neutraliser are positively effected by

increasing of the neutraliser temperature. The relation between the release rate and the neutraliser temperature corresponds to equation 4.23 and 4.9.

4.5.3 Loading from pulsed mode

The impact of implantation time was also observed in the pulse regime. The ion beam was implanted in the neutraliser at 298 K for an implantation time of 5, 10 and 20 minutes.

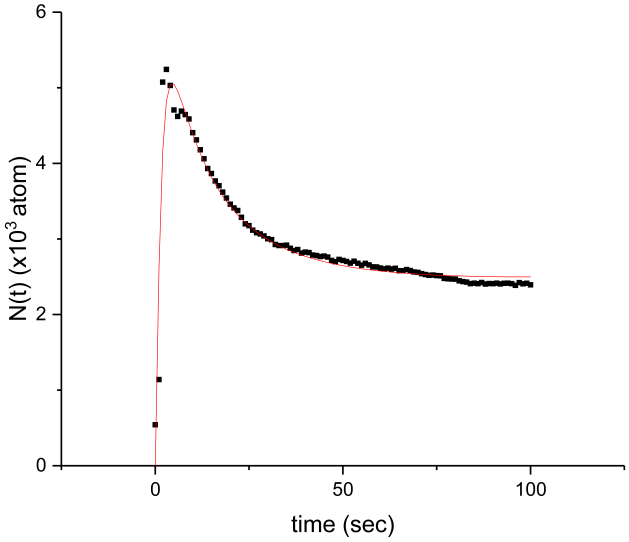

Figure 4.11: MOT population (black square) from the neutraliser after implanted 10^{-10} A ion beam for 20 minute at room temperature. The operating temperature is 930 K. The red line is a fitting curve given by equation 4.16. Adjusted R-square of the fit, $R^2_{adj} = 0.927$.

Implantation time (minute)	MOT peak number ($\times 10^3$ atom)	Implanted atom ($\times 10^9$ atom)	Diffusion time (second)
5	1.68	1.78±0.08	10.07±0.30
10	2.05	6.18±0.14	9.93±0.26
20	5.03	23.68±0.64	9.87±0.31

Table 4.2: Fitting result of Implanted atom number and diffusion time at implantation time of 5, 10 and 20 minutes. The implantation was performed under conditions that average ion beam current is 10^{-10} A and the neutraliser temperature is 930 K.

A MOT loading curve is shown in figure 4.11 which shows that the MOT

number rapidly rises to maximum in short period and then decays to a saturated offset level. The offset level corresponds to loading via bulk atom in neutraliser. Then, the loading curves were fitted with equation 4.19 using the pulse regime release rate, f in equation 4.16. The fitting result (peak trapped number, implanted atom number and diffusion time) are shown in table 4.2.

4.5.4 Loading from continuous mode

The MOT loading in continuous mode was conducted in order to replicate the situation of implanted ^{135m}Cs MOT loading. Because of the short life-time, a considerable amount of the implanted atom decays during implantation process resulting in a small trap number. To minimize the problem, the implanted atoms need to be trapped and cooled immediately after implantation, achieve by MOT loading in continuous mode.

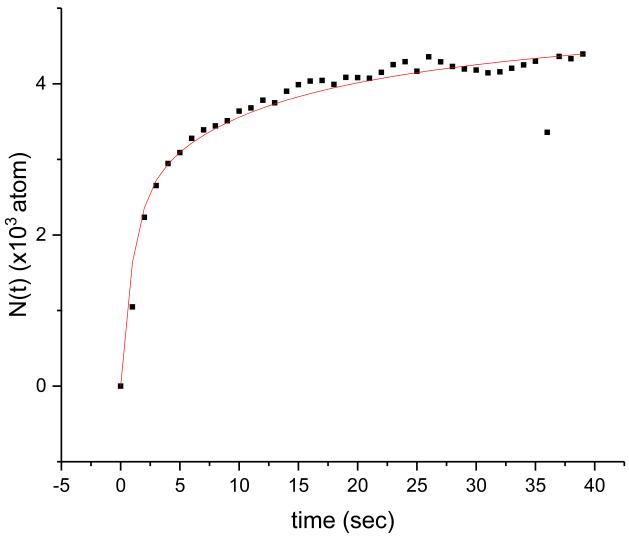

Figure 4.12: MOT population (black square) from the neutraliser in continuous mode with 10^{-10} A ion beam and operating temperature is 930 K. The fit of the data (red line) with equation 4.18 gives the characteristic diffusion time, $\tau_d = 4.38 \pm 0.22$ second. Adjusted R-square of the fit, $R^2_{adj} = 0.943$. The drop of atom number at t=36 s could be caused by surging of background signal outside trap region. The surge does not increase detected fluorescent signal from trap region but weight parameter of background subtraction in fluorescent imaging software resulting fall of trapped atoms number. This problem was later fixed by installation of light-shielding box covering the glass cell and imaging system.

Before loading, the bulk atoms in the neutraliser were minimised by MOT loading from high temperature neutraliser. The MOT number had been monitor until trap signal is minimised. Then continuous mode loading was conducted with temperature from 830 K to 931 K and an averaged ion beam current of 10^{-10} A. The loading curve is shown in figure 4.12.

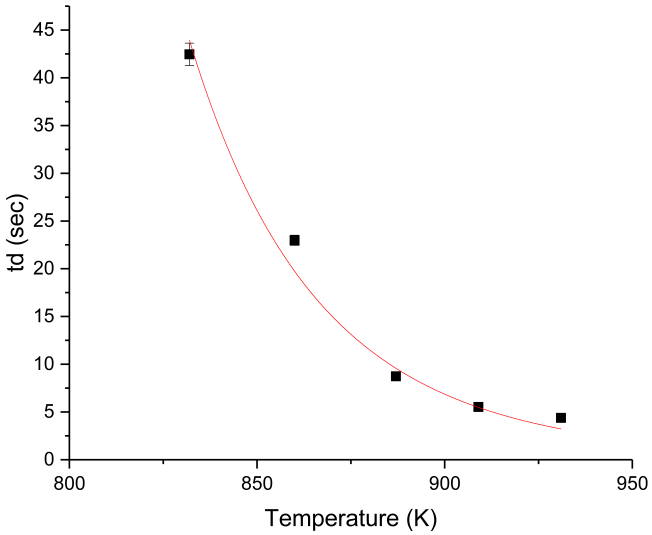

Figure 4.13: Diffusion time as a function of operating temperature in continuous mode. The fit of the data (red line) with equation 4.10 gives the activation energy, $E_a = 1.65 \pm 0.15$ eV. Reduced chi-square of the fit, $\chi^2_{red} = 30.229$.

The loading curves were fitted with equation 4.19 using the continuous regime release rate, f in equation 4.18 in order to extract the characteristic diffusion time, t_d for each temperature. The fitting results are shown in figure 4.13. The relationship between t_d and temperature is explained by Arrhenius equation. To confirm the relation, the data in figure 4.13 was fitted with equation 4.10 with $T_{ref} = 875$ K, to extract the activation energy of Y foil, E_a and the characteristic diffusion time at $T = 875$ K, t_{875}. The results are $E_a = 1.65 \pm 0.15$ eV which is comparable the value report in [88]: 1.8 ± 1.1 eV and $t_{875} = 13.14 \pm 0.84$ s.

In figure 4.14, effect of the neutraliser temperature on the MOT atom number is presented. The exponential increase of the MOT atom number confirms the thermal diffusion role for MOT loading from ion implantation.

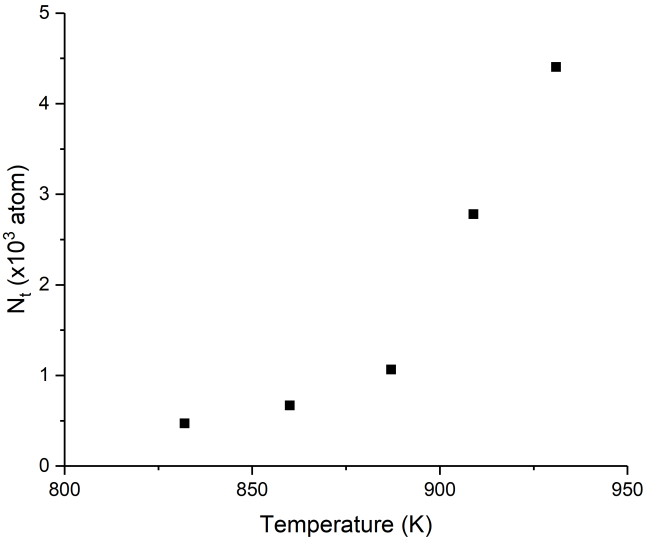

Figure 4.14: MOT atom number as a function of operating temperature in continuous mode.

4.6 Ion implantation of ^{135m}Cs

The ^{135m}Cs isomer is a ^{135}Cs isotope with 1.63 MeV nucleus's excitation energy. The de-excitation of the nucleus back to the ground state occurs via a sequence of two gamma-ray emission processes: first an 846 keV γ-ray and then a 787 keV γ-ray. The half-life, $t_{1/2}$ of ^{135m}Cs is 53 minutes [95]. It is categorized as a shape isomer [2], where a semi-stable nuclear excited state is due to the significant change in the shape of the nucleus with respect with the ground state. The ^{135m}Cs isomer can be prepared by ion implantation [96] based on proton-induced fission of an actinide target.

Ion implantation of $^{135m}Cs^+$ was tested in the ion beam spectroscopy line. The $^{135m}Cs^+$ beam was produced as explain in section 4.1 and focused to impinged on a thin foil, which located at the end of the spectroscopy line. The implantation time was 30 minutes and the γ emission from the foil was detected by germanium detector (Canberra GC7020, energy range from 40 keV to 10 MeV), which was placed behind the foil. The γ spectrum present in figure 4.15.

In figure 4.15, existence of the implanted ^{135m}Cs was identified by two characteristic peaks of 787 keV (E2) and 846 keV (M4). Moreover, γ emission peaks

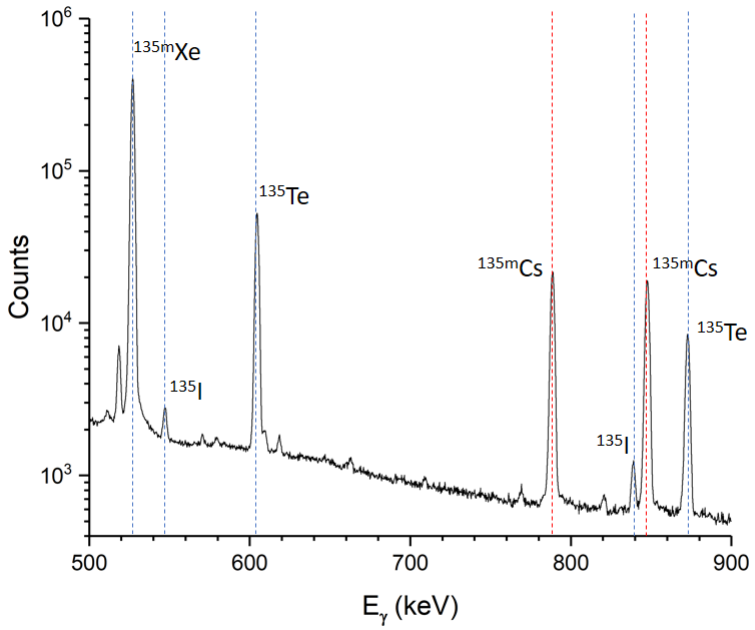

Figure 4.15: γ spectrum produced by a Ge detector after 30 minute implantation.

of other $\frac{A}{q} = 135$ implanted species were also observed. For the proton beam current of 5 μA, taking the detector efficiency and solid angle into account, $^{135m}Cs^{+}$ implantation rate of 2×10^4 ion/s was calculated.

4.6.1 Beam transmission efficiencies measurement

For certain primary beam intensity, the implantation rate in the thin foil can be conversed to an implantation rate of the neutraliser in cold atom chamber by measuring transmission efficiencies of the switchyard to the spectroscopy line and the swicthyard to the neutraliser.

The switchyard-spectroscopy line is calculated by using implantation of ^{112}Rh (half-life is 6.8 second). The half-life was suitable for fast optimisation. The implantations were performed both in the switchyard and the end of the spectroscopy line. The β decay of ^{112}Rh were detected by Si detectors. The measured transmission efficiency of the switchyard and the spectroscopy line is 70%.

The switchyard-neutraliser line is calculated by using $^{136+}$Xe which was produce by adding ^{136}Xe gas to He buffer gas in the target area. The ^{136}Xe ionised by the primary beam during the on-line production of ^{135m}Cs and the ions were accel-

erated and mass separated. Then, the $\frac{A}{q} = 136$ ions were guided through a Faraday cup to measure the ion current and finally implanted in the neutraliser. The ion current measured by the Faraday cup was 95 nA and the current measured from the neutraliser was 38 nA. These lead to 40% of switchyard-neutraliser transmission efficiency.

By comparing the two transmission efficiency and taking implantation rate measured by the Ge detector into account, $\sim 1.2 \times 10^4$ ion/s implantation rate of ^{135m}Cs into the neutraliser was calculated.

4.6.2 Off-line γ-ray spectroscopy of ^{135m}Cs implantation

In order to confirm that the ion implantation of ^{135m}Cs was succeed, an off-line γ-spectroscopy was operated at the neutraliser. An ion beam of $\frac{A}{q} = 135$, ion beam current, $I_0 = 3 \times 10^{-14}$ A, was implanted in the neutraliser for 2 days and then the implantation ion beam was stopped by blocking the ion beam. After the implantation, the neutraliser was left for 7 hours for Y foil to cool down. The cooling down period allow short haft-life implanted species such as ^{135}Sb ($t_{1/2} = 1.68$ s) to decay resulting in minimised radiation from the neutraliser. This is necessary for the safety of neutraliser transfer. Then, the neutraliser was installed in low background counting station which is a chamber located a broad energy germanium detector (Canberra BE3825 detector, 3 keV to 3 MeV energy range) which was place in a lead castle in N_2 atmosphere to minimised background counts. The γ ray spectrum from the neutraliser was measured after the installation. The measurement points is 26 points between 12 to 630 minute after the installation.

In the inset of figure 4.16, the two characteristic γ emission peaks of ^{135m}Cs (787 keV and 864 keV) at four measurement points were identified by the two red dash line. The 846 keV peak was clearly observed in all four measurement points. However, only the 787 keV peaks at 42 and 96 minutes can be identified. At the 144 and 196 minutes, the 787 keV peaks were shifted leftward. The peak shifting correspond to the overlapping of 785 keV peak of ^{135}I which dominated the peak area when the measurement point time is increased. This is because the ^{135}I has the longer haft-life, $t_{1/2} = 6.58$h.

In order to eliminate the contribution of the 785 keV peak to the 787 keV peak, the estimated counts of the ^{135}I's 785 keV peak need to be taken away from the 787 keV peak area. The estimated counts was obtained by measuring of counts ratio, between two emission peaks of ^{135}I. The counts of the two peaks are measure point, i dependent and are located at 546 keV (no interference peak), donated as $A^{I}_{546}(i)$ and the 785 keV, donated as $A^{I}_{785}(i)$. The measurements were conducted at long time measurement points where the 785 keV peak contributed by ^{135}I is dominated. Once the average ratio, $r_{avg} = \frac{1}{\text{number of i}} \sum_i \frac{A^{785}_{I}(i)}{A^{546}_{I}(i)}$ was obtained, the counts of 787 keV of ^{135}Cs, A^{Cs}_{787} was given by

$$A^{Cs}_{787} = A^{Cs+I}_{787} - r_{avg} A^{I}_{546} \ , \tag{4.24}$$

where A^{787}_{Cs+I} is the total counts of interfering peak at 787 keV area. The decreasing of A^{Cs}_{787} and A^{Cs}_{846}as a function of time are shown in figure 4.16. The data were exponential fitted to extract haft-life of ^{135m}Cs. The averaged fit result is $t_{1/2} = 53.5 \pm 1.6$ minute.

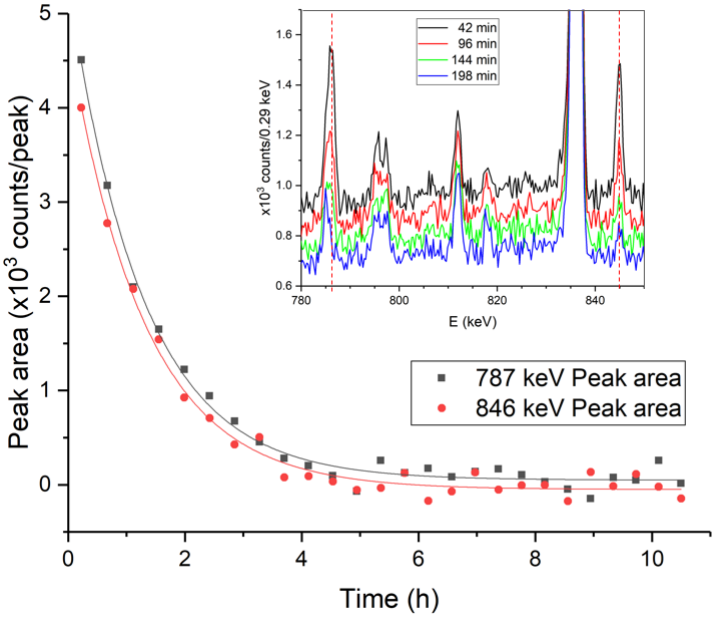

Figure 4.16: γ decay curve of transitions of ^{135m}Cs.

4.7 Trapping of ^{135}Cs with the upgraded frequency control system

After characterisation of neutraliser by means of^{133}Cs MOT and implantation test run of ^{135m}Cs, an Attempt for trapping of ^{135}Cs was performed in order to further test MOT detection sensitivity before trapping of ^{135m}Cs. Although, ^{135}Cs is not directed long term goal of this project, it was chosen as prior target species before trapping of ^{135m}Cs because it has been trapped and is more populated compare to ^{135m}Cs.

In 2002, M. D. Di Rosa et al. successfully trapped ^{135}Cs using VCMOT and reported its spectroscopic data as shown in table 1.3. This is an important referent point for our frequency control system.

^{135}Cs is a long-lived isomer (2.3×10^6 years), which could be assumed as a stable isotope. Therefore it can be implanted and stored regardless time conditions. Additionally, apart from being directed product of proton-induced fission, ^{135}Cs is also daughter product of other short-live $\frac{A}{q} = 135$ isotopes produced by the proton-induced fission such as ^{135m}Cs and ^{135}Xe. This increase ^{135}Cs population by time.

4.7.1 Upgraded frequency control system

According to hyperfine structure diagram in figure 1.2 and isotope shift shown in table 1.2, frequency shifts of other caesium isotope MOT relative to ^{133}Cs MOT transition frequency, Δf_A is calculated by

$$\Delta f_A = \Delta \nu_c - (\delta_F^A - \delta_F^{133}) + (\delta_{F'}^A - \delta_{F'}^{133}) \,, \tag{4.25}$$

where A is caesium isotope mass number. According to the figure 1.2 and table 1.2, ^{135}Cs MOT Frequency shifts, Δf_A which calculated from equation 4.25 are reported in table 4.3

As shown in the table, frequency shift for ^{135}Cs MOT is large that the current frequency control system cannot provide. In order to perform ^{135}Cs MOT, the frequency stabilisation and control part explained in chapter 2 were modified, while

the ^{133}Cs trapping capability still remain.

Figure 4.17 show that the modified frequency control system is comprised of three AOM configurations. An extra double-pass AOM setup using a 110 MHz AOM was added as DP-AOM 2 in order to shift frequency of former DP-AOM 1 output beam before it enter the DAVLL setup to perform frequency locking. The AOM was added in order to widen frequency tuning length of MOT cooling laser to enhance the system capability for trapping of both ^{133}Cs and ^{135}Cs. The DP-AOM 1 and DP-AOM 2 work as active frequency controller which can alter MOT cooling frequency while the DAVLL is operated. The DP-AOM 3 only work as fast switch and intensity controller for MOT cooling beam. The AOM 3 driven frequency is fixed to avoid misalignment in MOT beams configuration because of AOM output beam axial shift.

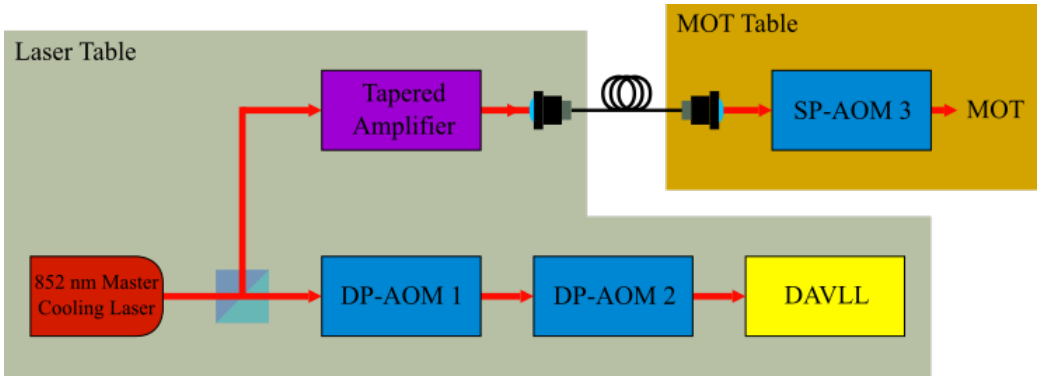

Figure 4.17: Modified MOT cooling frequency control. The 852 nm Master Cooling laser is the cat's eye configuration NarrowDiode Laser explained in section 3.2. The modified part is DP-AOM 2 on laser table (grey area), while single-pass configuration of SP-AOM 3 on MOT table (brown area) is unchanged.

The shifts contributed by the AOMs have a reference point at $6^2S_{1/2}\ F = 4$ to $6^2P_{3/2}\ F' = 4,5$ transition of ^{133}Cs, which was used as a locking transition for MOT cooling frequency. Table 4.3 show required RF frequency amplitude, which were applied to AOMs in order to achieve observable MOT cooling detuning,$\delta = -2.65\Gamma$ and on-resonance repump frequency for ^{133}Cs and ^{135}Cs MOT. The detuning was derived from [23]. Moreover, relative total shift with ^{133}Cs MOT frequencies also report in the table.

AOM	^{133}Cs	^{135}Cs
AOM 1 (MHz)	-95.9	110.0
AOM 2 (MHz)	79.9	bypassed
AOM 3 (MHz)	79.9	79.9
Cooling shift (MHz)	0	-252
Repump shift (MHz)	0	263

Table 4.3: AOMs's driven RF frequencies for trapping of ^{133}Cs and ^{135}Cs. For both specie, number illustrated in this table are set to provide -2.65Γ detuning from $6^2S_{1/2}$ $F = 4$ to $6^2P_{3/2}$ $F' = 5$ transition for cooling laser and on-resonance of $6^2S_{1/2}$ $F = 3$ to $6^2P_{3/2}$ $F' = 4$ transition for repump laser. The total shift of cooling and repump relate to its transition frequency.

4.7.2 Preliminary evidence of ^{135}Cs trapping

Before trapping ^{135}Cs, the atomic source was loaded by ion implantation of $\frac{A}{q} = 135$ ions in the neutraliser for 64 hours. Energy and current of proton beam are 50 MeV and 5 μA, respectively. The measured implantation rate of ^{135}Cs is $\sim 11.2 \times 10^3$ atoms/s. The implanted neutraliser was left for a month in order to ensure that other implanted radioactive specie decays and some of it decay to be ^{135}Cs. Then, the experiment was switched on and the implanted ^{135}Cs was released by resistive heating of the neutraliser above 800 K. The total beam powers of MOT cooling and repump were 127 mW and 15 mW respectively. MOT lasers were tuned by AOM1 and AOM2 to the respective transition frequencies reported in table 4.3.

For the MOT cooling laser, the frequency was locked to the expected -2.65Γs detuning from $F = 4$ to $F' = 5$ transition peak. During the operation, the cooling frequency was $\pm$10 MHz scanned around the calculated transition frequency in order to cover uncertainty of MOT cooling frequency. The frequency was changed with step of 0.5Γ per measurement.

For the MOT repumper laser, the frequency was tuned to $F = 3$ to $F' = 4$ transition frequency, however, the laser have to run without frequency locking because of lacking of AOM to provide large frequency shift related to ^{133}Cs repump transition frequency. In order to compensate the disadvantage from frequency uncertainty, the frequency was $\pm$55 MHz modulate with modulation frequency of 100 kHz. The

repump central relative frequency was slowly scanned during a measurement by applied 400 mVp-p, 10 mHz modulation which applied to the repump laser modulation input, this modulation correspond to +140 MHz to +410 MHz relative to ^{133}Cs MOT repump frequency and 5.4 MHz/s scanning rate. The modulation range was set to cover the expected repump transition frequency of +263MHz. Moreover, frequency of the repump laser are monitored by a wavemeter (MWM002 Laser Wavemeter from MOGlabs) during trapping.

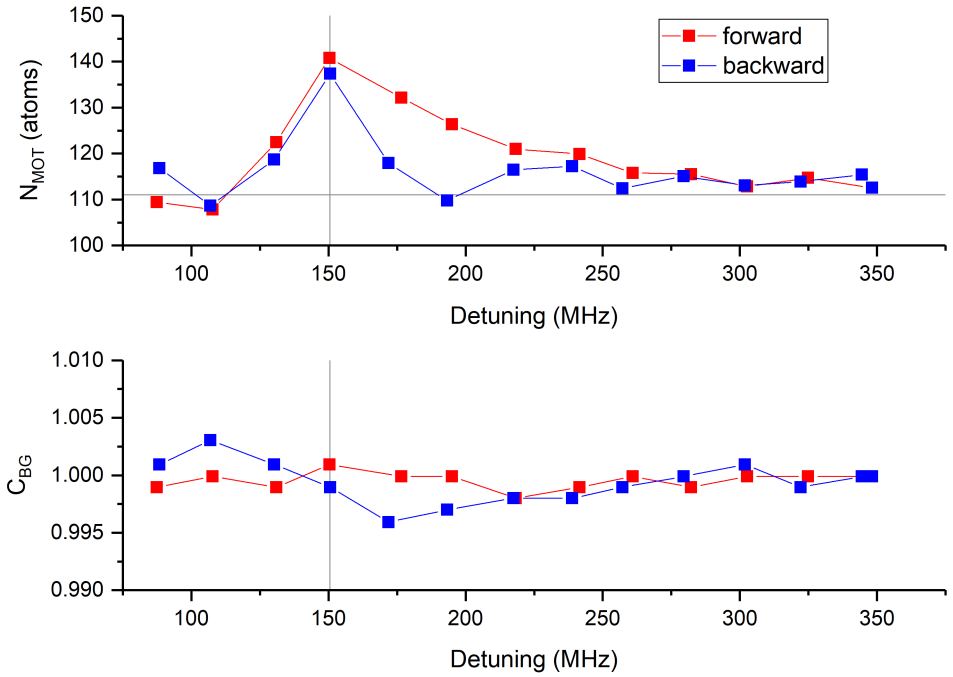

Figure 4.18: MOT fluorescence and background signals detected during forward (red) and backward (blue) repump central frequency scanning. The vertical lines mark where fluorescent peaks were detected. The horizontal line is represent average black ground level. Raw Data using in this figure was collected by my colleagues, Dr. Alexandros Giatzoglou and Dr. Luca Marmugi.

The fluorescence signal obtained in this experiment is shown in Figure 4.18, where two peaks can be clearly observed. The first peak was detected at repump detuning, $\delta_{repump} = +148$ MHz and the second was at $\delta_{repump} = +151$ MHz. In middle of the peaks, there was a turning point of the frequency scanning, which was called conversion frequency, $\delta_c = +348$ MHz. When the peaks were detected, cooling detuning is -2.65Γ.

For the cooling frequency, the observed relative frequency is consistent with [25]. However, the observed +150.37 MHz and +150.59 MHz of repump relative frequency are not consistent with the expected value of +236 MHz. This could be explained that the central relative frequency of the repump has drifted down, hence the frequency scanning range did not cover the expected frequency. Alternatively, uncertainty in the readout of the wavemeter could cause the apparent contradiction. Further tests would be necessary to rule out possible systematic effects, or to confirm the correctness of the frequency reading. In this sense, we note that - although not commonly used - there are other far resonant frequencies [97] for the repumper that can lead to MOT loading.

Unfortunately, at the time of this thesis, it was not possible to replicate the experiment of ^{135}Cs MOT because of depletion in the neutraliser and limited beam time available. However, one should highlight that this preliminary data is significant: the observed peaks are observed above the average noise level equivalent to 111 ± 4 atoms. In addition, one can exclude abrupt variations of the background conditions, as demonstrated by the behaviour of the background compensation constant, C_{BG} in bottom graph of figure 4.18.

Chapter 5

Conclusions and outlook

5.1 Summary

My work in the context of the ultra-cold caesium isomer project was divided into three parts: 1) design, construction and test of a laser system for trapping of ^{133}Cs, 2) operation of a VCMOT of ^{133}Cs and characterisation of the MOT parameters 3) characterisation of MOT loaded from a neutralised ionic beam. In addition, preliminary evidence of a ^{135}Cs MOT was also presented.

The first part took place at University College London. Here, the laser sources for the ^{133}Cs MOT were assembled and tested. The system consisted of cooling and repump ECDLs. The output beams of the system were conveyed through optical fibres to a MOT table, where the double chamber vacuum system was located. On the MOT table, a double MOT of ^{133}Cs was assembled and tested. This ensured that the laser system and the MOT were fully functional, an essential step in preparation of the following phase.

For the second part, the laser system was transferred to the accelerator laboratory, University of Jyväskylä in order to demonstrate a MOT of caesium isotopes and isomers. After the laser system was installed, the master lasers of the MOT cooling and repumping were replaced with two commercial ECDLs in order to enhance the laser system performance. The mode-hop free tuning range of the lasers were characterised by Doppler-free saturated absorption spectroscopy. On a different optical table, a VCMOT experiment which consisted of two main parts, the

MOT optical alignment system and the vacuum system, was assembled. VCMOT of ^{133}Cs was demonstrated in a glass cell and the MOT parameters were characterised by means of absorption imaging to determine the optimal MOT control parameters to be used in the next stage. In this part, the MOT input parameters were controlled by a NI-6009 DAQ, interfaced to a computer via Labview.

In the third part, in the accelerator laboratory, the MOT vacuum system was connected to the ion guide isotope separation on-line (IGISOL) facility. The glass cell was replaced by a custom glass cell with the inner surface coated by an organic coating (polydimethylsiloxane, PDMS) to reduced atomic losses. The chamber is also equipped with an Y foil mounted inside. The foil acts as a 'catcher' and 'neutraliser': it serves as a target and stopping stage of a 30 keV ion beam, and allows one to transform the slowed down ions into neutral atoms. In detail, $^{133}Cs^{+}$ (or $^{135,135m}Cs^{+}$) were implanted into the neutraliser which works as atomic source for the MOT, thanks to resistive heating. The MOT loading curves for several heating temperatures and implantation time were characterised by fitting the data with a mathematical model in order to extract the activation energy of the neutraliser, $E_a = 1.65 \pm 0.15$ eV. The measured activation energy is lower than yttrium's work function of 3.1 eV.

After that, $^{135,135m}Cs^{+}$ ions, with the latter being a candidate isomer for the demonstration of generation of coherent gamma photons, were implanted into the neutraliser for 2 days. Then the implanted neutraliser was removed and placed in a low background emission environment in order to measure γ-ray emission. The γ-ray emission peaks of ^{135m}Cs were detected and ^{135m}Cs half-life of 53.5 ± 1.6 minutes was calculated to confirm successful of ^{135m}Cs implantation.

Finally, trapping of ^{135}Cs was attempted using spectroscopic data from [25]. As a result, two sharp increases in MOT population - detected via fluorescence imaging - were observed at a cooling frequency consistent with the result reported in [25]. However, the repump relative central frequency that generated the peaks was different from the expected value. Unfortunately, the presence of ^{135}Cs MOT could not be confirmed because the experiment could not be repeated because of

the depletion of the neutraliser and unavailability of beam time.

5.2 Towards ultra-cold isomers

The experimental setup described in this thesis is designed to produce a MOT from ion implantation and specifically from implanted caesium isomers. The long-term goal of the project, which is the production of ultra-cold caesium isomers, will require the current setup to be upgraded. There are three main points which need to be improved upon the current setup: 1) the AOMs based frequency control ability of laser system is limited and cannot be applied to trap all target caesium isotopes (^{133}Cs, ^{135}Cs, and ^{135m}Cs) without reconfiguring the AOMs setup. 2)short trap lifetime caused by high background pressure and 3) the temperature achievable in a MOT has a lower limit, given by the recoil temperature. This is not cold enough for ultra-cold temperature regime. The solutions for these problems, as planned for the future developments of the project are discussed in the following.

5.2.1 Laser tuning range extension via offset locking

Currently, the MOT lasers frequencies tuning range, as determined by the AOMs based frequency control system, is only suitable for cooling and trapping of ^{133}Cs and ^{135}Cs. A possible solution to be able to trap other species, including the desired isomer ^{135m}Cs, is the installation of offset phase lock systems.

The offset phase lock systems (OPLS) [98] provide wide laser frequency tuning range of $\geq$ 9.5 GHz by detecting the beat note signal from the interference of two laser beams. The frequency difference between the two lasers is electronically stabilised, therefore, the OPLS offer fast and precise frequency control ability.

The lasers used in the offset lock system are called customarily master and slave laser. The master laser works as reference laser which is frequency locked, in our case is by DAVLL. For caesium, the locked frequencies of the master laser for cooling and repumping are $6^2S_{1/2}\ F = 4$ to $6^2P_{3/2}\ F' = 5$ and $6^2S_{1/2}\ F = 3$ to $6^2P_{3/2}\ F' = 4$, respectively. The slave laser frequency is controlled by the offset phase lock servo, which has the beat note signal as an input, in order to maintain a constant frequency difference from the locked master laser.

For trapping of ^{135}Cs, an OPLS will be installed and used as the MOT repump laser and another OPLS will be added as the MOT cooling laser for trapping of ^{135m}Cs.

5.2.2 Double vacuum chamber

An unavoidable problem of the vapour cell MOT is the short trap lifetime because of the high background collision rate. As discussed in section 4.5.1.1, the loading rate for a MOT is proportional to the background number density of the species to be trapped. However, the background density also increases the trap background collision rate. Therefore, in VCMOT, the increase in the MOT atoms number is saturated as the atom production rate increases. This is not a good starting point for the trapping of caesium isotopes, which have a short lifetime and ultra-low production yield.

To circumvent this problem, a double chamber vacuum system needs to be built [99][100]. In this way, as detailed in chapter 2, the second chamber will have a much lower background pressure ($P \leq 10^{-10}$ mbar). This will allow us to create a second MOT, loaded from the first one, in an environment with a substantially decreased collisional rate. Consequently, the trap lifetime is drastically increased, and further steps of the experimental sequence can be implemented.

5.2.3 Degenerate Raman side-band cooling

The Degenerate Raman side-band cooling (dRSC) [101][102][103] is a cooling technique that lowers the temperature of trapped atoms down to a few micro Kelvin [35] with high cooling efficiency [104].

The dRSC mechanism can be explained as an optical pumping process in optical harmonic traps such as an optical dipole trap or an optical lattice [105]. The optical pumping alone populates the lowest magnetic sublevel. However, the process cannot manipulate the trap population to the lowest vibrational state of a trap's potential well. To do so, the optical pumping process needs to operate on required conditions, which are free population transfer between magnetic sub-levels and the Lamb-Dicke regime.

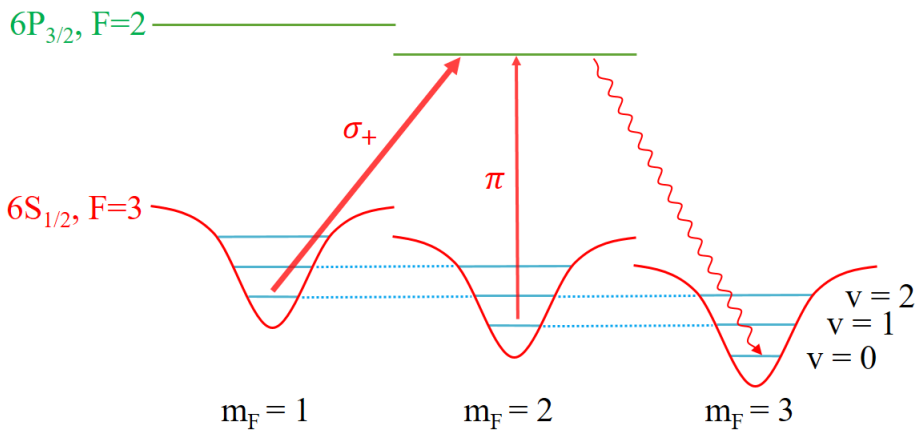

Figure 5.1: dRSC Cooling scheme of cold caesium atoms: ground state lattice potentials (red line wells) of magnetic sub-levels, m_F are split by Zeeman shift. The magnitude of the shift is equal to the energy gap between vibration states, v (blue dash line). Trapped atoms in the lattice are optically pumped to an excited state (green line bar) by optical pumping light, σ_+ and repump light, π. Finally, atoms decay (red wave line arrows) to both the lowest magnetic sub-level and vibrational level.

The free population transfer between vibrational states of individual potential wells of each magnetic sub-level is generated by the vibrational states degeneracy and Raman coupling. Moreover, to cool atoms down efficiently, trapped atoms need to be in the Lamb-Dicke regime [106], where the energy space of vibrational states is significantly larger than the recoil energy of spontaneous emission. Therefore the change of vibrational quantum number after spontaneous decay is suppressed.

Figure 5.1 show that, pre-cooled atoms from optical molasses are loaded into an optical lattice which is located in a uniform magnetic field. The magnetic field generates Zeeman energy shift between magnetic sub-levels, Δm_F equal to the vibrational energy of the lattice potential well, $\Delta v = \hbar\omega$. In this condition, degeneracy between $|F, m_F; v>$ and $|F, m_F - 1; v - 1>$ is created. The degeneracy and the degenerate Raman transition created by the optical lattice beams allow free population transfer between the degenerate vibrational states. Then, a circularly polarised beam is applied as an optical pumping beam that pumps atoms to a lower magnetic sub-level. Because of the Lamb-Dicke regime, the atom decay to a lower magnetic

sub-level without changing of vibrational state. Eventually, the trapped atoms are spin-polarised by the optical pumping process and also transferred to a dark and lowest vibrational ground state. Unlike the evaporative cooling in an optical trap, the dRSC can achieve an ultra-low trap temperature without sacrificing high energy trapped atoms. The cooling efficiency of the dRSC can be as high as 70% [104]. Therefore, this technique is ideal to generate ultra-cold isomers, given the expected very low population since the MOT phase. With the abovementioned high cooling efficiency, BEC from a low-populated trap is attainable.

These upgrades are being implemented at UCL and will be completed by the other members of the group.

Appendix A

First-order feedback of an external cavity diode laser (ECDL)

The procedure to align ECDL's 1^{st} order beam to be fed back to the laser diode is detailed in the following.

Step 1: The ECDL is roughly setup as shown in figure 2.1. The output of the laser diode is collimated and directed onto the diffraction grating with an angle of approximately 45°. When the 1^{st} order beam is far from the optimal angle for feedback (i.e. the cavity is not aligned), it is not overlapped with the diode laser output beam and can be detected by an infrared card.

Step 2: The grating orientation and hence the input angle of the laser beam is rotated by a vertical and horizontal fine adjustment screw until the 1st order beam is injected back into the diode. An indication that the alignment is close to the optimal feedback condition is the presence of two red spots which can be observed on an infra-red card at a large distance from the grating output [49]. One is from the 0^{th} order output of the grating and the other is the first-order diffracted beam's reflection from the collimating lens front surface.

Step 3: The driving current of the laser diode is reduced to about the threshold current of the laser diode. At this current, an increase of diode laser output power due to the feedback is easier to be observed. The 0^{th} order beam from the grating (i.e. the output beam) is measured by a power meter and fine tuning of vertical angle of grating is done until the highest output power is achieved.

Step 4: The diode driving current is reduced to the new threshold which should be at lower driving current, and step 3 is repeated until the lowest threshold current is reached. At this point, the laser feedback alignment is completed, which provides single mode operation and large tuning range.

Step 5: The diode driving current is increased until the desired optical power is reached. The wavelength of the emitted laser radiation is measured with a wavemeter. The horizontal grating angle is tilted until the desired wavelength, in the present case 852 nm, is obtained.

In order to confirm that the laser output wavelength is resonant with the wanted atomic transition, 852 nm in case of caesium atoms, the laser beam is passed through a caesium reference vapor cell and the fluorescence due to spontaneous emission is observed with the help of a CCD camera.

Appendix B

Double-pass AOM alignment steps

An acousto-optical modulator (AOM) is an optical device which can control power [107] and frequency of an input laser beam by the application of an acoustic radio frequency (RF) produced by a piezoelectric transducer to the crystal inside the AOM [108]. The RF modulation forms a spatially periodic refractive index in the crystal which behaves like a diffraction grating for the laser. By considering the conservation of momentum and the conservation of energy, the condition for constructive interference is,

$$m\lambda = 2\Lambda \sin\theta_i \tag{B.1}$$

where m is the diffraction order, Λ is the acoustic wavelength and θ_i is the incidence angle of the laser beam onto the AOM. In terms of photon-phonon scattering, the photon momentum is increased or decreased by the phonon energy, in other words, the laser output frequency is changed. The change for single pass AOM, Δf_L, is written as,

$$\Delta f_L = m\Omega \tag{B.2}$$

where m is the diffraction order which can be a positive or negative integer, and Ω is the acoustic wave frequency.

The single pass AOM has a significant disadvantage as highlighted by equation B.1: a change of frequency or wavelength of the 1st order beam causes a shift of the diffraction angle which leads to a misalignment of the single pass AOM output at long distance from the AOM. The double pass AOM configuration overcomes this

limitation, and allows for the beam line direction accuracy to be maintained. The frequency can be changed, without consequences on the alignment. The key element of the double-pass configuration consists in the retro-reflection of the 1^{st} order output back to the AOM. The 1st order output beam of the double pass AOM will then be in the same direction and overlap the input beam. In the double pass AOM configuration, the output beam direction is maintained irrespective of the variation of the AOM frequency, at the cost of a higher loss in optical power.

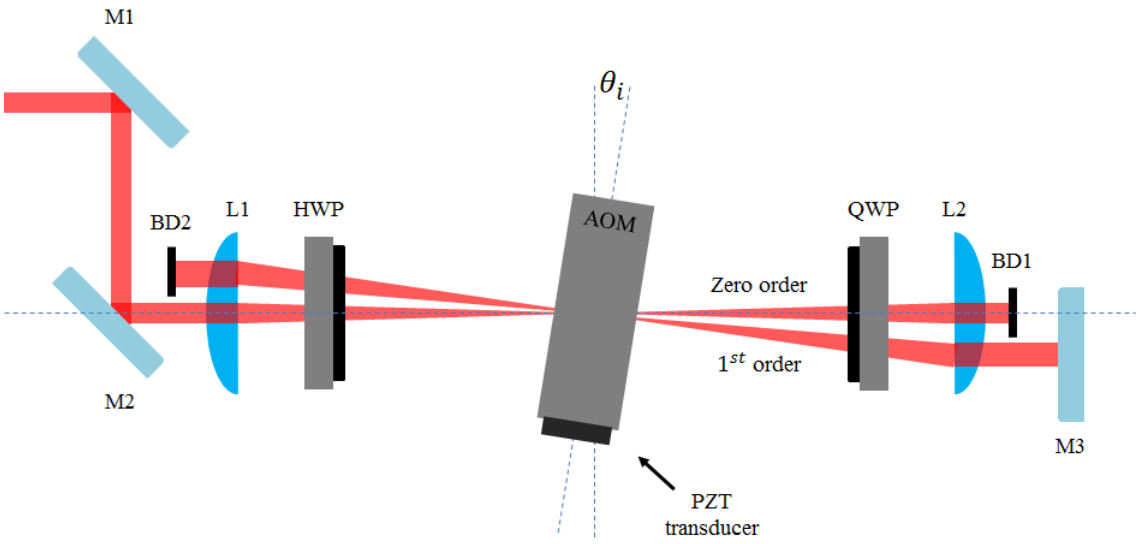

Figure B.1: Double-pass AOM configuration

The double pass AOM configuration is shown in figure B.1, and the alignment procedure is detailed in the following.

Step 1: The laser beam is aligned to be parallel to the optical table plane and also aligned to the axis determined by the position of mirrors M1 and M2.

Step 2: A $F = 200$ mm plano convex lens, L1 is placed after mirror M2. The beam passes through the center of the lens in order to maintain the beam direction along the vertical and horizontal axis. The beam is focused in order to reduce the beam waist so to match the AOM active aperture which is 2.5×0.6 mm^2. The appropriate optical beam waist, d can be calculated as a function of the lens focal length by,

$$d = \frac{1.27F\lambda}{D} \tag{B.3}$$

where F is the focal length of the lens, λ is the laser wavelength and D is the $1/e^2$ radius of the input beam. In the present case, $D \simeq 2/e^2$ mm and $d \simeq 0.8$ mm.

Step 3: A $F = 200$ mm plano convex lens, L2 is placed roughly 400 mm away from L1 in order to collimate the beam.

Step 4: The AOM is placed at the midpoint between lens L1 and L2. The vertical and horizontal position of the AOM is optimized so that the laser beam is fully transmitted through it, as it can be verified by an infrared card.

Step 5: The incident angle of the beam is adjusted by rotating the AOM until the 1^{st} order of diffraction appear. The direction of the 1^{st} order beam is shifted in the same direction than the acoustic wave of the AOM.

Step 6: The incident angle of the AOM's input beam is finely optimized again by using the two mirrors, so to to maximize the output of the 1^{st} order. The 0^{th} order is blocked by a beam dump.

Step 7: The optical path length of the beam is shortened because of the difference of the refractive index of the AOM's crystal and air. Therefore, the collimation of 1^{st} order beam should be redone. This completes the single pass configuration alignment. The following alignment steps are for the double pass configuration.

Step 8: The 1^{st} order beam is retro-reflected back into the AOM by the mirror M3. The 1^{st} order output beam of the double pass configuration is overlapped to the input beam but in opposite direction. The 0^{th} order output of the retro reflected beam is blocked by a beam dump.

Step 9: A quarter wave plate is added in order to rotate by 90° the 1^{st} order output beam polarization. Then the beam is reflected by a polarizing beam splitter to the DAVLL saturated absorption spectroscopy.

Appendix C

AC Stark shift

An optical dipole trap is a conservative trap which traps atoms by the dipole force generated by the optical dipole potential gradient [109]. The dipole force exploits the AC stark shift of the ground state energy level of the atoms and the intensity gradient of the trapping laser field. The energy shift, or trap depth, depends on the intensity of the trapping laser field, I and its detuning from atomic resonance. The ground state energy shift of a multi level atom in a dipole trap is given by [110][111],

$$\Delta_{F,m_F} = \frac{I}{2\varepsilon_0 c\hbar} \times \sum_{\gamma',F',m_{F'}} \delta_{\gamma',F';\gamma,F} |\langle \gamma, F, m_F | er_0 | \gamma', F', m_{F'} \rangle|^2, \tag{C.1}$$

where the detuning factor is,

$$\delta_{\gamma',F';\gamma,F} = \frac{1}{\omega_{\gamma',F';\gamma,F} + \omega} + \frac{1}{\omega_{\gamma',F';\gamma,F} - \omega} \tag{C.2}$$

and

$$\begin{aligned} |\langle \gamma, F, m_F | er_0 | \gamma', F', m_{F'} \rangle|^2 &= d^2 (2F+1)(2F'+1) \\ &\times \begin{pmatrix} F' & 1 & F \\ M_{F'} & 0 & -M_F \end{pmatrix}_{3j}^2 \begin{Bmatrix} J & J' & 1 \\ F' & F & 3/2 \end{Bmatrix}_{6j}^2, \end{aligned} \tag{C.3}$$

where d is the transition dipole matrix element.

In a two-level system, the dipole force determined by the light shift gradient

can be written as [14],

$$F_{dipole} = -\nabla(\Delta_{F,m_F}) = -\nabla\left(\frac{\hbar\Omega^2}{4(\omega-\omega_0)}\right) \tag{C.4}$$

where ω_0 is the transition angular frequency between the ground state and the excited state of the atom, Ω is the Rabi frequency defined by

$$\Omega = \frac{\langle g|\,\mathbf{p}\cdot\mathbf{E_0}\,|e\rangle}{\hbar} \tag{C.5}$$

where $\mathbf{p}$ is the electric dipole moment associated with transition between the ground state $|g\rangle$ and the excited state $|e\rangle$ and $\mathbf{E_0}$ is the amplitude of the electric field.

Appendix D

Pictures of experimental sketches and diagrams

Figures illustrated in this thesis are sketches and diagrams because they can express information and features of the experimental setup and objects better than pictures. However, I would add pictures of some figures in this thesis to provide the actual scale of this experiment to the reader. Ultimately, I hope these photos make this thesis more exciting and demonstrate the beautifulness of experimental physic research.

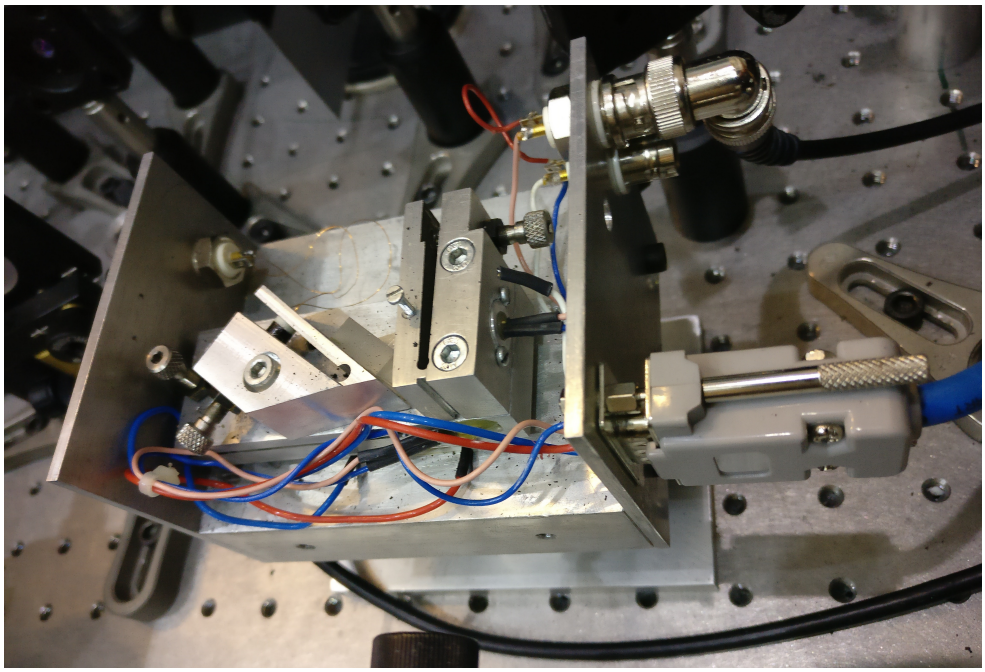

Figure D.1: Photo of ECDL in Littrow configuration.

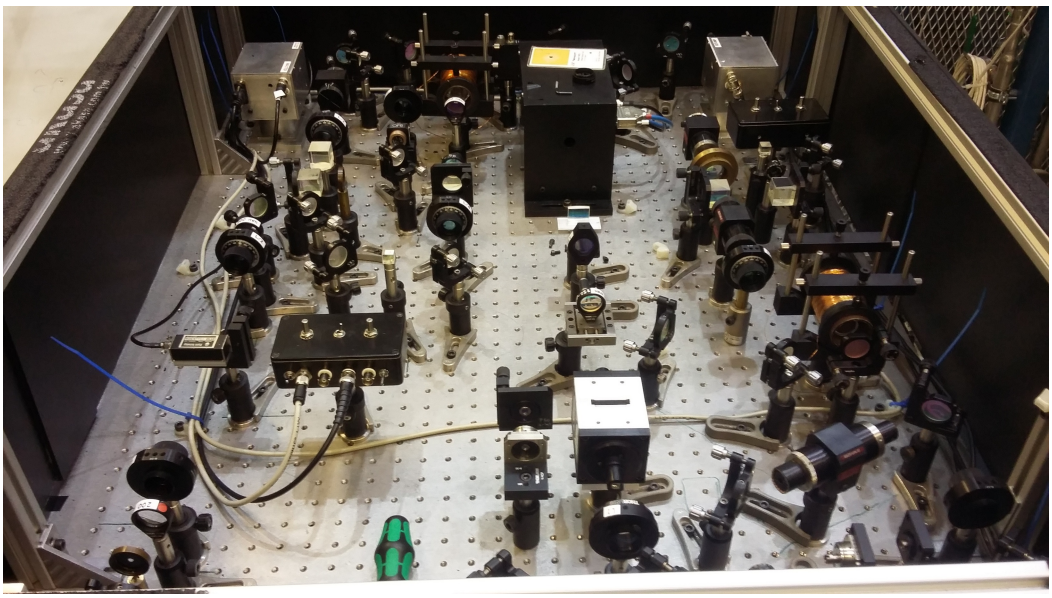

Figure D.2: Photo of Laser system use in this experiment.

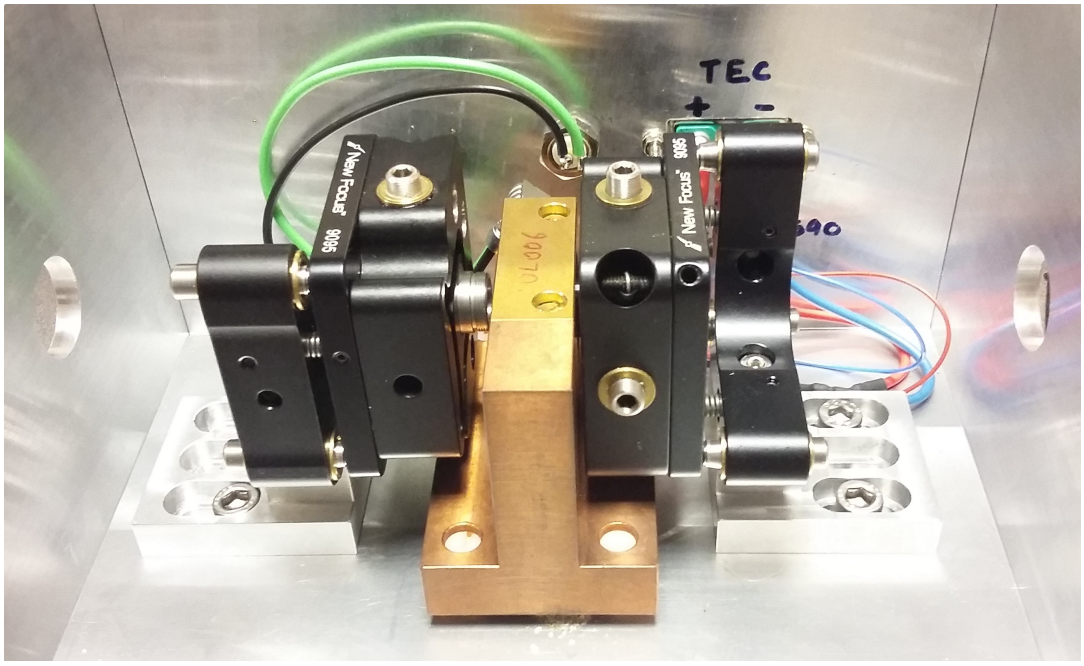

Figure D.3: Photo of Tapered amplifier.

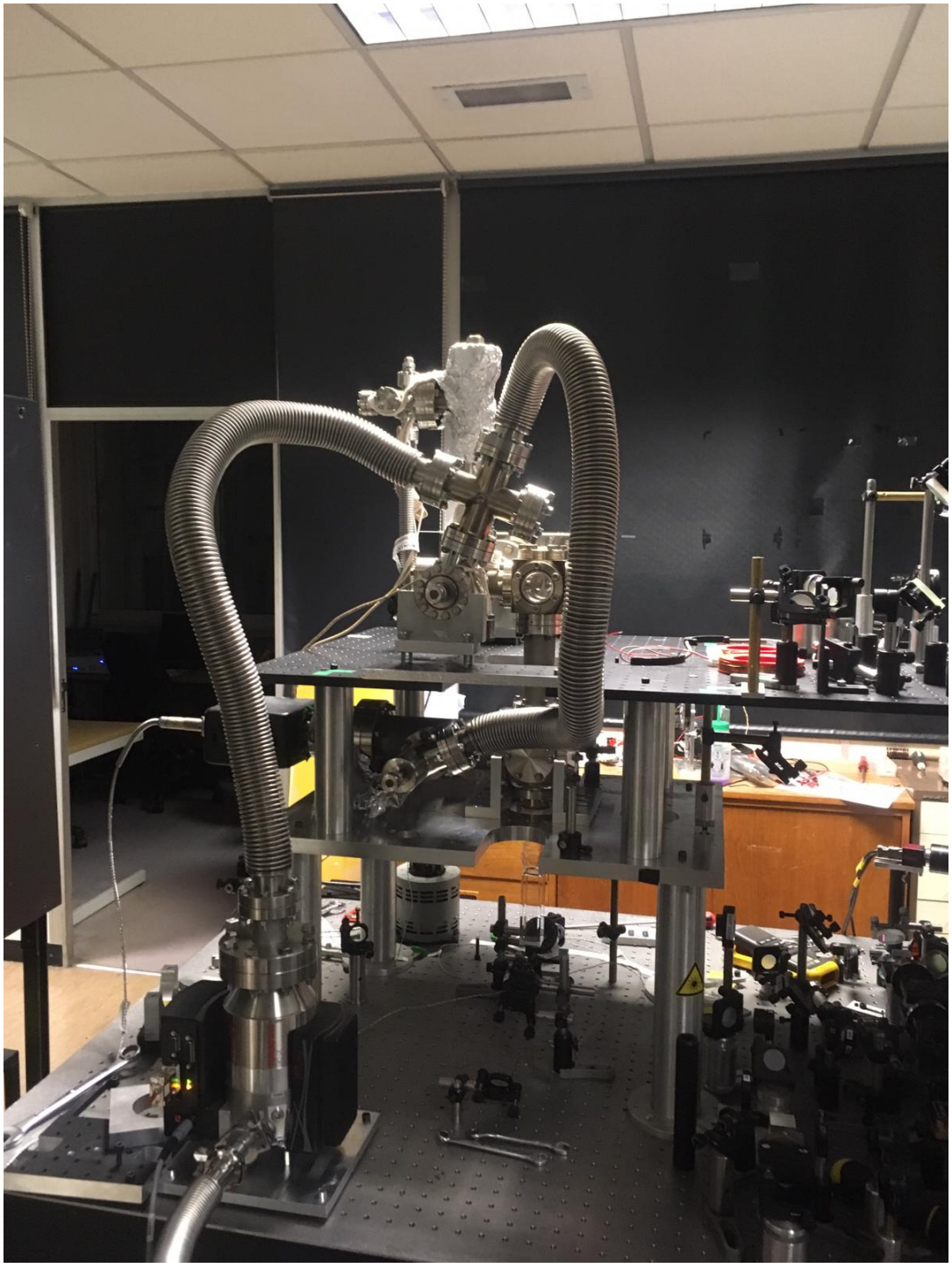

Figure D.4: Photo of vacuum system for double ^{133}Cs MOT.

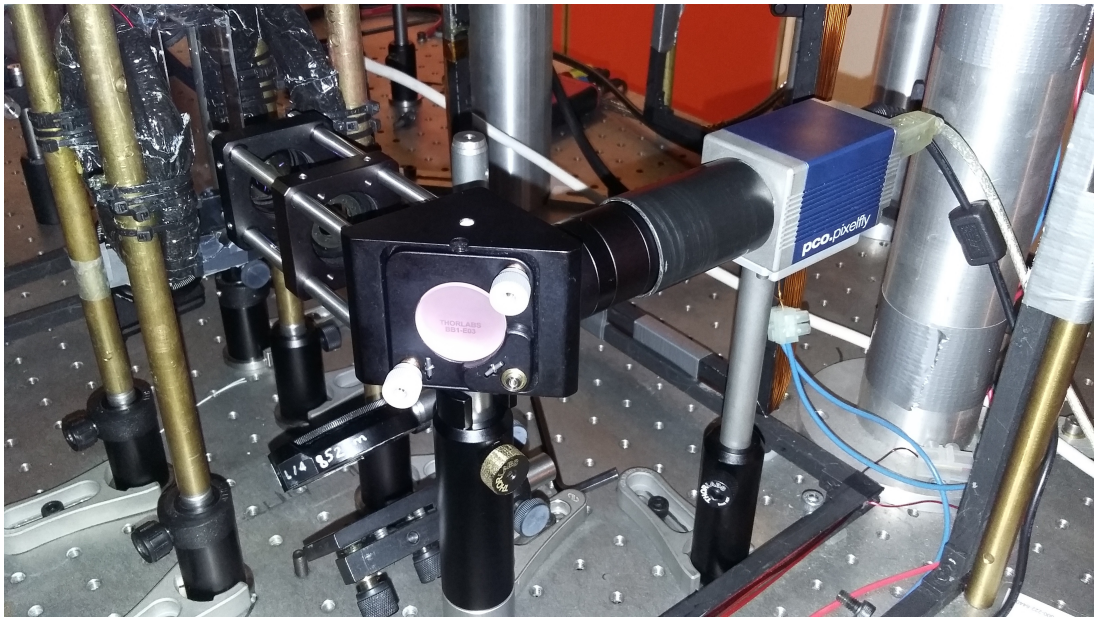

Figure D.5: Photo MOT imaging optical setup.

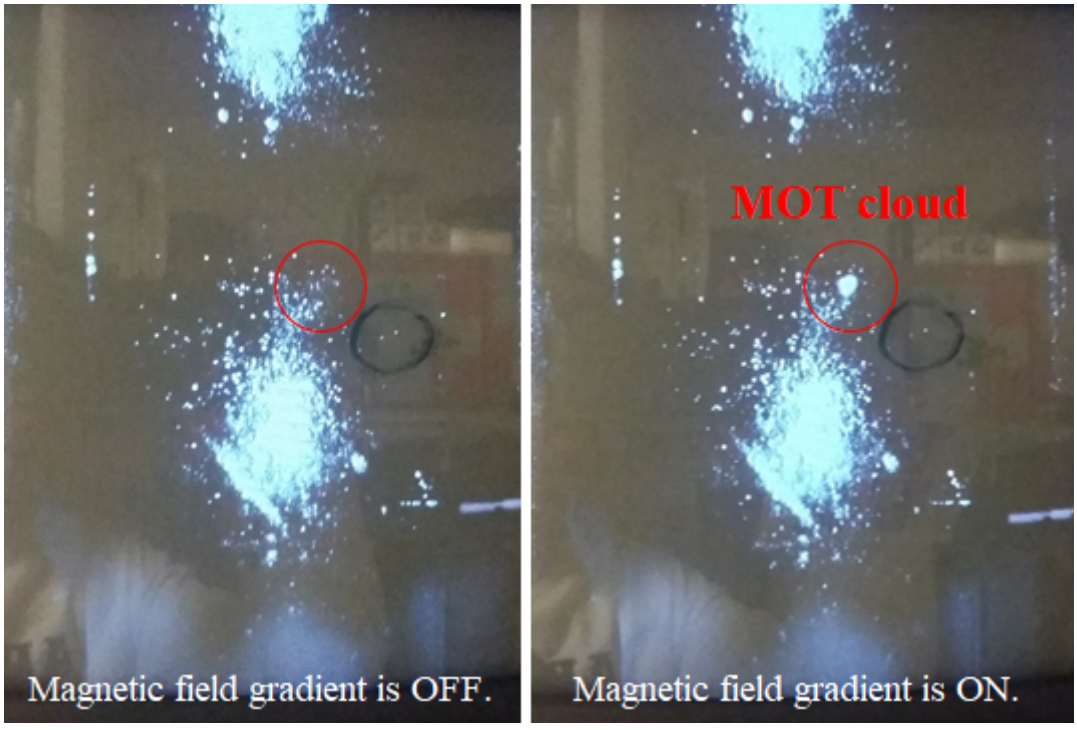

Figure D.6: Photo of MOT cloud in present of magnetic field gradient observed by an infarred camera.

Figure D.7: Photo of laser system contained in a wooden box (left) and the ^{133}Cs MOT optical setup (right) in the Accelerator Laboratory of the University of Jyväskylä. The bottom picture show area of the cold atom experiment in the accelerator laboratory.

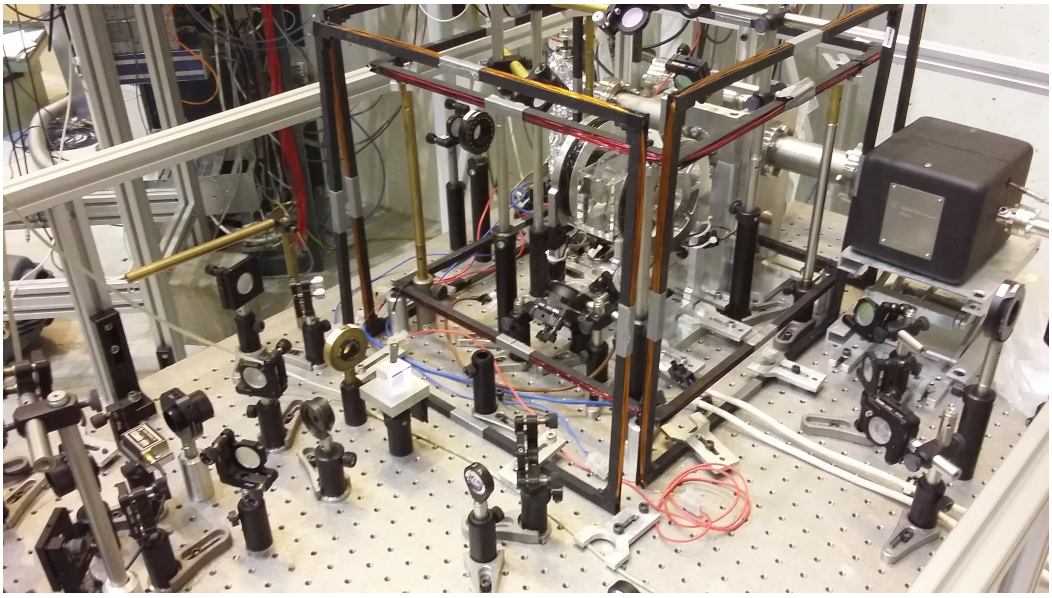

Figure D.8: Photo of optical setup and vacuum system for single ^{133}Cs MOT.

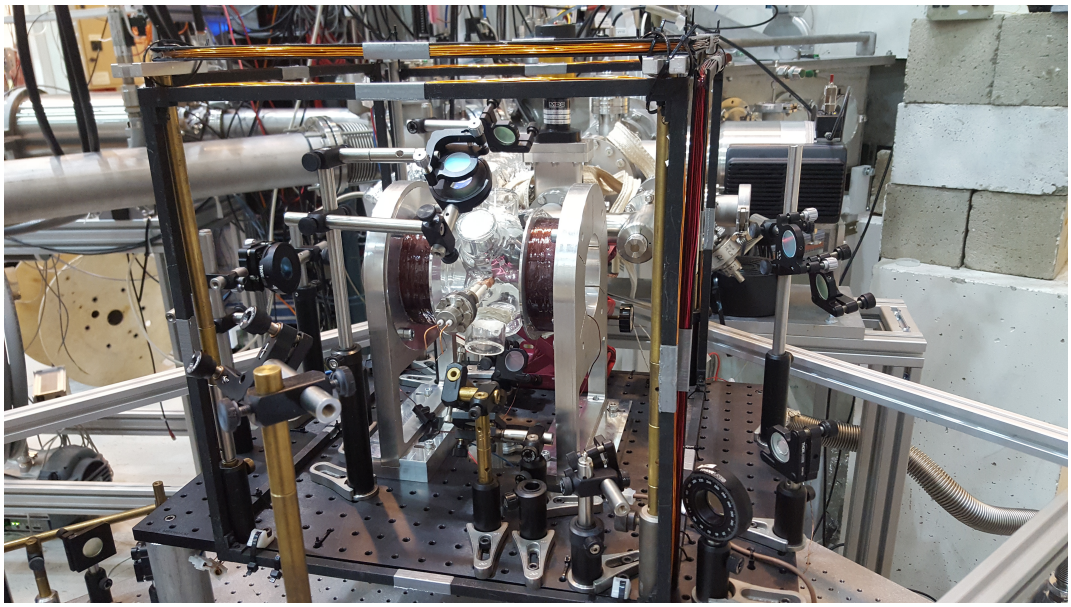

Figure D.9: Photo of optical setup and vacuum system for single ion implanted ^{133}Cs and ^{135}Cs MOT. The picture was taken by Dr Luca Marmugi and Dr Alexandros Giatzoglou.

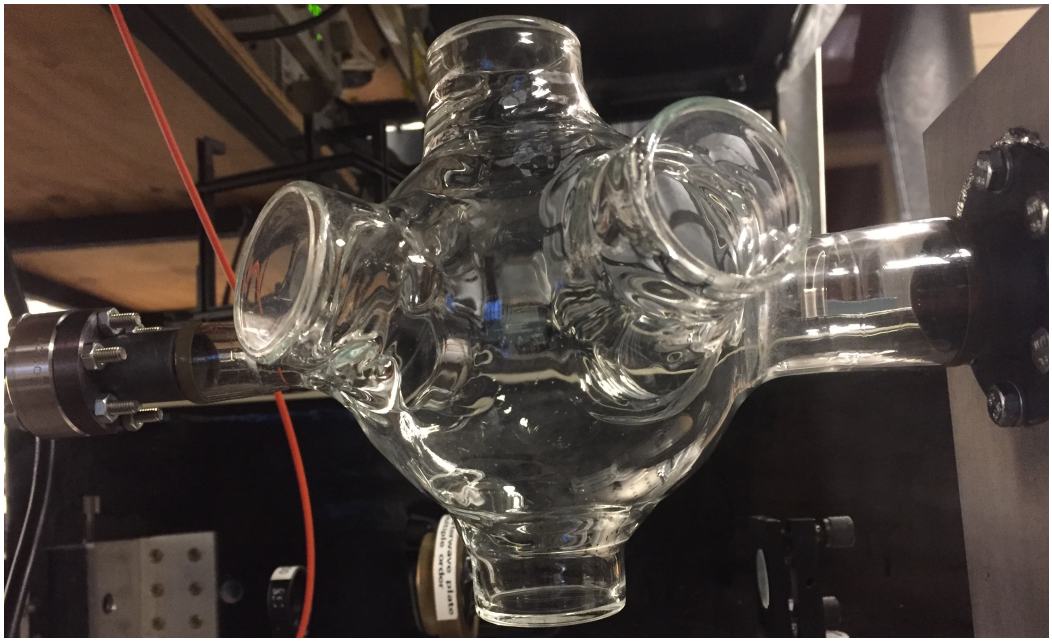

Figure D.10: Photo of the glass cell.

Figure D.11: Photo of the neutraliser. The picture was taken by Dr Luca Marmugi and Dr Alexandros Giatzoglou.

Bibliography

[1] H. S. Matis. *Nuclear Science, A Guide to the Nuclear Science Wall Chart (Third Edition)*. Lawrence Berkeley National Laboratory, 2003.

[2] Ph. Walker and G. Dracoulis. Energy traps in atomic nuclei. *Nature*, 399:35–40, 1999.

[3] Ph. Walker and J. Carroll. Up and downs of nuclear isomers. *Physics Today*, 58:39–44, 2005.

[4] F. Soddy. The complexity of the chemical elements. *Nuture*, 99:433–8, 1917.

[5] O. Hahn. Uber eine neue radioaktive substanz im uran. *Chem. Ber.*, 54:1131–42, 1921.

[6] P. J. Nolan and J. F. Sharpey-Schafer. The measurement of the lifetimes of excited nuclear states. *Rep. Prog. Phys.*, 42, 1979.

[7] G. Audi, O. Bersillon, J. Blachot, and A. H. Wapstra. The nubase evaluation of nuclear and decay properties. 2004.

[8] K. P. Xie, W. Y. Ke, W. Y. Liang, X. M. Fu, C. F. Jiao, J. C. Pei, and F .R. Xu. Collective rotations of fission isomers in actinide nuclei. *Sci China-Phys Mech Astron*, 57:189–193, 2014.

[9] S. Leoni et al. Multifaceted quadruplet of low-lying spin-zero states in ^{66}Ni: Emergence of shape isomerism in light nuclei. *Physical Review Letters*, 118(162502), 2017.

[10] W. H. King. *Isotope shifts in atomic spectra*. 1984.

[11] V. A. Dzuba, W. R. Johnson, and M. S. Safronova. Calculation of isotope shifts for cesium and francium. *Physical Review A*, 72:31–33, 2005.

[12] D. J. Griffiths. *Introduction to Quantum Mechanics*. 1994.

[13] K. Heilig and A. Steudel. Changes in mean-square nuclear charge radii from optical isotope shifts. *Atomic data and nuclear data tables*, 14(5):613–638, 1974.

[14] Ch. J. Foot. *Atomic Physics*. Oxford University Press, 2005.

[15] A. Pa´lffy. Nuclear effects in atomic transitions. *Contemporary Physics*, 51(6):471–496, 2010.

[16] M.L. Bissell, K.T. Flanagan, M.D. Gardner, M. Avgoulea, J. Billowes, P. Campbell, B. Cheal, T. Eronen, D.H. Forest, J. Huikari, A. Jokinen, I.D. Moore, A. Nieminenb, H. Penttilä, S. Rinta-Antila, B. Tordoff, G. Tungatea, and J. Äystöc. On the decrease in charge radii of multi-quasi particle isomers. *Physics Letters B*, 645(330–334), 2007.

[17] Yu. Gangrsky. Laser spectroscopy of high spin isomers – a review. *Hyperfine Interact*, (171):203–208, 2007.

[18] F. A. BABUSHKIN. Isotope shift of spectral line. *SOVIET PHYSICS JETP*, 17(5):1118–1122, 1963.

[19] C. Thibault, F. Touchard, S. Biittgenbach, R. Klapisch, and M. de Saint Simon. Hyperfiae structure and isotope shift of the d2, line of $^{76-98}$Rb and some of their isomers. *Physical Review C*, 23(6):2720–2729, 1981.

[20] R. Weiner. Charge distribution of excited isomeric nuclei and atomic spectra (the nuclear isomeric shift). *Physical Review*, 114(1):256–260, 1959.

[21] S. A. Blundell, P. E. G. Baird, C. W. P. Palmer, D. N. Stacey, and G. K. Woodgate. A re-evaluation of isotope shift constants. *Z. Phys. A - Atoms and Nuclei*, 321:31–33, 1985.

[22] B. Fricke and J. T. Waber. Calculation of isomer shift in mossbauer spectroscopy. *Physical Review B*, 5(9):3445–3449, 1972.

[23] C. Thibault, F. Touchard, S. Buttgenbach, R. Klapisch, M. D. S. Simon, H. T. Duong, P. Jacquinot, P. Juncar, S. Liberman, P. Pillet, J. Pinard, and J. L. Vialle. Hyperfine structure and isotope shift of the d2 line of $^{118-145}$Cs and some of their isomers. *Nuclear Physics A*, 367:1–12, 1981.

[24] D. A. Steck. Cesium D Line Data. 2010.

[25] M. D. di Rosa, S. G. Crane, J. J. Kitten, W. A. Taylor, D. J. Vieira, and X. Zhao. Magneto-optical trap and mass-separator system for the ultrasensitive detection of ^{135}Cs and ^{137}Cs. *Appl. Phys. B*, 76:45–55, 2003.

[26] G. Yang, H. Tazoe1, and M. Yamada. 135cs activity and ^{135}Cs/^{137}Cs atom ratio in environmental samples before and after the fukushima daiichi nuclear power plant accident. *Sci. Rep.*, 71(10), 2016.

[27] T.R.S.Wilson. Caesium-137 as movement tracer in the st george's channel. *J. Geophys. Res.*, 248:125–127, 1974.

[28] W. S. Broecker, E. R. Bonebakker, and G. G. Rocco. Radioisotopes and the rate of mixing across the main thermoclines of the ocean. *J. Geophys. Res.*, 71(24), 1966.

[29] J. Estrany, C. Garcia, and D. E. Walling. An investigation of soil erosion and redistribution in a mediterranean lowland agricultural catchment using caesium-137. *International Journal of Sediment Research*, 25(1):1–16, 2010.

[30] V L Ginzburg. What problems of physics and astrophysics seem now to be especially important and interesting (thirty years later, already on the verge of xxi century)? *Physics-Uspekhi*, 42(4):353–373, 1999.

[31] L. Marmugi, Ph. Walker, and F. Renzoni. Coherent gamma photon generation in a bose–einstein condensate of ^{135m}Cs. *Physics Letters B*, 777:281–285, 2018.

[32] S. Aubin, E. Gomez, L. A. Orozco, and G. D. Sprouse. High efficiency magneto-optical trap for unstable isotopes. *Rev. Sci. Instrum.*, 1:356, 2003.

[33] A. Giatzoglou, T. Poomaradee, I. Pohjalainen, S. Rinta-Antila, I. D. Moore, P. M. Walker, L. Marmugi, and F. Renzoni. A Facility for Production and Laser Cooling of Cesium Isotopes and Isomers. *Nucl. Instrum. Methods Phys. Res. A*, 908:367–375, 2018.

[34] T. Weber, J. Herbig, M. Mark, H. C. Nagerl, and R. Grimm. Bose-einstein condensation of cesium. *Science*, 229:232–235, 2003.

[35] J. Hu, A. Urvoy, Z. Vendeiro, V. Crépel, W. Chen, and V. Vuletić. Creation of a bose-condensed gas of ^{87}rb by laser cooling. *Science*, 358:1078–1080, 2017.

[36] M. Drewsen, Ph. Laurent, A. Nadir, G. Santarelli, A. Clairon, Y. Castin, and C. Salomon D. Grison 3. Investigation of sub-Doppler cooling effects in a cesium magneto-optical trap. *Appl. Phys. B*, 59:283–298, 1994.

[37] J. Dalibard and C. Cohen-Tannoudji. Laser cooling below the doppler limit by polarization gradients: simple theoretical models. *J. Opt. Soc. Am. B*, 6(11):2023–2045, 1989.

[38] D. S. Weiss, E. Riis, Y. Shevy, P. J. Ungar, and S. Chu. Optical molasses and multilevel atoms: experiment. *J. Opt. Soc. Am. B*, 6(11):2072–2083, 1989.

[39] H. J. Metcalf. *Laser Cooling and Trapping*. Springer-Verlag New York, 1999.

[40] D. S. Weiss, E. Riis, Y. Shevy, P. J. Ungar, and S. Chu. Revisiting the capture velocity of a cesium magneto-optical trap: model, simulation and experiment. *Laser Phys.*, 24(125502), 2014.

[41] T. Arpornthip and C. A. Sackett. Vacuum-pressure measurement using a magneto-optical trap. *Phys. Rev. A*, 85, 2012.

[42] L. Marcassa, V. Bagnato, Y. Wang, C. Tsao, and J. Weiner. Collisional loss rate in a magneto-optical trap for sodium atoms: Light-intensity dependence. *Phys. Rev. A*, 47(6):4563–4566, 1993.

[43] C. G. Townsend, N. H. Edwards, C. J. Cooper, K. P. Zetie, and C. J. Foot. Phase-space density in the magneto-optical trap. *Phys. Rev. A*, 52(2):1423–1440, 1995.

[44] S. Grego, M. Colla, A. Fioretti, J. H. Muller, P. Verkerk, and E. Arimondo. A cesium magneto-optical trap for cold collisions studies. *Optics Communication*, 132:519–526, 1996.

[45] W. Hong. Design and characterization of a littrow configuration external cavity diode laser.

[46] C. E. Wieman. Using diode lasers for atomic physics. *Rev. Sci. Instrum.*, 62(1), 1991.

[47] K. B. MacAdam, A . Steinbac, and C. Wieman. A narrow-band tunable diode laser system with grating feedback, and a saturated absorption spectrometer for cs and rb. *Am. J. Phys.*, 60(12):1098–1111, 1992.

[48] A. Wicht, M. Rudolf, P. Huke, R.-H. Rinkleff, and K. Danzmann. Grating enhanced external cavity diode laser. *Appl. Phys. B*, 78:137–144, 2004.

[49] R. S. Conroy, A. Carleton, A. Carruthers, B. D. Sinclair, C. F. Rae, and K. Dholakia. A visible extended cavity diode laser for the undergraduate laboratory. *Am. J. Phys.*, 68(10), 2000.

[50] P. Arora, A. Agarwal, and A. Sen Gupta. Simple alignment technique for polarisation maintaining fibres. *Rev. Sci. Instrum.*, 82(125103), 2011.

[51] N. W. Carlson. *Monolithic Diode-Laser Arrays*. Springer Series in Electronics and Photonics, 1994.

[52] L. Zhang, R. Dou, and J. Chen. Characteristics of the injection-locked master–slave lasers. *Applied Optics*, 47(14), 2008.

[53] W. Diao, J. He, Z. Liu, B. Yang, and J. Wang. Alternative laser system for cesium magnetooptical trap via optical injection locking to sideband of a 9-ghz current-modulated diode laser. *Optics Express*, 20(7), 2012.

[54] T. Rieger and T. Volz. Doppler-free saturation spectroscopy.

[55] P. Phoonthong. *State-Insensitive Traps for Caesium Atoms*. University College London, London, 2011.

[56] J. Wang, S. Yan, Y. Wang, T. Liu, and T. Zhang. Modulation-free frequency stabilization of a grating-external-cavity diode laser by magnetically induced sub-doppler dichroism in cesium vapor cell. *Jpn. J. Appl. Phys.*, 43(3), 2004.

[57] D. Q. Su, T. F. Meng, Z. H. Ji, J. P. Yuan, Y. T. Zhao, L. T. Xiao, and S. T. Jia. Application of sub-doppler DAVLL to laser frequency stabilization in atomic cesium. *Appled Optics*, 53(30), 2014.

[58] Z. T. Lu, K. L. Corwin, M. J. Renn, M. H. Anderson, E. A. Cornell, and C. E. Wieman. Low-velocity intense source of atoms from a magneto-optical trap. *Physical Review Letters*, 77(16):3331–3334, 1996.

[59] I. Serre, L. Pruvost, and H. T. Duong. Fluorescence imaging efficiency of cold atoms in free fall. *Applied Optics*, 37(6), 1998.

[60] J. F. Sherson, C. Weitenberg, M. Endres, I. Bloch M. Cheneau, and S. Kuhr. Single-atom-resolved fluorescence imaging of an atomic mott insulator. *Nature*, 467:68–72, 2010.

[61] C. Bradley. Design and realisation of an anti-helmholtz and feshbach coils system for ultra-cold atoms experiments with ^{133}Cs, 2015.

[62] F. Allard, I. Maksimovic, M. Abgrall, and Ph. Laurent. Automatic system to control the operation of an extended cavity diode laser. *Rev. Sci. Instrum.*, 75(1):54–58, 2004.

[63] D. J. Thompson and Robert E. Scholten. Narrow linewidth tunable external cavity diode laser using wide bandwidth filter. *Rev. Sci. Instrum.*, 83(023107), 2012.

[64] P. Zorabedian and Jr. W. R. Trutna. Interference-filter-tuned, alignment-stabilized, semiconductor external-cavity laser. *Optics Letters*, 13(10):826–828, 1988.

[65] X. Baillard, A. Gauguet, S. Bize, P. Lemonde, Ph. Laurent, A. Clairon, and P. Rosenbusch. Interference-filter-stabilized external-cavity diode lasers. *Optics Communications*, 266(1):609–613, 2006.

[66] T. A. Heumier and J. L. Carlsten. Mode hopping in semiconductor lasers.

[67] M. Fukuda, T. Mishima, N. Nakayama, and T. Masuda. Temperature and current coefficients of lasing wavelength in tunable diode laser spectroscopy. *Appl Phys B*, 100:377–382, 2010.

[68] K. Hueck, N. Luick, L. Sobirey, J. Siegl, T. Lompe, H. Moritz, L. W. Clark, and C. Chin. Calibrating high intensity absorption imaging of ultracold atoms. *Optics Express*, 25(8), 2017.

[69] G. Reinaudi, T. Lahaye, Z. Wang, and D. Guéry-Odelin. Strong saturation absorption imaging of dense clouds of ultracold atoms. *Optics Letters*, 32(21):3143–3145, 2007.

[70] P. Arora, S. B. Purnapatra, A. Acharya, R. Kumar, and A. Sen Gupta. Measurement of temperature of atomic cloud using time-of-flight technique. *MAPAN-Journal of Metrology Society of India*, 27(1):31–39, 2012.

[71] H. C. Zhang, P. F. Zhang, X. P. Xu, F. Cheng, and Y. Z. Wang. Optimized temperature measurement with time-of-flight method. *Optics Communications*, 282:3278–3281, 2009.

[72] S. Pradhan and B. N. Jagatap. Measurement of temperature of laser cooled atoms by one-dimensional expansion in a magneto-optical trap. *Rev. Sci. Instrum.*, 79, 2008.

[73] M. Vilén, L. Canete, B. Cheal, A. Giatzoglou, R. de Groote, A. de Roubin, T. Eronen, S. Geldhof, A. Jokinen, A. Kankainen, I. D. Moore, D. A. Nesterenko, H. Penttilä, I. Pohjalainen, M. Reponen, and S. Rinta-Antila. A new off-line ion source facility at igisol. *Nucl. Instrum. Methods Phys. Res. B*, 2019.

[74] A. Al-Adili, K. Jansson, M. Lantz, A. Solders, D. Gorelov, C. Gustavsson, A. Mattera, I. Moore, A. V. Prokofiev, V. Rakopoulos, H. Penttilä, D. Tarrío, S. Wiberg, M. Österlund, and S. Pomp. Simulations of the fission-product stopping efficiency in igisol. *Eur. Phys. J. A*, 51(5), 2015.

[75] P. Karvonen, I. Moore, T. Sonoda, T. Kessler, H. Penttilä, K. Peräjäarvi, P. Ronkanen, and J. Äystö. A sextupole ion beam guide to improve the efficiency and beam quality at igisols. *Nucl. Instrum. Methods Phys. Res. B*, 266(21):4794–4807, 2008.

[76] T. Dinneen, A. Ghiorso, and H. Gould. An orthotropic source of thermal atoms. *Rev. Sci. Instrum.*, 67(3):752–755, 1996.

[77] T. Warner, G. Ball, J. A. Behr, T. E. Chupp, G. Hackman P. Finlay, M. E. Hayden, B. Hyland, K. Koopmans, S. R. Nuss-Warren, M. R. Pearson, A. A. Phillips, M. A. Schumaker, M. B. Smith, C. E. Svensson, and E. R. Tardiff. Diffusion of xe in ta, zr, and pt. *Nucl. Instrum. Methods Phys. Res. A*, 538:135–142, 2005.

[78] J. F. Ziegler and J. P. Biersack. *The Stopping and Range of Ions in Matter. In: Bromley D.A. (eds) Treatise on Heavy-Ion Science*. Springer, 1985.

[79] M. Stephens, R. Rhodes, and C. Wieman. Study of wall coatings for vapor-cell laser traps. *J. Appl. Phys.*, 76(6):3479–3488, 1994.

[80] A. Lucchesini, S. Gozzini, C. Marinelli, and Luca Marmugi. Low energy atomic photodesorption from organic coatings. *Coating*, 6(47), 2016.

[81] M. Stephens and C. Wieman. High collection efficiency in a laser trap. *Physical Review Letters*, 7(24):3787–3790, 1994.

[82] S. Hu, X. Ren, M. Bachman, C. E. Sims, G. P. Li, and N. Allbritton. Surface modification of poly(dimethylsiloxane) microfluidic devices by ultraviolet polymer grafting. *Anal. Chem.*, 74:4117–4123, 2002.

[83] Y. J. Chuah, Y. T. Koh, K. Lim, N. V. Menon, Y. Wu, and Y. Kang. Simple surface engineering of polydimethylsiloxane with polydopamine for stabilized mesenchymal stem cell adhesion and multipotency. *Sci. Rep.*, 5(18162), 2015.

[84] W. Zhang, D. S. Choi, Y. H. Nguyen, J. Chang, and L. Qin. Studying cancer stem cell dynamics on pdms surfaces for microfluidics device design. *Sci. Rep.*, 3(2332), 2013.

[85] S. Agustsson, G. Bianchi, R. Calabrese, L. Corradi, A. Dainelli, A. Khanbekyan, C. Marinelli, E. Mariotti, L. Marmugi, L. Ricci, L. Stiaccini, L. Tomassetti, and A. Vanella. Enhanced atomic desorption of 209 and 210 francium from organic coating. *Scientific Reports*, 7(1):4207, 2017.

[86] P. Arora, S. Chowdhury, A. Agarwal, K. Pant, and A. S. Gupta. Characterization of cold atomic cloud in a magneto-optical trap. *Indian Journal of Pure and Applied Physics*, 49:590–595, 2011.

[87] E. Liatard, G. Gimond, G. Perrin, and F. Schussler. Release by therrnal diffusion of radioactive xe atoms implanted into w*. *Nucl. Instrum. Methods Phys. Res. A*, 385:398–402, 1997.

[88] C. de Mauro, R. Calabrese, L. Corradi, A. Dainelli, A. Khanbekyan, E. Mariotti, P. Minguzzi, L. Moi, S. Sanguinetti, G. Stancari, L. Tomassetti, and S. Veronesi. Measurement of diffusion coefficients of francium and rubidium in yttrium based on laser spectroscopy. *Phys. Rev. A*, 78(063415), 2008.

[89] H. Risken. *The Fokker-Planck Equation: Method s of Solution and Applications (second edition)*. Springer, 1989.

[90] D. Melconian, M. Trinczek, A. Gorelov, W. P. Alford, J. A. Behr, J. M. D'Auria, M. Dombsky, U. Giesen, K. P. Jackson, T. B. Swanson, and W. Wong. Release of ^{37}K from catcher foils. *Nucl. Instrum. Methods Phys. Res. A*, 538:93–99, 2005.

[91] C. de Mauro. *The Legnoro Francium MOT: efficient detection, characterization and perspectives*. University of Siena, Siena, 2007.

[92] M. Stephens and C. Wieman. High collection efficiency in a laser trap. *Physical Review Letters*, 72(24):3787–3790, 1994.

[93] V. S. Bagnato, L. G. Marcassa, S. G. Miranda, S. R. Muniz, and A. L. de Oliveira. Measuring the capture velocity of atoms in a magneto-optical trap as a function of laser intensity. *Phys. Rev. A*, 62:4563–4566, 2000.

[94] M. Haw, N. Evetts, W. Gunton, J. Van Dongen, J. L. Booth, and K. W. Madison. Magneto-optical trap loading rate dependence on trap depth and vapor density. *J. Opt. Soc. Am. B*, 29(3):475–483, 2012.

[95] H. Warhanek. A 53 min isomer of caesium 135. *Nuclear Physics*, 33:639–647, 1962.

[96] R. Guckert, X. Zhao, S. G. Crane, A. Hime, W. A. Taylor, D. Tupa, D. J. Vieira, and H. Wollnik. Magneto-optical trapping of radioactive 82rb atoms. *Phys. Rev. A*, 53(3):1637–1640, 1999.

[97] J. A. Behr and G. Gwinner. Standard model tests with trapped radioactive atoms. *J. Phys. G: Nucl. Part. Phys.*, 36(3), 2009.

[98] D. A. Tulchinsky, A. S. Hastings, and K. J. Williams. Characteristics and performance of offset phase locked single frequency heterodyned laser systems. *Rev. Sci. Instrum.*, 87(053107), 2016.

[99] K. Gibble, S. Chang, and R. Legere. Direct observation of *s*-wave atomic collisions. *Physical Review Letters*, 75(14), 1995.

[100] C. J. Myatt, N. R. Newbury, R. W. Ghrist, S. Loutzenhiser, and C. E. Wieman. Multiply loaded magneto-optical trap. *Optics Letters*, 21(4):290–292, 1996.

[101] P. Treutlein, K. Y. Chung, and S. Chu. High-brightness atom source for atomic fountains. *Phys. Rev. A*, 63(051401), 2001.

[102] V. Vuletic´, C. Chin, A. J. Kerman, and S. Chu. Degenerate raman sideband cooling of trapped cesium atoms at very high atomic densities. *Physical Review Letters*, 81(26):5768–5771, 1998.

[103] A. J. Kerman, V. Vuletic´, C. Chin, and S. Chu. Beyond optical molasses: 3d raman sideband cooling of atomic cesium to high phase-space density. *Physical Review Letters*, 84(3), 2000.

[104] S. E. Hamann, D. L. Haycock, G. Klose, P. H. Pax, I. H. Deutsch, and P. S. Jessen. Resolved-sideband raman cooling to the ground state of an optical lattice. *Physical Review Letters*, 80(19), 1998.

[105] Y. Li, J. Wu, G. Feng, J. Nute, S. Piano, L. Hackermüller, J. Ma, L. Xiao, and S. Jia. Enhanced raman sideband cooling of caesium atoms in a vapour-loaded magneto-optical trap. *Laser Phys. Lett.*, 12, 2015.

[106] Y. Yu, N. R. Hutzler, J. T. Zhang, L. R. Liu, J. D. Hood, T. Rosenband, and K.-K. Ni‡. Motional-ground-state cooling outside the lamb-dicke regime. *Physical Review A*, 97(063423), 2018.

[107] D. I. Kim, H. G. Rhee, J. B. Song, and Y. W. Lee. Laser output power stabilization for direct laser writing system by using an acousto-optic modulator. *Rev. Sci. Instrum.*, 78(103110), 2007.

[108] ”Acousto-Optic: application note – modulator model 3000 series”. Crystal Technology, inc.

[109] B. M. Garraway and V. G. Minogin. Theory of an optical dipole trap for cold atoms. *Physical Review A*, 62(043406), 2000.

[110] C. Y. Shih and M. S. Chapman. Nondestructive light-shift measurements of single atoms in optical dipole traps. *Physical Review A*, 87(063408), 2013.

[111] M. E. Shea and D. J. Gauthier. Comment on “nondestructive light-shift measurements of single atoms in optical dipole traps”. *Physical Review A*, 96(027401), 2017.